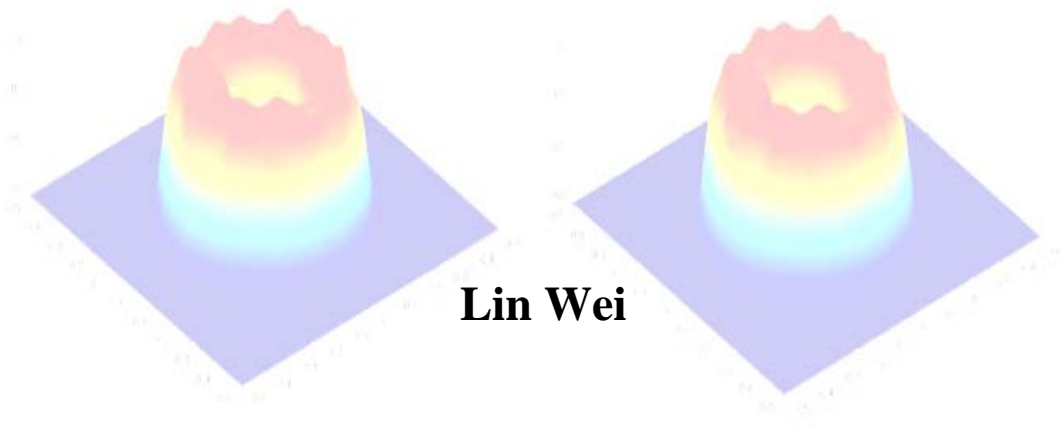


FAST ALGORITHMS AND APPLICATIONS FOR MULTI-DIMENSIONAL LEAST-SQUARES-BASED MINIMUM VARIANCE SPECTRAL ESTIMATION



Lin Wei

**Degree of Doctor of Philosophy (Ph.D.)
in Electrical and Computer Engineering presented on March 26, 2007**

Advisor: Dr. S. Lawrence Marple, Jr.

AN ABSTRACT OF THE THESIS OF

Lin Wei for the degree of Doctor of Philosophy in

Electrical and Computer Engineering presented on March 26, 2007.

Title:

FAST ALGORITHMS AND APPLICATIONS FOR MULTI-DIMENSIONAL
LEAST-SQUARES-BASED MINIMUM VARIANCE SPECTRAL ESTIMATION

Abstract approved: _____

S. Lawrence Marple Jr.

The main contributions of this thesis are the development and application of four computationally efficient solutions for least-squares-based (LS-based) minimum variance spectral estimation (MVSE). They are: (1) fast computational solution for the 1-D covariance LS-based MVSE, (2) fast computational solution for the 1-D modified covariance LS-based MVSE, (3) fast computational solution for the 2-D covariance LS-based MVSE, and (4) fast computational solution for the 2-D modified covariance LS-based MVSE. The four fast computational solutions not only significantly reduce computational complexity and save memory from array to vector sizing proportionalities, but they also inherit improved-feature details from the corresponding direct methods of 1-D and 2-D LS-based MVSEs. The two 2-D fast computational solutions numerically produce the same results as the corresponding 1-D fast solutions when the estimation order in one of the two dimensions is set to zero.

MVSEs are high-resolution spectral estimators which have been used extensively in the sensor community (for example, radar, sonar, communication

signal localization, and seismic velocity discrimination) for extracting and resolving more features from limited data collection apertures than traditional Fourier-based techniques. Least-squares-based MVSEs are especially applicable in the case that the autocorrelation is unknown and only 1-D or 2-D finite data acquisitions are available. However, LS-based minimum variance (MV) spectral estimators require intensive computational burdens which limit their operational use. This thesis proposes 1-D and 2-D fast computational solutions. The basis for the fast solutions is the exploitation of the special structures of the various inverse matrix relationships, which express the inverse of autocorrelation matrices (or autocorrelation-like quadratic-data-matrix product matrices in the case of the least-squares algorithms) in terms of the parametric autoregressive (AR) or linear prediction (LP) parameters. The fast algorithms also have the serendipitous feature that all lower-order solutions are obtained by the fast computational solutions without additional computations, unlike the non-fast approaches. This is useful especially when the correct order is unknown, requiring that a range of orders to be evaluated to determine the order that produces the best result using one algorithmic execution of a fast algorithm.

©Copyright by Lin Wei

March 26, 2007

All Rights Reserved

FAST ALGORITHMS AND APPLICATIONS FOR
MULTI-DIMENSIONAL LEAST-SQUARES-BASED
MINIMUM VARIANCE SPECTRAL ESTIMATION

by

Lin Wei

A THESIS

submitted to

Oregon State University

in partial fulfillment of
the requirements for the
degree of

Doctor of Philosophy

Presented March 26, 2007
Commencement June 2007

Doctor of Philosophy thesis of Lin Wei presented on March 26, 2007

APPROVED:

Major Professor, representing Electrical and Computer Engineering

Director of the School of Electrical Engineering and Computer Science

Dean of the Graduate School

I understand that my thesis will become part of the permanent collection of Oregon State University libraries. My signature below authorizes release of my thesis to any reader upon request.

Lin Wei, Author

ACKNOWLEDGMENTS

First of all I would like to express my sincere gratitude to my advisor Dr. S. Lawrence Marple Jr. for his continuous encouragement, support and guidance throughout my graduate studies. I am very thankful for his patience and always believing in me during the ups and downs of my Ph.D. research. His broad knowledge and logical way of thinking have been of great value for me. His technical advice and constructive comments have provided a good basis for this thesis. I would also like to thank Intel Corp. for providing me the opportunity to work with the great people that I met along the way.

I am deeply indebted to Dr. Hua-ping Liu, Dr. Mario Edgardo Magaña, Dr. Zhong-feng Wang and Dr. Guenter Schneider for their efforts and time to serve on my Ph.D. committee.

My thanks to all the members in my lab for their help and friendship. Special thanks to Dr. Ji-seok Liew and David Ohm for always being available for technical discussions.

Finally, I would like to express my deepest gratitude for the constant support, understanding and unconditional love that I received from my parents and my husband Hao.

TABLE OF CONTENTS

	<u>Page</u>
1 INTRODUCTION	1
1.1 Background and Motivation	1
1.2 Overview of Minimum Variance Spectral Estimation Research Contributions	6
1.3 Summary of Performance Behavior	14
2 ONE-DIMENSIONAL MINIMUM VARIANCE SPECTRAL ESTIMATORS: CONCEPTUAL AND ESTIMATION TECHNIQUES	20
2.1 Autocorrelation-Based Minimum Variance Spectral Estimation: Toeplitz Autocorrelation Case	20
2.2 Least-Squares-Based Minimum Variance Spectral Estimation: Covariance Case	21
2.3 Least-Squares-Based Minimum Variance Spectral Estimation: Modified Covariance Case	24
3 FAST SOLUTIONS FOR ONE-DIMENSIONAL MINIMUM VARIANCE SPECTRAL ESTIMATION	26
3.1 Autocorrelation-Based 1-D Minimum Variance Spectral Estimation: Toeplitz Autocorrelation Case	26
3.1.1 Review Fast Computational Solution	26
3.1.2 Computation and Storage Counts	28
3.2 Least-Squares-Based 1-D Minimum Variance Spectral Estimation: Covariance Case	28
3.2.1 Development of Fast Computational Solution	28
3.2.2 Computation and Storage Counts	35
3.3 Least-Squares-Based 1-D Minimum Variance Spectral Estimation: Modified Covariance Case	36
3.3.1 Development of Fast Computational Solution	36
3.3.2 Computation and Storage Counts	42

TABLE OF CONTENTS (Continued)

	<u>Page</u>
4 IMPROVED-FEATURE DETAIL USING FAST ALGORITHMS FOR ONE-DIMENSIONAL MINIMUM VARIANCE SPECTRAL ESTIMATION	44
4.1 Application One: Narrow-Band Sinusoidal Data	44
4.2 Application Two: Wide-Band Autoregressive Process	48
4.3 Application Three: Simulated Doppler Radar Data	49
4.4 Application Four: Actual 1-D Doppler Radar Data	51
5 TWO-DIMENSIONAL MINIMUM VARIANCE SPECTRAL ESTIMATORS: CONCEPTUAL AND ESTIMATION TECHNIQUES	67
5.1 Autocorrelation-Based 2-D Minimum Variance Spectral Estimation: Doubly-Toeplitz Autocorrelation Case	67
5.2 Least-Squares-Based 2-D Minimum Variance Spectral Estimation: Covariance Case	70
5.3 Least-Squares-Based 2-D Minimum Variance Spectral Estimation: Modified Covariance Case	75
6 FAST SOLUTIONS FOR TWO-DIMENSIONAL MINIMUM VARIANCE SPECTRAL ESTIMATION	79
6.1 Autocorrelation-Based 2-D Minimum Variance Spectral Estimation: Doubly-Toeplitz Autocorrelation Case	79
6.1.1 Review Fast Computational Solution	79
6.1.2 Computation and Storage Counts	82
6.2 Least-Squares-Based 2-D Minimum Variance Spectral Estimation: Covariance Case	83
6.2.1 Development of Fast Computational Solution	83
6.2.2 Computation and Storage Counts	93

TABLE OF CONTENTS (Continued)

	<u>Page</u>
6.3 Least-Squares-Based 2-D Minimum Variance Spectral Estimation: Modified Covariance Case	93
6.3.1 Development of Fast Computational Solution	93
6.3.2 Computation and Storage Counts	103
 7 IMPROVED-FEATURE DETAIL USING FAST ALGORITHMS FOR TWO-DIMENSIONAL MINIMUM VARIANCE SPECTRAL ESTIMA- TION.....	 105
7.1 Application One: Narrow-Band 2-D Sinusoid Data.....	105
7.2 Application Two: Wide-Band 2-D bandpass signal.....	107
7.3 Application Three: Actual 2-D Synthetic Aperture Radar Data ...	107
 8 SUMMARY OF RESEARCH CONTRIBUTIONS.....	 120
 BIBLIOGRAPHY	 125
 APPENDICES	 129
APPENDIX A LIST OF ACRONYMS	130
APPENDIX B LIST OF SYMBOLS	131

LIST OF FIGURES

<u>Figure</u>	<u>Page</u>
1.1 Overview of high-detail spectral estimation techniques.	2
1.2 Research contribution 1: flowchart of fast computational solution of 1-D LS-based MVSE in covariance case.	7
1.3 Research contribution 2: flowchart of fast computational solution of 1-D LS-based MVSE in modified covariance case.	8
1.4 Research contribution 3: flowchart of fast computational solution of 2-D LS-based MVSE in covariance case.	9
1.5 Research contribution 4: flowchart of fast computational solution of 2-D LS-based MVSE in modified covariance case.	10
1.6 Computation and storage savings of the fast algorithm vs the orig- inal method for 1-D covariance LS-Based MVSE. (a) Multiplication savings. (b) Addition savings. (c) Storage savings. Notation: p is the order of the estimator, N is the number of data values, and the number of 1-D FFT frequency bins $N_f = 64$ is used.	16
1.7 Computation and storage savings of the fast algorithm vs the original method for 1-D modified covariance LS-Based MVSE. (a) Multipli- cation savings. (b) Addition savings. (c) Storage savings. Notation: p is the order of the estimator, N is the number of data values, and the number of 1-D FFT frequency bins $N_f = 64$ is used.	17
1.8 Computation and storage savings of the fast algorithm vs the orig- inal method for 2-D covariance LS-Based MVSE. (a) Multipli- cation savings. (b) Addition savings. (c) Storage savings. Notation: $p_1 = p_2 = p$ are the orders of the 2-D estimator in rows and columns, $N_1 = N_2 = N$ are the size of 2-D data values, and the numbers of 2-D FFT frequency bins $N_{f1} = N_{f2} = 64$ are used.	18
1.9 Computation and storage savings of the fast algorithm vs the original method for 2-D modified covariance LS-Based MVSE. (a) Multipli- cation savings. (b) Addition savings. (c) Storage savings. Notation: $p_1 = p_2 = p$ are the orders of the 2-D estimator in rows and columns, $N_1 = N_2 = N$ are the size of 2-D data values, and the numbers of 2-D FFT frequency bins $N_{f1} = N_{f2} = 64$ are used.	19
4.1 True spectral density of the six complex sinusoidal signals.	45

LIST OF FIGURES (Continued)

<u>Figure</u>	<u>Page</u>
4.2 Comparing the capability for improved-feature detail for the different spectral estimators with $SNR = 40$ dB. (a) 1-D classical periodogram estimator. (b) 1-D AR Yule-Walker estimator. (c) 1-D lattice-Burg estimator. (d) the new fast 1-D covariance LS-based MV estimator. (e) the new fast 1-D modified covariance LS-based MV estimator. . . .	54
4.3 Comparing the capability for improved-feature detail for the different spectral estimators with $SNR = 20$ dB. (a) 1-D classical periodogram estimator. (b) 1-D AR Yule-Walker estimator. (c) 1-D lattice-Burg estimator. (d) the new fast 1-D covariance LS-based MV estimator. (e) the new fast 1-D modified covariance LS-based MV estimator. . . .	55
4.4 Close up of the peaks in different spectral estimators. (a) 1-D AR-Yule Walker estimator. (b) 1-D lattice-Burg estimator. (c) the new fast 1-D covariance LS-based MV estimator. (d) the new fast 1-D modified covariance LS-based MV estimator (zoomed in from Fig. 4.3).	56
4.5 Comparing the capability for improved-feature detail for the different spectral estimators with $SNR = 10$ dB. (a) 1-D classical periodogram estimator. (b) 1-D AR Yule-Walker estimator. (c) 1-D lattice-Burg estimator. (d) the new fast 1-D covariance LS-based MV estimator. (e) the new fast 1-D modified covariance LS-based MV estimator. . . .	57
4.6 Close up of the biased phenomenon in different estimators. (a) 1-D AR-Yule Walker estimator. (b) 1-D lattice-Burg estimator. (c) the new fast 1-D covariance LS-based MV estimator. (d) the new fast 1-D modified covariance LS-based MV estimator (zoomed in from Fig. 4.5).	58
4.7 Output variances, ρ_a and ρ_b , of forward and backward linear prediction error decrease as order p increases.	59
4.8 A six-order AR(6) process with driving noise variance $\rho_\omega = 0.01$ described by Eq. 4.4. (a) The positions of its poles. (b) True spectral density of the AR(6) process.	59
4.9 Response of four spectral estimators to the AR(6) process. Overlapped estimates of 50 realizations, each of 400-samples, are shown for each method. (a) 1-D AR Yule-Walker estimator. (b) 1-D lattice-Burg estimator. (c) the new fast 1-D covariance LS-based MV estimator. (d) the new fast 1-D modified covariance LS-based MV estimator.	60

LIST OF FIGURES (Continued)

<u>Figure</u>	<u>Page</u>
4.10 A set of 1-D spectral estimators of a 64-complex-point test sequence (order $p = 12$, sampling frequency $f_s = 2500$ Hz). (a) true spectra. (b) 1-D classical periodogram estimate. (c) 1-D AR Yule-Walker estimator. (d) 1-D lattice-Burg estimator. (e) the new fast 1-D covariance LS-based MV estimator. (f) the new fast 1-D modified covariance LS-based MV estimator.	61
4.11 Close up of the biased peak phenomenon in different estimators (order $p = 12$). (a) 1-D lattice-Burg estimator. (b) the new fast 1-D covariance LS-based MV estimator (zoomed in from Fig. 4.10).	62
4.12 Close up of the line splitting phenomenon in different estimators (order $p = 16$). (a) 1-D lattice-Burg estimator. (b) the new fast 1-D modified covariance LS-based MV estimator (zoomed in from Fig. 4.10).	62
4.13 Photos of the acquisition system of ISAR radar data for an actual truck. (a) 10-story microwave anechoic chamber. (b) truck was set on a pylon in the middle of the chamber. (c) close up the front of truck. (d) close up the rear of the truck. (The data were collected by Dr.Marple with permission for use in this thesis.)	63
4.14 Illustration of basic steps to create 1-D Doppler radar data and 2-D synthetic aperture radar data that can be used to create radar imagery by 2-D spectral analysis.....	64
4.15 Truck radar echoes spectral estimates by different 1-D spectral estimators (center azimuth is 47 degrees). (a) 1-D classical periodogram estimator. (b) 1-D covariance AR estimator. (c) the new fast 1-D covariance LS-based MV estimator. (d) the new fast 1-D modified covariance LS-based MV estimator.	65
4.16 Truck spectral estimator by different 1-D spectral estimates (center azimuth is 75 degrees). (a) 1-D classical periodogram estimator. (b) 1-D covariance AR estimator. (c) the new fast 1-D covariance LS-based MV estimator. (d) the new fast 1-D modified covariance LS-based MV estimator.	66

LIST OF FIGURES (Continued)

<u>Figure</u>	<u>Page</u>
7.1 Comparison of the resolution and accuracy for the different 2-D spectral estimators. (a) True spectra of 2-D complex sinusoids. (b) 2-D classical periodogram estimator. (c) 2-D covariance AR estimator. (d) 2-D lattice MV estimator. (e) the new fast 2-D covariance LS-based MV estimator. (f) the new fast 2-D modified covariance LS-based MV estimator.	109
7.2 One-dimensional slices for the different 2-D spectral estimators at 0.3 spatial fraction of sampling frequency in the column dimension. (a) True spectra of 2-D complex sinusoids. (b) 2-D classical periodogram estimator. (c) 2-D covariance AR estimator. (d) 2-D lattice MV estimator. (e) the new fast 2-D covariance LS-based MV estimator. (f) the new fast 2-D modified covariance LS-based MV estimator. . . .	110
7.3 Comparison data modeling capability for different 2-D spectral estimators. (a) doughnut-shape true 2-D spectrum of wide-band band-pass signal. (b) 2-D classical periodogram estimator. (c) 2-D covariance AR estimator. (d) 2-D lattice MV estimator. (e) the new fast 2-D covariance LS-based MV estimator. (f) the new fast 2-D modified covariance LS-based MV estimator.	111
7.4 S-band ISAR image of truck obtained by different spectral estimators (center azimuth 0 degrees - front of truck). (a) 2-D classical periodogram estimator. (b) 2-D covariance AR estimator.	112
7.5 S-band ISAR image of truck obtained by different spectral estimators (center azimuth 0 degrees - front of truck). (a) the new fast 2-D covariance LS-based MV estimator. (b) the new fast 2-D modified covariance LS-based MV estimator.	113
7.6 S-band ISAR image of truck obtained by different spectral estimators (center azimuth 47 degrees). (a) 2-D classical periodogram estimator. (b) 2-D covariance AR estimator.	114
7.7 S-band ISAR image of truck obtained by different spectral estimators (center azimuth 47 degrees). (a) the new fast 2-D covariance LS-based MV estimator. (b) the new fast 2-D modified covariance LS-based MV estimator.	115
7.8 S-band ISAR image of truck obtained by different spectral estimators (center azimuth 75 degrees). (a) 2-D classical periodogram estimator. (b) 2-D covariance AR estimator.	116

LIST OF FIGURES (Continued)

<u>Figure</u>	<u>Page</u>
7.9 S-band ISAR image of truck obtained by different spectral estimators (center azimuth 75 degrees). (a) the new fast 2-D covariance LS-based MV estimator. (b) the new fast 2-D modified covariance LS-based MV estimator.	117
7.10 S-band ISAR image of truck obtained by different spectral estimators (center azimuth 180 degrees - rear of truck). (a) 2-D classical periodogram estimator. (b) 2-D covariance AR estimator.	118
7.11 S-band ISAR image of truck obtained by different spectral estimators (center azimuth 180 degrees - rear of truck). (a) the new fast 2-D covariance LS-based MV estimator. (b) the new fast 2-D modified covariance LS-based MV estimator.	119

LIST OF TABLES

<u>Table</u>	<u>Page</u>
1.1 Comparison of Spectral Estimation Techniques. \times indicates not available, $\sqrt{}$ indicates available, N is the number of data samples, p is the order of model, N_f is the number of FFT frequency bins.	3
3.1 Comparison of the Computation Complexity and Storage Counts for 1-D ACS-Based MVSE. Note: p is the order of the estimator, N is the number of data sequence, N_f is the number of FFT frequency bins, \times is the number of complex multiplications, and $+$ is the number of complex additions.	28
3.2 Comparison of the Computation Complexity and Storage Counts for 1-D Covariance LS-Based MVSE. Note: p is the order of the estimator, N is the number of data sequence, N_f is the number of FFT frequency bins, \times is the number of complex multiplications, and $+$ is the number of complex additions. Note that the maximum order p_{max} must satisfy $p_{max} < (N - 1)/2$ for $\hat{\mathbf{R}}_p^{-1}$ exist.	35
3.3 Comparison of the Computation Complexity and Storage Counts for 1-D Modified Covariance LS-Based MVSE. Note: p is the order of the estimator, N is the number of data sequence, N_f is the number of FFT frequency bins, \times is the number of complex multiplications, and $+$ is the number of complex additions. Note that the maximum order p_{max} must satisfy $p_{max} < (2N - 1)/3$ for $\hat{\mathbf{R}}_p^{-1}$ exist.	43
6.1 Comparison of the Computation and Storage Counts for 2-D autocorrelation-based (ACS-Based) MVSE. Note: p_1, p_2 are the orders of the estimator in 2-D directions, N_1, N_2 are the size of 2-D data sequence, N_{f1}, N_{f2} are the numbers of 2-D FFT frequency bins, \times is the number of complex multiplications, and $+$ is the number of complex additions.	83
6.2 Comparison of the Computation and Storage Counts for 2-D Covariance LS-Based MVSE. Note: p_1, p_2 are the orders of the estimator in 2-D directions, N_1, N_2 are the size of 2-D data sequence, N_{f1}, N_{f2} are the numbers of 2-D FFT frequency bins, \times is the number of complex multiplications, and $+$ is the number of complex additions. Note that the maximum 2-D order p_{max} must satisfy $p_{max} < (N - 1)/2$ for $\hat{\mathbf{R}}_p^{-1}$ exist.	94

LIST OF TABLES (Continued)

<u>Table</u>	<u>Page</u>
6.3 Comparison of the Computation and Storage Counts for 2-D Modified Covariance LS-Based MVSE. Note: p_1, p_2 are the orders of the estimator in 2-D directions, N_1, N_2 are the size of 2-D data sequence, N_{f1}, N_{f2} are the numbers of 2-D FFT frequency bins, \times is the number of complex multiplications, and $+$ is the number of complex additions. Note that the maximum 2-D order p_{max} must satisfy $p_{max} < (2N - 1)/3$ for $\hat{\underline{\mathbf{R}}}_p^{-1}$ exist.	104
8.1 Comparison of Spectral Estimation Techniques. \times indicates not available, \checkmark indicates available, N is the number of data samples, p is the order of model, N_f is the number of FFT frequency bins. Notations are given in this chapter.	124

FAST ALGORITHMS AND APPLICATIONS FOR MULTI-DIMENSIONAL LEAST-SQUARES-BASED MINIMUM VARIANCE SPECTRAL ESTIMATION

1. INTRODUCTION

1.1. Background and Motivation

High-resolution spectral estimation has been widely used to provide improved spectral feature revelation in many practical applications, such as acoustics, communication, radar, biomedicine, economics, and many other fields. High-resolution spectral estimation can be applied to multi-dimensional data sources with an improved-feature detail capability. Fig. 1.1 overviews the application procedure of the high-resolution spectral estimation techniques covered in this thesis. One-dimensional (1-D) or two-dimensional (2-D) autoregressive/linear prediction (AR/LP) parameters can be calculated by existing fast algorithms, such as the Yule-Walker algorithm, the Burg lattice algorithm, the least-squares-based (LS-based) covariance method, and the LS-based modified covariance method. The last two methods have been selected in this thesis for their high-resolution capability [15, 16]. The spectral estimation techniques are then used to analyze 1-D or 2-D spectra. Table 1.1 summarizes the definitions, relative computational complexities and resolution capabilities of high-resolution spectral estimation techniques introduced by Marple, Kay and others [15, 16, 13, 30, 33, 34]. In Table 1.1, the minimum variance spectral estimation (MVSE) is indicated to have a high-resolution capability, compared with the Fourier-based spectral esti-

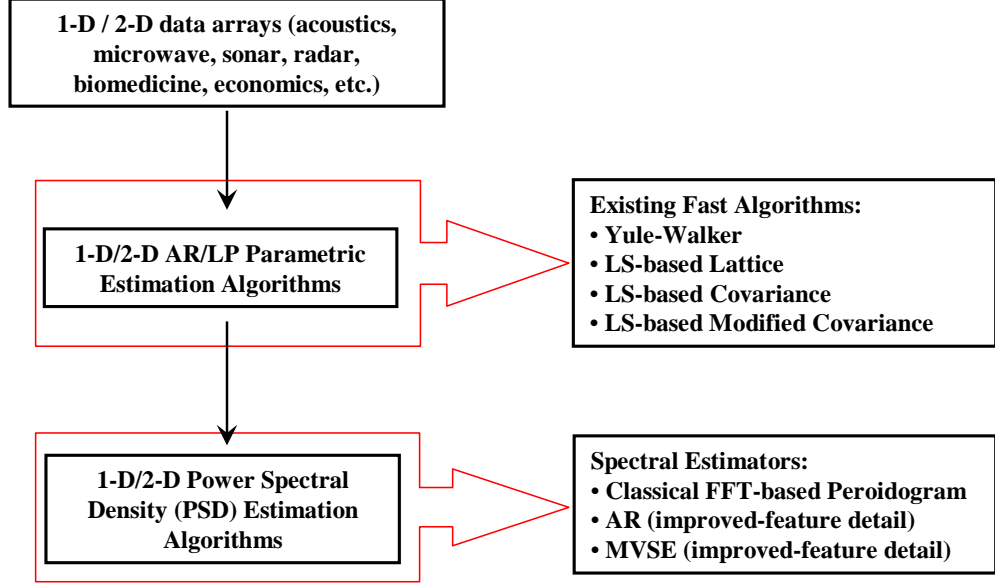


FIGURE 1.1. Overview of high-detail spectral estimation techniques.

mators, and almost as much resolution as the AR spectral estimators. However, the computational complexity of the original method of the MVSE is much higher than that of the Fourier-based spectral estimators and the AR spectral estimators. The fast computational solutions of the 1-D LS-based MVSE in the Yule-walker and Burg-Lattice cases can compensate for the computational inefficiency disadvantage of the original formulation of the MVSE while also increasing resolution. The new fast solutions of the LS-based MVSE, proposed in this thesis, preserve the high-resolution and decrease the computational complexity in the covariance and modified covariance cases. The resolutions of the new fast solutions are as high as the original non-fast-algorithm approach for estimating the MVSE. In addition, the new fast solutions, based on the AR covariance estimator and the AR modified covariance estimator, will recursively generate and save all intermediate order parameters. Therefore, if a lower order solution is required, it may be obtained without re-calculation, which is not possible in the original formulation

of the MVSE. This thesis focuses on investigation of the fast computational solutions for 1-D and 2-D LS-based MVSEs in the covariance and modified covariance cases.

Spectral Estimator Type	Defining Equations	Method	Resolution Capability	Lower-order Solutions Recursively Generated	Relative Computational Complexity	Relative Storage
Classical Fourier Methods	Eq. 4.2	Periodogram	Low	\times	$O(N \log_2 N)$	$O(N)$
Autoregressive	Eq.4.3	Yule-Walker	Medium	$\sqrt{}$	$O(p^2 + N_f \log_2 N_f)$	$O(p)$
		Burg Lattice	Medium	$\sqrt{}$		
		Covariance	high	$\sqrt{}$		
		Modified Covariance	high	$\sqrt{}$		
Minimum Variance Spectral Estimation	Eq.2.5	Original Approach	Medium	\times	$O(p^3)$	$O(p^2)$
	Eq.3.3	Yule-Walker + Correlation + FFT	Medium	$\sqrt{}$	$O(p^2 + N_f \log_2 N_f)$	$O(p)$
	Eq.3.3	Burg-Lattice + Correlation + FFT	high	$\sqrt{}$		
	Eq.3.17	Covariance + Correlation + FFT	high	$\sqrt{}$		
	Eq.3.31	Modified Covariance + Correlation + FFT	high	$\sqrt{}$		

TABLE 1.1. Comparison of Spectral Estimation Techniques. \times indicates not available, $\sqrt{}$ indicates available, N is the number of data samples, p is the order of model, N_f is the number of FFT frequency bins.

MVSE was originally introduced by Capon [1] in 1969 for use in multi-dimensional seismic array frequency-wavenumber analysis. Lacoss [2] reformulated Capon's MVSE for application to 1-D time-series analysis. Some recent

work has improved the characteristics and widened the range of applications of the MVSE [7–10, 15, 17, 19, 21, 26, 31]. For example, Krolik and Eizenman [17] facilitated the application of the MVSE to broadband source localization. Lee and Munson [26] reformulated spatially variant apodization (SVA) as a special variation of the MVSE to implement image reconstruction from partial Fourier data. Frazho and Sherman [19] discussed the convergence of the MVSE in a nonstationary noise environment. It has been difficult to create robust 2-D spectral estimators. Some 2-D spectral estimators that depend on polynomial factoring into isolated poles could not be directly extended from the high-resolution 1-D spectral estimators that depend on pole placement, because 2-D polynomials cannot always be factored into isolated poles. However, unlike other spectral estimation techniques, the MVSE was originally developed in a multi-dimensional setting as an array processing technique [1]. Non-least-squares 2-D MVSE methods [9, 10] have been successfully used in practice. In addition to the 2-D MVSE, the 2-D periodogram [9] and the 2-D hybrid methods [7] have been extended to 2-D primarily due to the fact that these 2-D estimators do not depend upon 2-D polynomial factorization [15].

The MVSE has been shown in the literature to achieve high resolution, however its practical application has been limited by an inherent disadvantage: computational inefficiency. The original computational burden of the MVSE was twofold. First, the calculation of an inverse autocorrelation matrix is intensive and a large amount of memory is required. Second, the power density estimator has to be calculated over all frequencies of interest. Typically, the second operation is even more computationally intensive. Fortunately, some simplifications have been discovered. In 1985, Musicus [13] published a fast computational solution for the 1-D autocorrelation-based (ACS-based) MVSE by exploiting the inverse

of the known autocorrelation matrix based on its Toeplitz structure. Inspired by Musicus' work, a fast computational solution for the 1-D covariance LS-based MVSE that exploits the *near-to-Toeplitz* data product matrix was summarized in 2005 by Wei and Marple [30]. The full details of the development is presented in this thesis. We then subsequently developed the fast computational solution for the 1-D modified covariance LS-based MVSE [34].

In 1986, Marple [14] developed a fast algorithm for the multichannel minimum variance spectral estimator, which involves a *block-Toeplitz* autocorrelation matrix, and in 1987 [15] introduced the first fast algorithms for the 2-D minimum variance spectral estimator. Andreas, Marple and Stoica [25] published a fast algorithm for the 2-D MVSE that utilized features from the development of the multichannel MVSE. This algorithm also used block recursion to solve the multichannel Yule-Walker normal equations, whose solution parameters could then be used to express the block matrix elements of the inverse block-Toeplitz matrix. Mathematical development of the fast algorithm of 2-D MVSE also very closely parallels the fast algorithm of 1-D MVSE. In 2006, based on previous work, Wei and Marple [34] developed a 2-D high-resolution algorithm for the covariance LS-MVSE and then developed the associated fast algorithm by extending the methods introduced in [15] and [30], respectively. This thesis will also present the development and application of a fourth fast solution, i.e., the fast computational solution for the 2-D modified covariance LS-based MVSE.

This thesis is organized as follows. In the first chapter, the background, motivation, and summary of performance behavior of the four fast computational solutions for the 1-D and 2-D LS-based MVSEs are reviewed. Then the concepts and estimation methods for three 1-D MVSE algorithms, i.e., the ACS-based MVSE, the covariance LS-based MVSE, and the modified covariance LS-based

MVSE, will be introduced in Chapter 2. In Chapter 3, the two fast computational solutions for the 1-D LS-based MVSE, inspired by the fast solution for 1-D ACS-based MVSE, will be presented. Their computation and storage counts will be provided as well. In Chapter 4, the application of the 1-D fast solutions to different data sets will be illustrated. Paralleling the development in Chapter 3, Chapter 5 will be dedicated to deriving the 2-D MVSE in the autocorrelation case, the LS-based covariance case, and the LS-based modified covariance case. Chapter 6 and Chapter 7 will present the 2-D fast algorithms development and 2-D test applications, respectively. Finally, the research contributions reported in this thesis will be summarized in Chapter 8.

1.2. Overview of Minimum Variance Spectral Estimation Research Contributions

This thesis proposes four new fast computational solutions for the 1-D and 2-D LS-based MVSE. The basis for the fast solutions is the exploitation of the structure of inverse autocorrelation matrices (or autocorrelation-like quadratic-data-matrix product matrices in the case of least-squares algorithms) in terms of their estimated AR or LP parameters. The contents in the red boxes in the figures from Fig. 1.2 through Fig. 1.5 highlight the key attributes of the development of the four fast solutions for the 1-D and 2-D LS-based MVSEs.

Inspired by the Musicus' fast solution [13] of 1-D ACS-based MVSE, in which he discovered that the MVSE denominator could be expressed efficiently as an FFT-computable function of the inverse Toeplitz autocorrelation matrix. It exploited the structure of the Toeplitz inverse, which can be formulated in terms of triangular Toeplitz matrix products with matrix elements composed of AR parameters. However, the autocorrelation matrix is unknown in practice and only

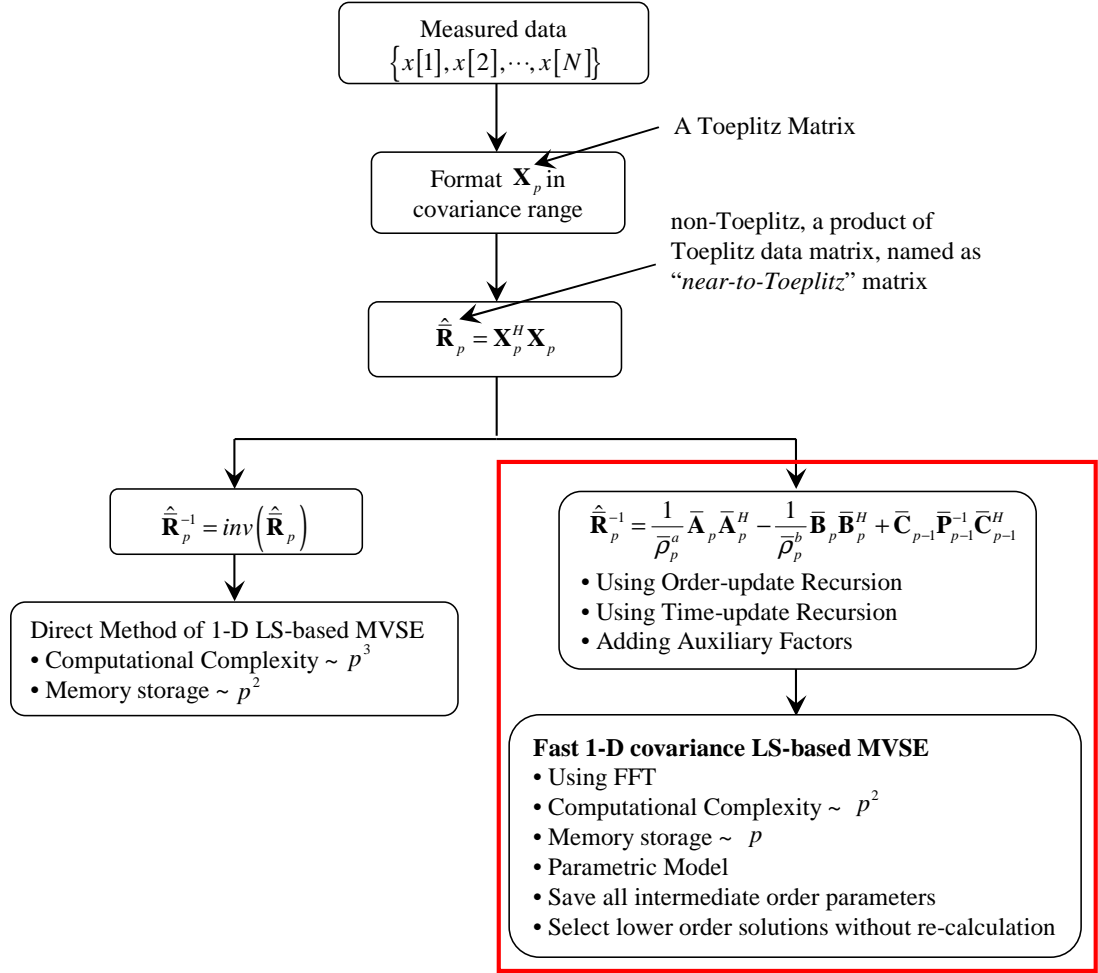


FIGURE 1.2. Research contribution 1: flowchart of fast computational solution of 1-D LS-based MVSE in covariance case.

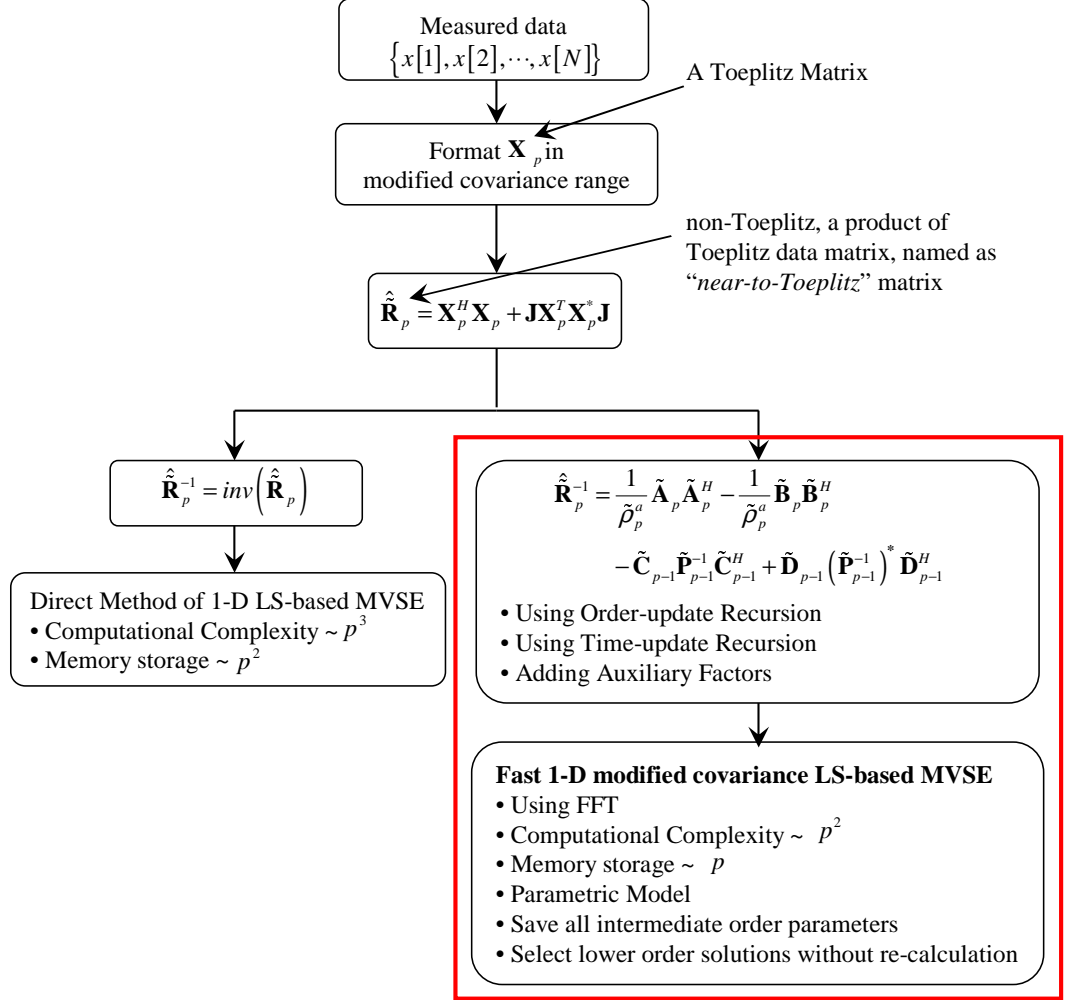


FIGURE 1.3. Research contribution 2: flowchart of fast computational solution of 1-D LS-based MVSE in modified covariance case.

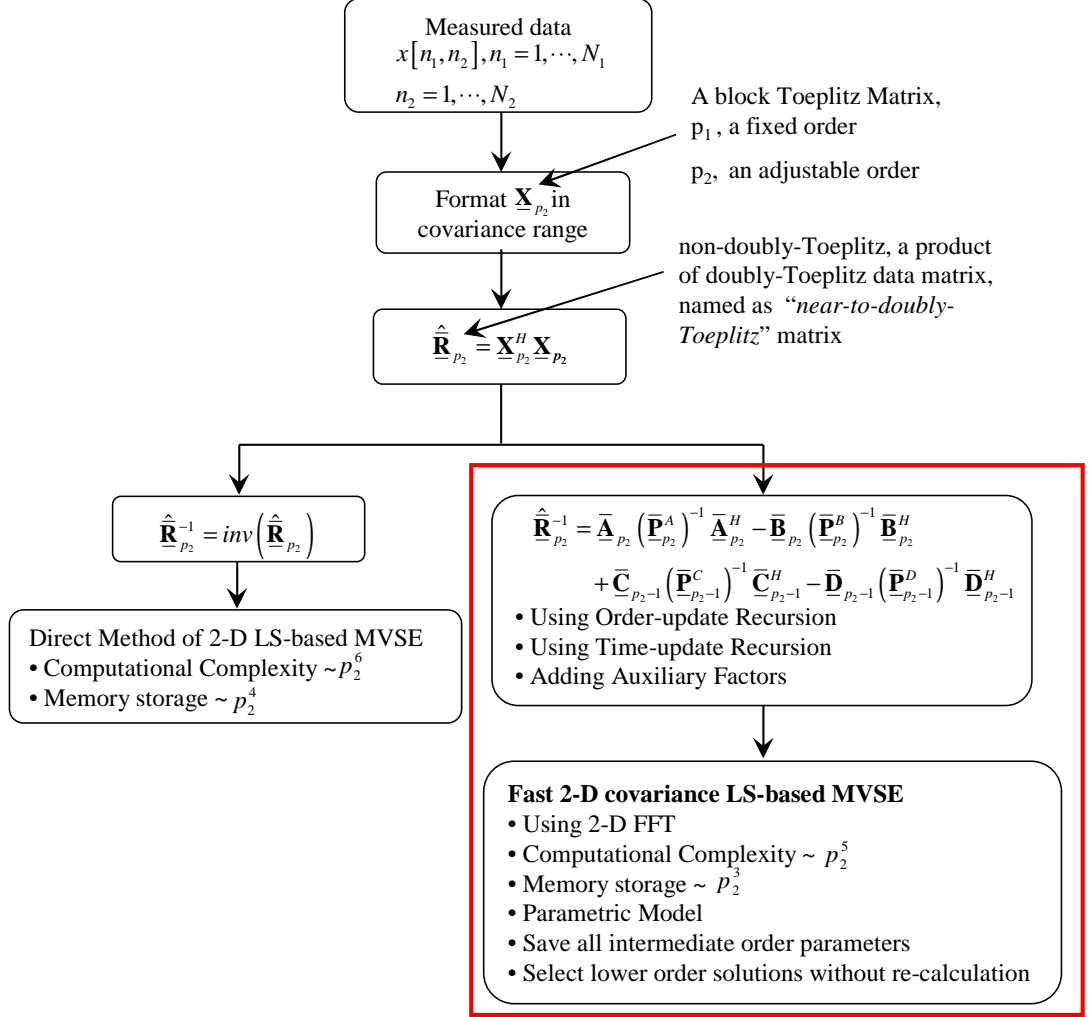


FIGURE 1.4. Research contribution 3: flowchart of fast computational solution of 2-D LS-based MVSE in covariance case.

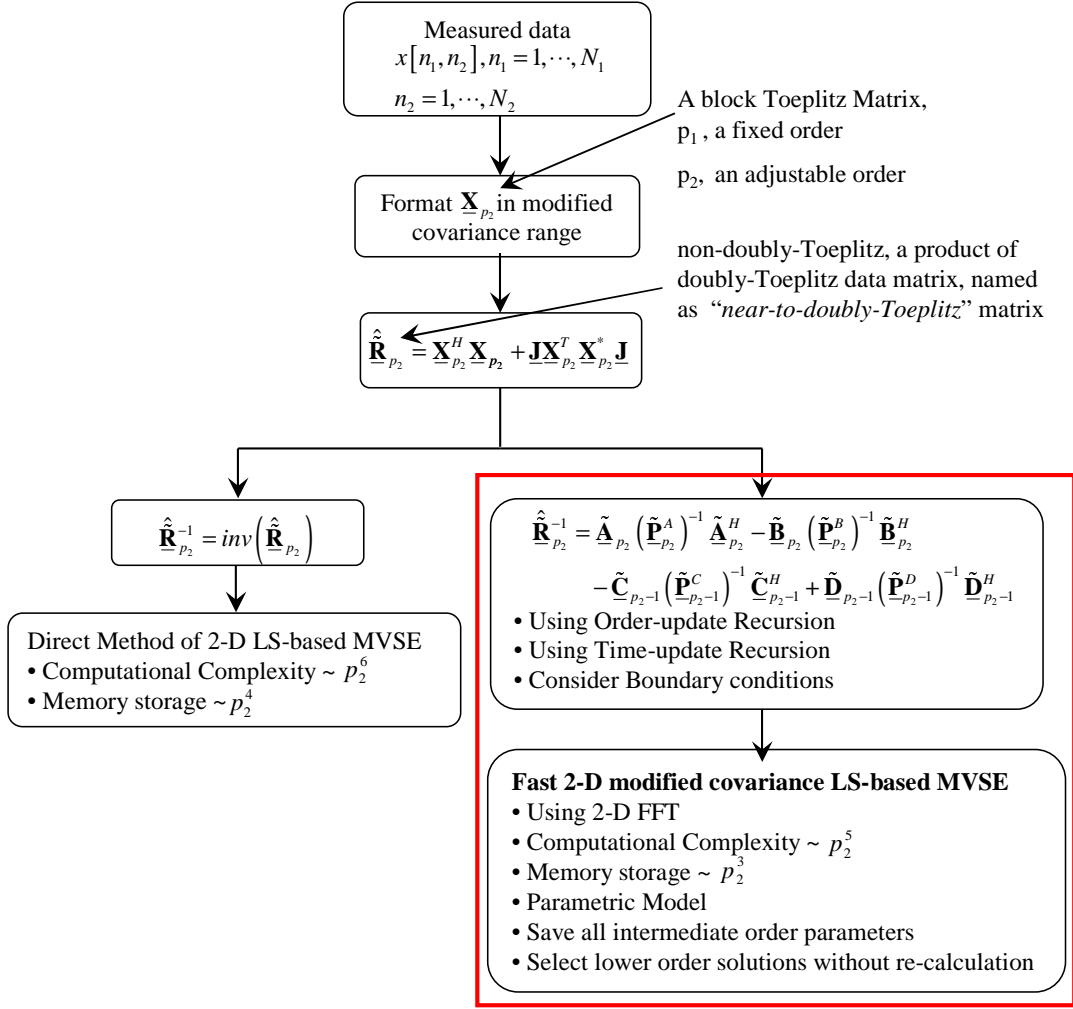


FIGURE 1.5. Research contribution 4: flowchart of fast computational solution of 2-D LS-based MVSE in modified covariance case.

data samples are available. Therefore, the MVSE has to be formulated in terms of a least squares minimization of the estimated output variance. Typically, two types of least squares estimators are of interest: (1) the covariance LP approach that utilizes separate forward and backward linear prediction for the estimate; (2) the modified covariance LP approach that employs combined forward and backward linear prediction. In the least-squares case, a stochastic approximation of the autocorrelation matrix is estimated by products of data matrices. As a result, the least-squares-based data matrix directly formed from a finite sampled data record has a *near-to-Toeplitz* structure in the 1-D case [30], and *near-to-doubly-Toeplitz* structure in the 2-D case [34], if the covariance data interval window is applied (calculated LP errors do not run off ends of data record). This leads to 1-D LS-based MVSE expressions that involve inverses of *near-to-Toeplitz* products of data matrices, and 2-D LS-based MVSE expressions involving inverses of *near-to-doubly-Toeplitz* products of data matrices. This thesis will show that, in the 1-D case, the inverse of *near-to-Toeplitz* data product matrix can be formulated in terms of triangular Toeplitz matrices products composed of LP parameters and associated gain parameters. The LP parameters and gain parameters can be provided by either the covariance LP algorithm or the modified covariance LP algorithm. These in turn can be substituted into the *near-to-Toeplitz* matrix inverse relationships to obtain fast computational solutions for evaluating the covariance LS-based MVSE and the modified covariance LS-based MVSE, respectively. Assuming p is the selected parametric order, the computational complexities of the two 1-D fast computational solutions are proportional to p^2 with memory storage proportional to p over the frequency range $[-1/2T, 1/2T]$ in Hz, versus p^3 computations and p^2 storage for each frequency component in both direct solution methods.

Table 3.2 and Table 3.3 in Chapter 3 summarize the computation and storage counts. Fig. 1.6 and Fig. 1.7 each provide three examples that compare the exact computational and storage savings of the two new 1-D fast solutions versus the non-fast original methods. Both the computation count and the storage count are functions of the length of the data record N , the model order p , and the number of the FFT frequency bins N_f . Fig. 1.6 and Fig. 1.7 show that the multiplication savings, addition savings and storage savings increase as the order p increases from $N = 64$, $N = 200$, to $N = 1000$. For all cases, when the order p is low, the computation and storage counts of the two new 1-D fast solutions may be very close to or even slightly larger than those of the direct methods, due to the overhead computation of the two new 1-D fast solutions. But as the order p increases, the computation and storage counts of the two new 1-D fast solutions are much less than those of the direct methods.

Similarly, for the 2-D case, the inverse matrix relationship of the *near-to-doubly-Toeplitz* data product matrix has a similar structure as discovered in the 1-D case, that is, it involves sums of products of triangular doubly-Toeplitz matrices. When the 2-D FFT is applied to compute the 2-D denominator of the 2-D LS-based MV estimators, a further significant simplification of the 2-D LS-based MVSE computation in the covariance and the modified covariance cases is possible. However, unlike the 2-D AR spectral estimators, the 2-D LS-based MV spectral estimators estimate the spectra without splitting it into four quadrant planes. In Chapter 5, it will be shown that the MV spectral estimator is numerically identical in each quarter-plane, and it does not have the skew problem of the other estimators, such as 2-D AR estimates. Combining quarter-plane estimates of the new fast solutions of LS-based MVSE is not necessary, which reduces computational complexity further. The computational complexities of the two

2-D fast computational solutions in the covariance and the modified covariance cases are proportional to p^5 , with memory storage proportional to p^3 over the 2-D frequency range $[-1/2T_1 \leq f_1 \leq 1/2T_1, -1/2T_2 \leq f_2 \leq 1/2T_2]$ in Hz or space per cycle (such as meters/cycle in this thesis), versus p^6 computation and p^4 storage, for each 2-D frequency component, if solved by the non-fast original 2-D method (we assume $p_1 = p_2 = p$, in which p_1 is the row parametric order and p_2 is the column parametric order).

Table 6.2 and Table 6.3 in Chapter 6 summarize the 2-D computation and storage counts in detail. Fig. 1.8 and Fig. 1.9 each provide three examples that compare the exact computational and storage savings of the two new 2-D fast solutions versus the original non-fast 2-D methods. Both the computation count and the storage count are functions of the size of data matrix ($N_1 \times N_2$), the row order p_1 and the column order p_2 of the model, and the number of 2-D FFT frequency bins ($N_{f1} \times N_{f2}$). For the sake of simplification, $p_1 = p_2 = p$, $N_1 = N_2 = N$, and $N_{f1} = N_{f2} = 64$ are assumed. Fig. 1.8 and Fig. 1.9 show that the multiplication savings, addition savings and storage savings increase as the number of data increases from $N_1 = N_2 = 64$, $N_1 = N_2 = 300$, to $N_1 = N_2 = 1000$. As observed in the 1-D cases of Fig. 1.6 and Fig. 1.7, selecting small orders p_1, p_2 will yield computation and storage counts of the two new 2-D fast solutions that may be very close to or even larger than those of the non-fast original 2-D methods, due to the overhead computation of the two new 2-D fast solutions. As the orders p_1 and p_2 increase, however, the computation and storage counts of the 2-D fast solutions are less than those of the direct methods. The results for very large data sizes $N_1 \times N_2$, such as 1000×1000 , and low 2-D orders $p_1 \times p_2$, such as 12×12 , indicate that the multiplication operations of the two new 2-D fast solution are larger than those of the original 2-D method. Since the multiplication operation

is very expensive, the new 2-D fast solutions may not be the best candidate in this situation. However we usually need a higher order to estimate all features in such a large data sample set.

Generally, the comparison results in Fig. 1.6 through Fig. 1.9 show that the four new fast computational solutions save significant computations and storage, especially multiplication operations which are more expensive, when the data size is not too large compared with the model order. As a benefit, the two new 2-D fast computational solutions produce numerically identical results as the corresponding 1-D fast solutions when the parametric order in one of the two dimension is set to zero. This provides a convenient tool to evaluate both 1-D and 2-D data case by using a single software implementation.

1.3. Summary of Performance Behavior

The four new fast computational solutions for the LS-based MVSE not only significantly reduce computational complexity and save memory by resizing from array to vector proportionalities, but also they inherit the improved-feature detail from the corresponding original methods of 1-D and 2-D LS-based MVSEs. The experimental results in Chapter 4 and Chapter 7 show that the LS-based MV spectral estimators exhibit the improved-feature details that may be missed by other spectral estimators, such as the Fourier-based algorithms or the AR methods. For example, the resolved peaks generated by the lattice-Burg methods show bias and line-splitting problems, which are not seen in the estimates produced by the four new fast solutions. The four new fast solutions create sharper peaks than other estimators compared in this thesis. Moreover, the new 1-D fast modified covariance estimates show the sharpest peaks compared with other estimates

in Fig. 4.4. This observation supports previous reports [15, 27] that concluded that the modified covariance method may provide the better performance since it combines the forward and backward LP parameters to provide a better statistical approximation of the autocorrelation sequence. Chapter 4.1 shows that, when the signal-to-noise (SNR) is 40 dB, the two new 1-D fast computational solutions generate 1.67 times higher resolution than the 1-D AR Yule-Walker method and the 1-D lattice-Burg method, which themselves have been reported as high-resolution estimators [15, 16]. The AR process test cases show that the estimates produced by the four new fast algorithms provide the best performance, and have less PSD magnitude variance and less frequency variance over an ensemble of repeated test cases. Another advantage of the four new fast computational algorithms is the recursive calculation that saves all intermediate order LP parameters, so that one can select a lower-order estimator without recalculating the LP parameters. It also helps if one is searching for the optimal order for data modeling, as illustrated later in Fig. 4.7. The least squares solutions do not seem to require as high an order as non-least-squares solutions in order to achieve similar feature resolution detail in the MVSE spectra. Application to inverse synthetic aperture radar (ISAR) radar data of an actual truck illuminated by the radar shows that the four new fast solutions can detect more scattering centers than the classical periodogram and AR spectral estimators in both the 1-D and 2-D cases. Also the scattering centers in the ISAR radar images created by the two new fast 2-D MVSE solutions are sharper than those generated by older radar-imaging spectral methods.

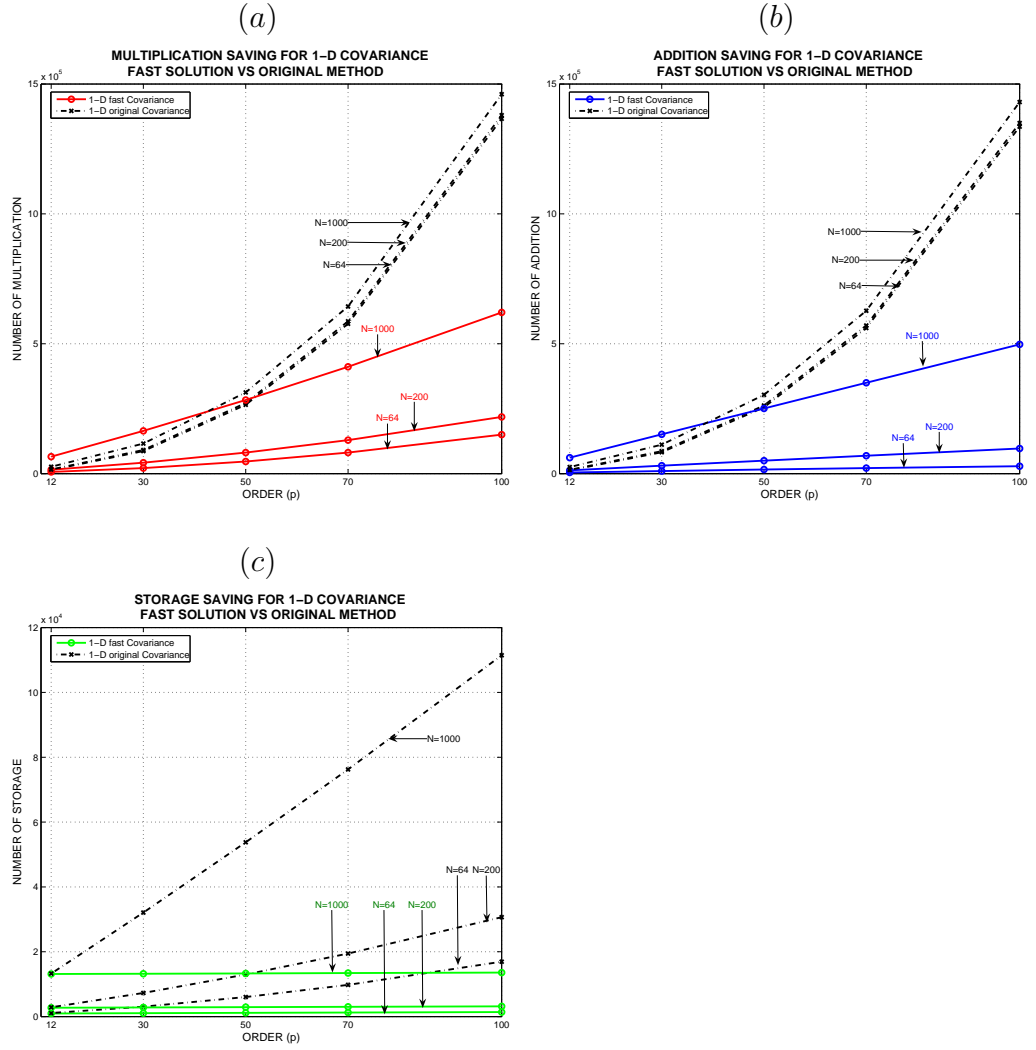


FIGURE 1.6. Computation and storage savings of the fast algorithm vs the original method for 1-D covariance LS-Based MVSE. (a) Multiplication savings. (b) Addition savings. (c) Storage savings. Notation: p is the order of the estimator, N is the number of data values, and the number of 1-D FFT frequency bins $N_f = 64$ is used.

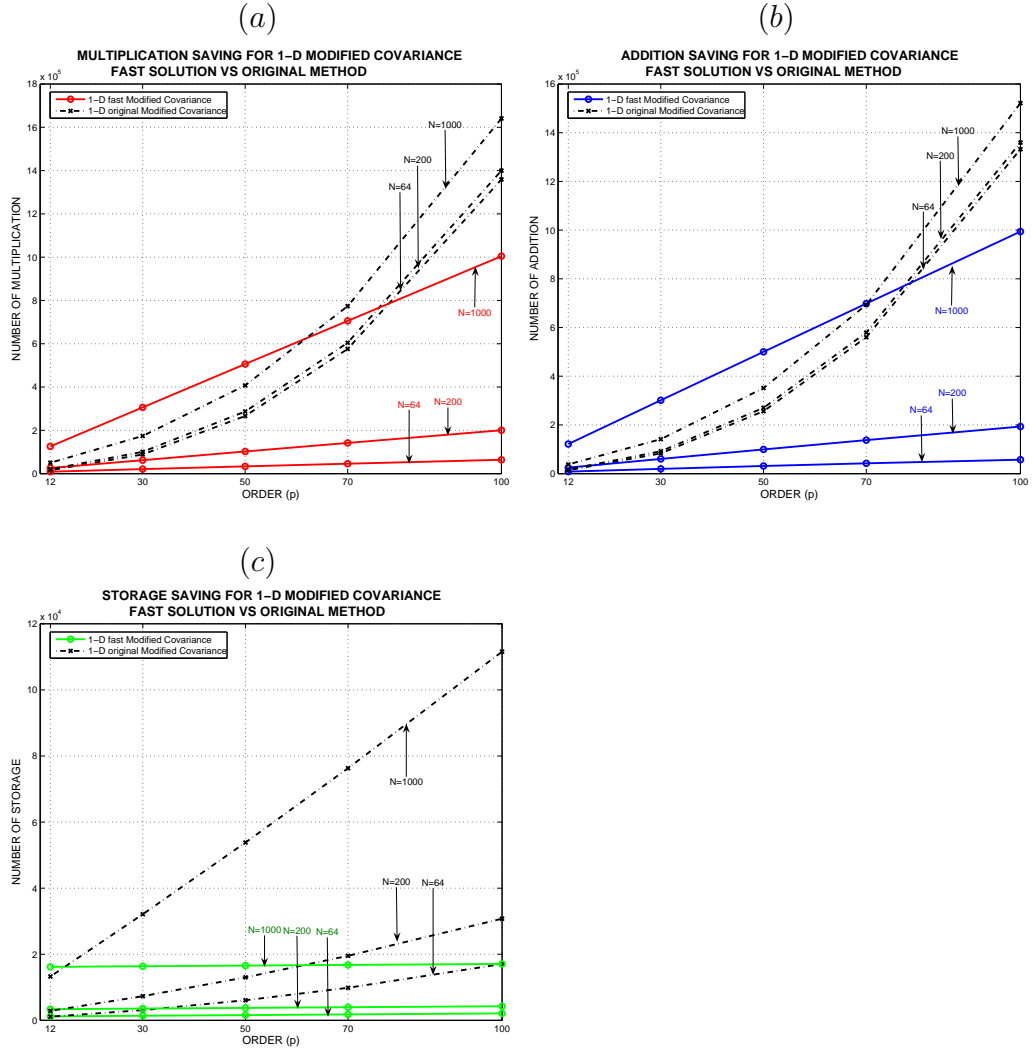


FIGURE 1.7. Computation and storage savings of the fast algorithm vs the original method for 1-D modified covariance LS-Based MVSE. (a) Multiplication savings. (b) Addition savings. (c) Storage savings. Notation: p is the order of the estimator, N is the number of data values, and the number of 1-D FFT frequency bins $N_f = 64$ is used.

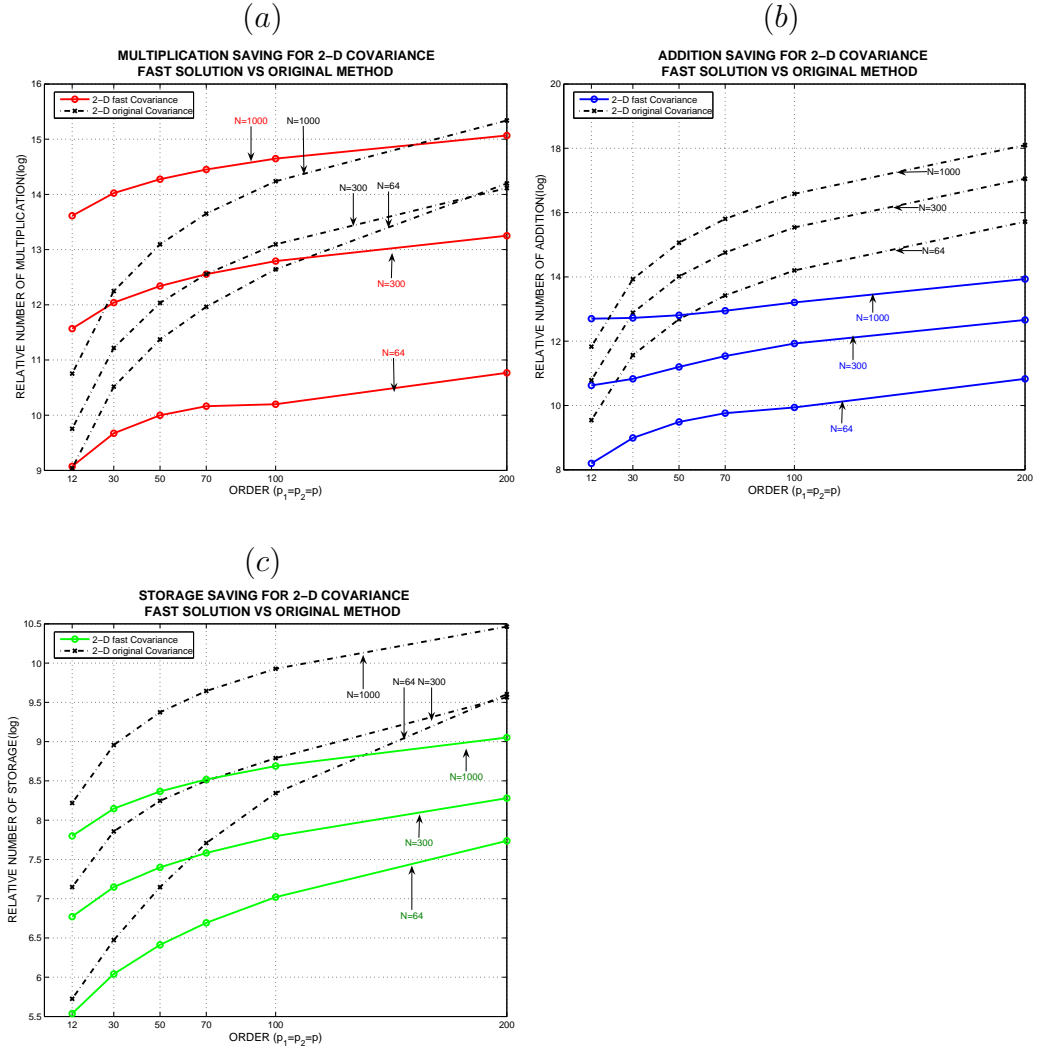


FIGURE 1.8. Computation and storage savings of the fast algorithm vs the original method for 2-D covariance LS-Based MVSE. (a) Multiplication savings. (b) Addition savings. (c) Storage savings. Notation: $p_1 = p_2 = p$ are the orders of the 2-D estimator in rows and columns, $N_1 = N_2 = N$ are the size of 2-D data values, and the numbers of 2-D FFT frequency bins $N_{f1} = N_{f2} = 64$ are used.

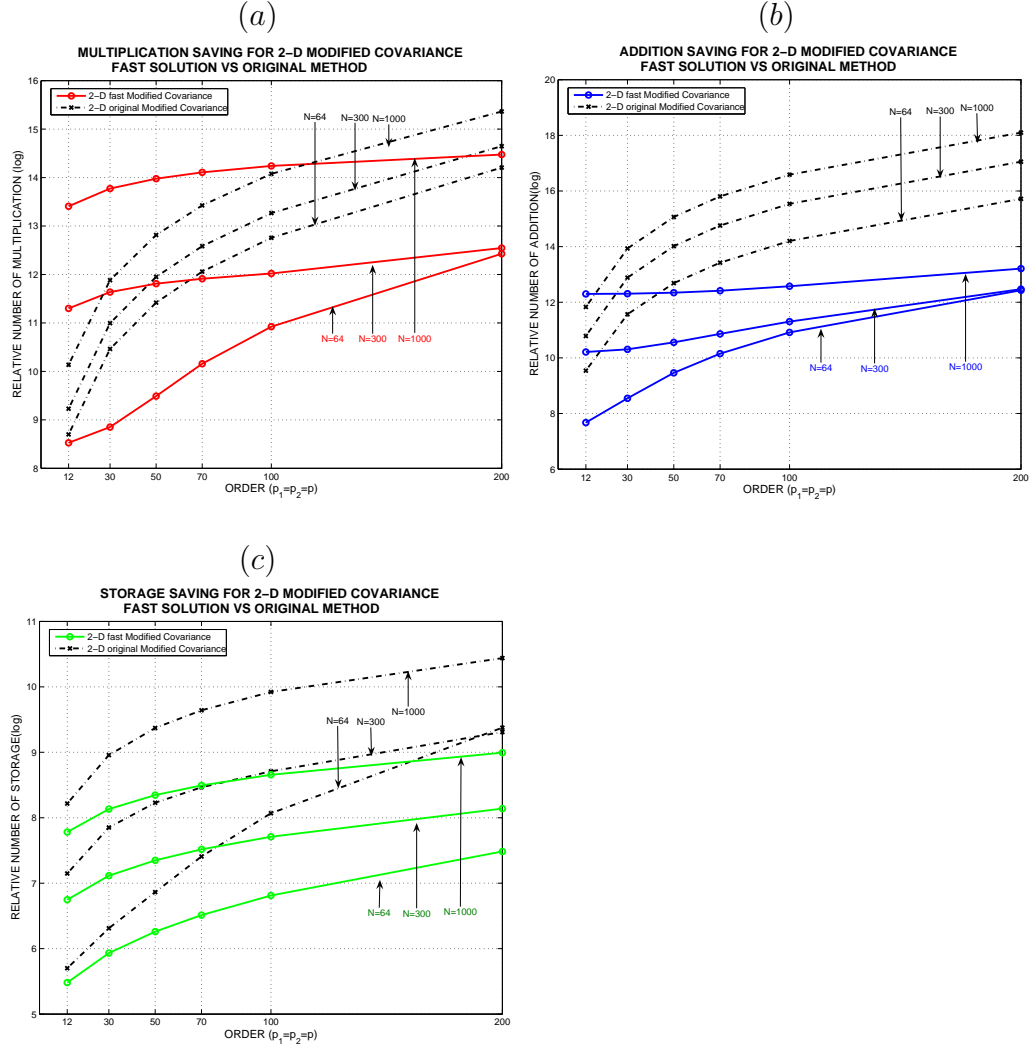


FIGURE 1.9. Computation and storage savings of the fast algorithm vs the original method for 2-D modified covariance LS-Based MVSE. (a) Multiplication savings. (b) Addition savings. (c) Storage savings. Notation: $p_1 = p_2 = p$ are the orders of the 2-D estimator in rows and columns, $N_1 = N_2 = N$ are the size of 2-D data values, and the numbers of 2-D FFT frequency bins $N_{f1} = N_{f2} = 64$ are used..

2. ONE-DIMENSIONAL MINIMUM VARIANCE SPECTRAL ESTIMATORS: CONCEPTUAL AND ESTIMATION TECHNIQUES

2.1. Autocorrelation-Based Minimum Variance Spectral Estimation: Toeplitz Autocorrelation Case

Assume that a stationary random process $x[n]$ for $1 \leq n \leq N$ is complex-valued (in general) and is filtered by passing through a finite impulse response (FIR) filter

$$y[n] = \sum_{k=0}^p h_p[k] x[n-k] = \mathbf{x}_p^T[n] \mathbf{h}_p \quad (2.1)$$

of order p and output $y[n]$, in which the data vector $\mathbf{x}_p^T[n] = (x[n] \ x[n-1] \ \cdots \ x[n-p])$ is a column vector of dimension $(p+1)$, and the filter vector $\mathbf{h}_p^T = (h_p[0] \ h_p[1] \ \cdots \ h_p[p])$ is also of dimension $(p+1)$ in which T represents the matrix transposition operation. The filter output variance is simply

$$\rho_p = \mathcal{E}\{|y[n]|^2\} = \mathbf{h}_p^H \mathcal{E}\{\mathbf{x}_p^*[n] \mathbf{x}_p^T[n]\} \mathbf{h}_p = \mathbf{h}_p^H \mathbf{R}_p \mathbf{h}_p \quad (2.2)$$

where H represents the matrix hermitian transposition operation and the $(p+1) \times (p+1)$ Toeplitz autocorrelation matrix is

$$\mathbf{R}_p = \begin{pmatrix} r[0] & r^*[1] & \cdots & r^*[p] \\ r[1] & \ddots & \ddots & \vdots \\ \vdots & \ddots & \ddots & r^*[1] \\ r[p] & \cdots & r[1] & r[0] \end{pmatrix} \quad (2.3)$$

and $r[m] = \mathcal{E}\{x[n]x^*[n-m]\}$ are the autocorrelation sequence (ACS) elements.

We minimize the filter output variance ρ_p subject to the constraint that, at a frequency f_0 , the gain is unity, that is, $\mathbf{e}_p^H(f_0)\mathbf{h}_p = 1$ for the $(p+1)$ -dimensional complex sinusoidal vector $\mathbf{e}_p^T(f_0) = (1 \ \exp(j2\pi f_0 T) \ \cdots \ \exp(j2\pi f_0 p T))$ and T

is the sample interval. The result of the constrained minimization of the variance [15] is

$$\rho_{\text{MV-acs}} = \frac{1}{\mathbf{e}_p^H(f_0) \mathbf{R}_p^{-1} \mathbf{e}_p(f_0)} \quad . \quad (2.4)$$

Since variance has units of power, scaling the variance by T changes the units to power per Hz, or power spectral density (PSD). Letting the frequency range over the Nyquist frequency interval $(-1/2T \leq f \leq 1/2T)$ in Hz, we define the traditional autocorrelation-based (ACS-based) MVSE [15] as

$$P_{\text{MV-acs}}(f) = T \rho_{\text{MV-acs}} = \frac{T}{\mathbf{e}_p^H(f) \mathbf{R}_p^{-1} \mathbf{e}_p(f)} \quad . \quad (2.5)$$

2.2. Least-Squares-Based Minimum Variance Spectral Estimation: Covariance Case

Assume that a finite data record of N complex-valued (in general) samples will be used to fit the frequency-adaptive FIR filter. The autocorrelation matrix is assumed unknown. The covariance LS-based MVSE is based on the concept of separate forward and backward FIR filters of the signal process $x[n]$ for $1 \leq n \leq N$

$$\begin{aligned} y^f[n] &= \sum_{k=0}^p \bar{a}_p[k] x[n-k] = \mathbf{x}_p^T[n] \bar{\mathbf{a}}_p = \bar{\mathbf{a}}_p^T \mathbf{x}_p[n], \\ y^b[n] &= \sum_{k=0}^p \bar{b}_p[k] x[n-p+k] = \mathbf{x}_p^T[n] \mathbf{J} \bar{\mathbf{b}}_p = \bar{\mathbf{b}}_p^T \mathbf{J} \mathbf{x}_p[n] \end{aligned} \quad (2.6)$$

of order p . The forward filter output $y^f[n]$ and the backward filter output $y^b[n]$ depend on the column $(p+1)$ -dimensional data vector \mathbf{x}_p , which is defined in Eq. 2.1. In practice, we most choose $p < N$. The filter forward parameter vector $\bar{\mathbf{a}}_p$ and the backward parameter vector $\bar{\mathbf{b}}_p$ are defined as

$$\begin{aligned} \bar{\mathbf{a}}_p^T &= (1 \ \bar{a}_p[1] \ \bar{a}_p[2] \ \cdots \ \bar{a}_p[p]) \\ \bar{\mathbf{b}}_p^T &= (1 \ \bar{b}_p[1] \ \bar{b}_p[2] \ \cdots \ \bar{b}_p[p]), \end{aligned}$$

respectively. A symbol with a bar above it, such as \bar{a} , means that it is related to the covariance case. A symbol written in bold font represents a matrix or a vector, rather than a scalar. Note that $\bar{a}_p[0] = \bar{b}_p[0] = 1$ by definition. We also note that $\bar{a}_p[p] = k_p^a$ and $\bar{b}_p[p] = k_p^b$, where k_p^a and k_p^b are reflection coefficients in a lattice realization of the LP error filters [15]. \mathbf{J} is a reflection matrix (an all-zeros matrix with ones along the anti-diagonal, whose dimension depends on the equation matrix structure) that has the effect of time reversing a signal vector. Note that $\mathbf{J}\mathbf{J} = \mathbf{I}$, the identity matrix.

The definition of the covariance LS-based MVSE assumes that $x[n]$ is only available over the range $1 \leq n \leq N$, so that FIR outputs can only be formed over the interval $p+1 \leq n \leq N$ to avoid running off the ends of the data. The sum of squared error magnitudes of the forward filter, if normalized by $1/(N-p)$, becomes an estimate of the output variance

$$\begin{aligned}
 \hat{\rho}_p &= \frac{1}{N-p} \sum_{n=p+1}^N |y^f[n]|^2 \\
 &= \frac{1}{N-p} \bar{\mathbf{a}}_p^H \left(\sum_{n=p+1}^N \mathbf{x}_p^*[n] \mathbf{x}_p^T[n] \right) \bar{\mathbf{a}}_p \\
 &= \frac{1}{N-p} \bar{\mathbf{a}}_p^H (\mathbf{X}_p^H \mathbf{X}_p) \bar{\mathbf{a}}_p \\
 &= \frac{1}{N-p} \bar{\mathbf{a}}_p^H \hat{\mathbf{R}}_p \bar{\mathbf{a}}_p
 \end{aligned} \tag{2.7}$$

in which the $(N-p) \times (p+1)$ rectangular Toeplitz data matrix is

$$\mathbf{X}_p = \begin{pmatrix} x[p+1] & \cdots & x[1] \\ \vdots & \ddots & \vdots \\ x[N-p] & \cdots & x[p+1] \\ \vdots & \ddots & \vdots \\ x[N] & \cdots & x[N-p] \end{pmatrix}, \tag{2.8}$$

and the $(p+1) \times (p+1)$ dimensional data product matrix

$$\begin{aligned}\hat{\mathbf{R}}_p &= \mathbf{X}_p^H \mathbf{X}_p \\ &= \begin{pmatrix} \hat{r}_p[0,0] & \cdots & \hat{r}_p[0,p] \\ \vdots & \ddots & \vdots \\ \hat{r}_p[p,0] & \cdots & \hat{r}_p[p,p] \end{pmatrix}\end{aligned}\quad (2.9)$$

is a stochastic least squares approximation of an ACS matrix, in which the elements of $\hat{\mathbf{R}}_p$ are $\hat{r}_p[i, j] = \sum_{m=p+1}^N x^*[m-i]x[m-j]$ for $0 \leq i, j \leq p$.

We minimize the estimated filter output variance $\hat{\rho}_p$ subject to the same unit gain constraint as applied to the ACS-based MVSE such that, at a frequency f_0 , $\mathbf{e}_p^H(f_0) \bar{\mathbf{a}}_p = 1$. Let $\bar{\mathbf{a}}_p = \bar{\mathbf{a}}_{p,min} + \boldsymbol{\delta}_p$ in which $\boldsymbol{\delta}_p$ is defined as a $(p+1) \times 1$ complex vector (in general) that satisfies $\mathbf{e}_p^H(f_0) \boldsymbol{\delta}_p = 0$. Substituting $\bar{\mathbf{a}}_p$ into the right side of Eq. 2.7 yields

$$\bar{\mathbf{a}}_p^H \hat{\mathbf{R}}_p \bar{\mathbf{a}}_p = \bar{\mathbf{a}}_{p,min}^H \hat{\mathbf{R}}_p \bar{\mathbf{a}}_{p,min} + \bar{\mathbf{a}}_{p,min}^H \hat{\mathbf{R}}_p \boldsymbol{\delta}_p + \boldsymbol{\delta}_p^H \hat{\mathbf{R}}_p \bar{\mathbf{a}}_{p,min} + \boldsymbol{\delta}_p^H \hat{\mathbf{R}}_p \boldsymbol{\delta}_p$$

in which the two middle terms are equal to zero

$$\bar{\mathbf{a}}_{p,min}^H \hat{\mathbf{R}}_p \boldsymbol{\delta}_p = \left(\mathbf{e}_p^H(f_0) \hat{\mathbf{R}}_p^{-1} \mathbf{e}_p(f_0) \right)^{-1} \mathbf{e}_p^H(f_0) \boldsymbol{\delta}_p = 0,$$

$\bar{\mathbf{a}}_p = (\mathbf{e}_p^H(f_0))^{-1}$, and $\boldsymbol{\delta}_p^H \hat{\mathbf{R}}_p \bar{\mathbf{a}}_{p,min} = (\bar{\mathbf{a}}_{p,min}^H \hat{\mathbf{R}}_p \boldsymbol{\delta}_p)^H = 0$, where $\hat{\mathbf{R}}_p$ is hermitian and positive definite. Hence,

$$\bar{\mathbf{a}}_p^H \hat{\mathbf{R}}_p \bar{\mathbf{a}}_p - \bar{\mathbf{a}}_{p,min}^H \hat{\mathbf{R}}_p \bar{\mathbf{a}}_{p,min} = \boldsymbol{\delta}_p^H \hat{\mathbf{R}}_p \boldsymbol{\delta}_p \geq 0 \quad . \quad (2.10)$$

Thus, the minimum value of $\bar{\mathbf{a}}_p^H \hat{\mathbf{R}}_p \bar{\mathbf{a}}_p$ follows from Eq. 2.10 by selecting the minimizing $\bar{\mathbf{a}}_p$ vector as

$$\bar{\mathbf{a}}_{p,min} = \frac{\hat{\mathbf{R}}_p^{-1} \mathbf{e}_p(f_0)}{\mathbf{e}_p^H(f_0) \hat{\mathbf{R}}_p^{-1} \mathbf{e}_p(f_0)} \quad .$$

Substituting the above expression $\bar{\mathbf{a}}_{p,min}$ into Eq. 2.7 yields the constrained least-squares covariance minimization of the estimated variance

$$\hat{\rho}_{\text{MV-cov}} = \frac{1}{\mathbf{e}_p^H(f_0) \hat{\mathbf{R}}_p^{-1} \mathbf{e}_p(f_0)} \quad .$$

Scaling the variance by T then yields units of PSD. Letting the frequency range over $-1/2T \leq f \leq 1/2T$ in Hz, we define the covariance LS-based MVSE as

$$\hat{P}_{\text{MV-cov}}(f) = T \hat{\rho}_{\text{MV-cov}} = \frac{T}{\mathbf{e}_p^H(f) \hat{\mathbf{R}}_p^{-1} \mathbf{e}_p(f)} \quad . \quad (2.11)$$

Note that the LS-based data product matrix $\hat{\mathbf{R}}_p$ does not have a Toeplitz structure, but it does have a *near-to-Toeplitz* (it is the product of two rectangular Toeplitz data matrices) property which can be exploited to decompose the inverse matrix $\hat{\mathbf{R}}_p^{-1}$ into sums of products of triangular Toeplitz matrices. We will provide the derivation in Section 3.2.1. $\hat{\mathbf{R}}_p$ is also a hermitian matrix since

$$\hat{\mathbf{R}}_p = \hat{\mathbf{R}}_p^H \quad .$$

2.3. Least-Squares-Based Minimum Variance Spectral Estimation: Modified Covariance Case

The modified covariance LS-based MVSE differs from the covariance LS-based MVSE in that a combination of filtering the signal process $x[n]$, $1 \leq n \leq N$, in forward and backward directions through the FIR filter is presented in one variance expression. It was shown in [15] that the forward and backward LP parameters for a stationary random process are simply complex conjugates of the other, so the output $y^b[n]$ of the backward FIR filter in Eq. 2.6 may then be expressed as

$$y^b[n] = \sum_{k=0}^p \tilde{a}_p^*[k] x[n-p+k] = \mathbf{x}_p^T[n] \mathbf{J} \tilde{\mathbf{a}}_p^* = \tilde{\mathbf{a}}_p^H \mathbf{J} \mathbf{x}_p[n]. \quad (2.12)$$

A symbol with a tilde above it, such as \tilde{a} , means that it is related used for the modified covariance case. The LS-based modified covariance case combines both the forward and backward filter variances to form the total variance estimate over the interval $p + 1 \leq n \leq N$, when normalized by $1/[2(N - p)]$, which is

$$\begin{aligned}\hat{\tilde{\rho}}_p &= \frac{1}{2(N - p)} \sum_{n=p+1}^N |y^f[n]|^2 + |y^b[n]|^2 \\ &= \frac{1}{2(N - p)} \tilde{\mathbf{a}}_p^H \left(\sum_{n=p+1}^N \mathbf{x}_p^*[n] \mathbf{x}_p^T[n] + \mathbf{J} \mathbf{x}_p[n] \mathbf{x}_p^H[n] \mathbf{J} \right) \tilde{\mathbf{a}}_p \\ &= \frac{1}{2(N - p)} \tilde{\mathbf{a}}_p^H (\mathbf{X}_p^H \mathbf{X}_p + \mathbf{J} \mathbf{X}_p^T \mathbf{X}_p^* \mathbf{J}) \tilde{\mathbf{a}}_p\end{aligned}\quad (2.13)$$

in which \mathbf{X}_p is the $(N - p) \times (p + 1)$ rectangular Toeplitz data matrix defined in Eq. 2.8. This forms the basis of the modified covariance LS-based MVSE. Minimizing the estimated variance in Eq. 2.13 subject to the same unit gain constraint as used in the covariance LS-based MVSE of the previous section then yields the following modified covariance LS-based MVSE

$$\hat{\tilde{P}}_{\text{MV-mod}}(f) = \frac{T}{\mathbf{e}_p^H(f) \hat{\tilde{\mathbf{R}}}_p^{-1} \mathbf{e}_p(f)} \quad (2.14)$$

in which the $(p + 1) \times (p + 1)$ *near-to-Toeplitz* matrix (it is composed of sum of products of Toeplitz data matrices) is

$$\begin{aligned}\hat{\tilde{\mathbf{R}}}_p &= (\mathbf{X}_p^H \mathbf{X}_p + \mathbf{J} \mathbf{X}_p^T \mathbf{X}_p^* \mathbf{J}) \\ &= \begin{pmatrix} \hat{\tilde{r}}_p[0, 0] & \cdots & \hat{\tilde{r}}_p[0, p] \\ \vdots & \ddots & \vdots \\ \hat{\tilde{r}}_p[p, 0] & \cdots & \hat{\tilde{r}}_p[p, p] \end{pmatrix}\end{aligned}\quad (2.15)$$

in which $\hat{\tilde{r}}_p[i, j] = \sum_{m=p+1}^N (x^*[m - i] x[m - j] + x[N - m + 1 + i] x^*[N - m + 1 + j])$ for $0 \leq i, j \leq p$. Also $\hat{\tilde{\mathbf{R}}}_p$ is centrosymmetric and hermitian since

$$\hat{\tilde{\mathbf{R}}}_p = \mathbf{J} \hat{\tilde{\mathbf{R}}}_p^* \mathbf{J}, \quad \hat{\tilde{\mathbf{R}}}_p = \hat{\tilde{\mathbf{R}}}_p^H.$$

3. FAST SOLUTIONS FOR ONE-DIMENSIONAL MINIMUM VARIANCE SPECTRAL ESTIMATION

This chapter will present the development of the two new fast computational solutions of the 1-D LS-based MVSE in both the covariance and the modified covariance cases, whose flowcharts are illustrated in Fig. 1.2 and Fig. 1.3. We will first review the fast computational solution of the 1-D ACS-based MVSE.

3.1. Autocorrelation-Based 1-D Minimum Variance Spectral Estimation: Toeplitz Autocorrelation Case

3.1.1. Review Fast Computational Solution

A fast computational algorithm, attributed to Musicus [13], is obtained by first noting that the inverse of the Toeplitz autocorrelation matrix can be expressed as the following difference of products of triangular Toeplitz matrices

$$\mathbf{R}_p^{-1} = \frac{1}{\rho_p^{AR}} \mathbf{A}_p \mathbf{A}_p^H - \frac{1}{\rho_p^{AR}} \mathbf{B}_p \mathbf{B}_p^H \quad (3.1)$$

in which the $(p+1) \times (p+1)$ triangular Toeplitz matrices

$$\mathbf{A}_p = \begin{pmatrix} 1 & 0 & \cdots & 0 & 0 \\ a_p[1] & 1 & \cdots & 0 & 0 \\ \vdots & \ddots & \ddots & \vdots & \vdots \\ a_p[p-1] & a_p[p-2] & \ddots & 1 & 0 \\ a_p[p] & a_p[p-1] & \cdots & a_p[1] & 1 \end{pmatrix}$$

$$\mathbf{B}_p = \begin{pmatrix} 0 & 0 & \cdots & 0 & 0 \\ a_p^*[p] & 0 & \cdots & 0 & 0 \\ \vdots & \ddots & \ddots & \vdots & \vdots \\ a_p^*[2] & a_p^*[3] & \ddots & 0 & 0 \\ a_p^*[1] & a_p^*[2] & \cdots & a_p^*[p] & 0 \end{pmatrix}$$

are composed of AR parameters $a_p[m]$ for $1 \leq m \leq p$, defined as the solution to

$$\mathbf{R}_p \begin{pmatrix} 1 \\ a_p[1] \\ \vdots \\ a_p[p] \end{pmatrix} = \begin{pmatrix} \rho_p^{AR} \\ 0 \\ \vdots \\ 0 \end{pmatrix} \quad (3.2)$$

The AR parameters and white noise variance ρ_p^{AR} are estimated from either the Yule-Walker method, using the known ACS or the estimated ACS, or from the Burg lattice algorithm. Substituting Eq. 3.1 for the inverse matrix into Eq. 2.5 yields, after extensive algebra,

$$P_{\text{MV-acs}}(f) = \frac{T}{\sum_{k=-p}^p \psi_{\text{MV-acs}}[k] \exp(-j2\pi f k T)} \quad (3.3)$$

in which the complex conjugate symmetric coefficients $\psi_{\text{MV-acs}}[k] = \psi_{\text{MV-acs}}^*[-k]$ for $-p \leq k \leq -1$ are weighted correlations of the AR parameters

$$\psi_{\text{MV-acs}}[k] = \frac{1}{\rho_p} \sum_{i=0}^{p-k} (p+1-k-2i) a_p[k+i] a_p^*[i] \quad (3.4)$$

over the interval $0 \leq k \leq p$. An examination of the denominator of Eq. 3.3 shows that it has the form of a discrete time Fourier transform (DTFT), thus a FFT can be used to evaluate it. Also, FFTs can be used for a fast correlation computation of Eq. 3.4.

3.1.2. Computation and Storage Counts

Table 3.1 summarizes the savings in computational complexity and memory storage required by the fast 1-D ACS-based MVSE in Eq. 3.3 versus that required by the direct method in Eq. 2.5. The computational complexity of the fast solution of the 1-D ACS-based MVSE is proportional to p^2 , with memory storage requirements proportional to p , versus p^3 computational complexity and p^2 storage if solved by the direct solution approach.

1-D ACS-based MVSE			
		Fast Solution	Direct Method
Computational Complexity	\times	$\frac{13}{8}p^2 + N_f \log_2(N_f)$	$\frac{2}{3}p^3 + \frac{5}{3}p^2 - \frac{1}{3}p + N_f^2$
	$+$	$\frac{3}{2}p^2 + N_f \log_2(N_f)$	$\frac{2}{3}p^3 - \frac{2}{3}p + N_f^2$
Storage		$3p + 2 + N_f$	$p^2 + N_f$

TABLE 3.1. Comparison of the Computation Complexity and Storage Counts for 1-D ACS-Based MVSE. Note: p is the order of the estimator, N is the number of data sequence, N_f is the number of FFT frequency bins, \times is the number of complex multiplications, and $+$ is the number of complex additions.

3.2. Least-Squares-Based 1-D Minimum Variance Spectral Estimation: Covariance Case

3.2.1. Development of Fast Computational Solution

A new fast algorithm for evaluating the covariance LS-based MVSE is inspired by the highly structured inverse Toeplitz autocorrelation matrix for the

known ACS case of the previous section. We present here the discovery that the inverse of the *near-to-Toeplitz* data product matrix, $\hat{\mathbf{R}}_p^{-1}$, in Eq. 2.11 can also be expressed in terms of a sum of products of triangular Toeplitz matrices formed by the estimated LP parameters, which are recursively computed by Marple's fast algorithm [15]. The structure of the least squares covariance inverse also leads to a modified denominator in which an FFT will then be used to evaluate the denominator of the covariance LS-based MVSE, $P_{\text{MV-cov}}(f)$, in Eq. 2.11.

Based on Eq. 2.9, the crucial partitions needed for the development of the fast algorithm of the covariance LS-based MVSE are the following order-index partitions of the matrix $\hat{\mathbf{R}}_p$ of dimension $(p+1) \times (p+1)$

$$\hat{\mathbf{R}}_p = \begin{pmatrix} \hat{\mathbf{R}}_{p-1}' & \hat{\mathbf{r}}_p' \\ \hat{\mathbf{r}}_p'^H & \hat{r}_p[p, p] \end{pmatrix} \quad (3.5)$$

and

$$\hat{\mathbf{R}}_p = \begin{pmatrix} \hat{r}_p[0, 0] & \hat{\mathbf{r}}_p''^H \\ \hat{\mathbf{r}}_p'' & \hat{\mathbf{R}}_{p-1}'' \end{pmatrix} \quad (3.6)$$

in which the dimension- p column vectors are $\hat{\mathbf{r}}_p'^H = (\hat{r}_p[p, 0] \cdots \hat{r}_p[p, p-1])$ and $\hat{\mathbf{r}}_p''^H = (\hat{r}_p[0, 1] \cdots \hat{r}_p[0, p])$. The $\hat{\mathbf{R}}_{p-1}'$ and $\hat{\mathbf{R}}_{p-1}''$ are square hermitian matrices

$$\hat{\mathbf{R}}_{p-1}' = \hat{\mathbf{R}}_{p-1}'^H, \quad \hat{\mathbf{R}}_{p-1}'' = \hat{\mathbf{R}}_{p-1}''^H.$$

Also crucial are the following time-index partitions

$$\hat{\mathbf{R}}_p' = \sum_{n=p+2}^N \mathbf{x}_p^*[n] \mathbf{x}_p^T[n] = \hat{\mathbf{R}}_p - \mathbf{x}_p^*[p+1] \mathbf{x}_p^T[p+1]$$

and

$$\hat{\mathbf{R}}_p'' = \sum_{n=p+1}^{N-1} \mathbf{x}_p^*[n] \mathbf{x}_p^T[n] = \hat{\mathbf{R}}_p - \mathbf{x}_p^*[N] \mathbf{x}_p^T[N].$$

A pair of auxiliary $(p+1) \times 1$ vectors $\bar{\mathbf{c}}_p^T = (\bar{c}_p[0] \cdots \bar{c}_p[p])$ and $\bar{\mathbf{d}}_p^T = (\bar{d}_p[0] \cdots \bar{d}_p[p])$ are also needed in the development of the fast algorithm. These are defined by

$$\hat{\mathbf{R}}_p \bar{\mathbf{c}}_p = \mathbf{x}_p^*[N], \quad \hat{\mathbf{R}}_p \bar{\mathbf{d}}_p = \mathbf{x}_p^*[p+1].$$

Minimizing the estimated variance $\hat{\rho}_p$ in Eq. 2.7 by least squares minimization then yields the dimension- $(p+1)$ normal equations [15]

$$\hat{\mathbf{R}}_p \begin{pmatrix} 1 \\ \bar{\mathbf{a}}_p \end{pmatrix} = \begin{pmatrix} \bar{\rho}_p^a \\ \mathbf{0}_p \end{pmatrix} \quad (3.7)$$

$$\hat{\mathbf{R}}_p \begin{pmatrix} \mathbf{J} \bar{\mathbf{b}}_p \\ 1 \end{pmatrix} = \begin{pmatrix} \mathbf{0}_p \\ \bar{\rho}_p^b \end{pmatrix} \quad (3.8)$$

in which $\mathbf{0}_p$ is a $p \times 1$ all-zeros column vector. The parameters $\bar{\rho}_p^a$ and $\bar{\rho}_p^b$ are the forward and backward LP error variance estimates, which are positive and real-valued scalars. Substituting the special matrix partitions Eq. 3.5 and Eq. 3.6 into the left sides of normal equations Eq. 3.8 and Eq. 3.7 yields, respectively,

$$\begin{pmatrix} \hat{\mathbf{R}}_{p-1}' & \hat{\mathbf{r}}_p' \\ \hat{\mathbf{r}}_p'^H & \hat{r}_p[p, p] \end{pmatrix} \begin{pmatrix} \mathbf{J} \bar{\mathbf{b}}_p \\ 1 \end{pmatrix} = \begin{pmatrix} \mathbf{0}_p \\ \bar{\rho}_p^b \end{pmatrix} \quad (3.9)$$

$$\begin{pmatrix} \hat{r}_p[0, 0] & \hat{\mathbf{r}}_p''^H \\ \hat{\mathbf{r}}_p'' & \hat{\mathbf{R}}_{p-1}'' \end{pmatrix} \begin{pmatrix} 1 \\ \bar{\mathbf{a}}_p \end{pmatrix} = \begin{pmatrix} \bar{\rho}_p^a \\ \mathbf{0}_p \end{pmatrix}. \quad (3.10)$$

The following relations can be derived from Eq. 3.9 and Eq. 3.10

$$\begin{aligned}\hat{\mathbf{r}}'_p &= -\hat{\mathbf{R}}_{p-1}' \mathbf{J} \bar{\mathbf{b}}_p, & \bar{\rho}_p^b - \hat{r}_p[p, p] &= \hat{\mathbf{r}}_p'^H \mathbf{J} \bar{\mathbf{b}}_p, \\ \hat{\mathbf{r}}''_p &= -\hat{\mathbf{R}}_{p-1}'' \bar{\mathbf{a}}_p, & \bar{\rho}_p^a - \hat{r}_p[0, 0] &= \hat{\mathbf{r}}_p''^H \bar{\mathbf{a}}_p.\end{aligned}$$

By using the partitioned matrix inversion lemma and the augmented matrix inversion lemma [15], the inverse matrix of Eq. 3.5 can be written as

$$\hat{\mathbf{R}}_p^{-1} = \begin{pmatrix} \hat{\mathbf{R}}_{p-1}'^{-1} + \hat{\mathbf{R}}_{p-1}'^{-1} \hat{\mathbf{r}}_p' \Delta^{-1} \hat{\mathbf{r}}_p'^H \hat{\mathbf{R}}_{p-1}'^{-1}, & -\hat{\mathbf{R}}_{p-1}'^{-1} \hat{\mathbf{r}}_p' \Delta^{-1} \\ -\Delta^{-1} \hat{\mathbf{r}}_p'^H \hat{\mathbf{R}}_{p-1}'^{-1}, & -\Delta^{-1} \end{pmatrix} \quad (3.11)$$

in which

$$\Delta = \hat{r}_p[p, p] - \hat{\mathbf{r}}_p'^H \hat{\mathbf{R}}_{p-1}'^{-1} \hat{\mathbf{r}}_p' = \hat{r}_p[p, p] + \hat{\mathbf{r}}_p'^H \mathbf{J} \bar{\mathbf{b}}_p = \bar{\rho}_p^b.$$

Noting that $\Delta^{-1} = 1/\bar{\rho}_p^b$, then $\hat{\mathbf{R}}_p^{-1}$ can be rewritten as

$$\hat{\mathbf{R}}_p^{-1} = \begin{pmatrix} \hat{\mathbf{R}}_{p-1}'^{-1} + \mathbf{J} \bar{\mathbf{b}}_p \bar{\mathbf{b}}_p^H \mathbf{J} & \mathbf{J} \bar{\mathbf{b}}_p \\ \bar{\mathbf{b}}_p^H \mathbf{J} & 1 \end{pmatrix} \frac{1}{\bar{\rho}_p^b}. \quad (3.12)$$

Also,

$$\begin{aligned}\hat{\mathbf{R}}_{p-1}'^{-1} &= \hat{\mathbf{R}}_{p-1}^{-1} + \frac{\hat{\mathbf{R}}_{p-1}^{-1} \mathbf{x}_{p-1}^*[p] \mathbf{x}_{p-1}^T[p] \hat{\mathbf{R}}_{p-1}^{-1}}{1 - \mathbf{x}_{p-1}^T[p] \hat{\mathbf{R}}_{p-1}^{-1} \mathbf{x}_{p-1}^*[p]} \\ &= \hat{\mathbf{R}}_{p-1}^{-1} + \frac{\bar{\mathbf{d}}_{p-1} \bar{\mathbf{d}}_{p-1}^H}{1 - \gamma_{p-1}^d}\end{aligned}$$

in which $\gamma_{p-1}^d = \mathbf{x}_{p-1}^T[p] \hat{\mathbf{R}}_{p-1}^{-1} \mathbf{x}_{p-1}^*[p]$ is a positive real-valued scalar in the range $[0, 1]$. Define the gain adjustment factor of $\bar{\mathbf{d}}$ as $\bar{\rho}_{p-1}^d = 1 - \gamma_{p-1}^d$, also bound between 0 and 1, so that Eq.3.11 may be expressed as

$$\hat{\mathbf{R}}_p^{-1} = \begin{pmatrix} \hat{\mathbf{R}}_{p-1}^{-1} + \bar{\mathbf{d}}_{p-1} \bar{\mathbf{d}}_{p-1}^H / \bar{\rho}_{p-1}^d + \mathbf{J} \bar{\mathbf{b}}_p \bar{\mathbf{b}}_p^H \mathbf{J} / \bar{\rho}_p^b, & \mathbf{J} \bar{\mathbf{b}}_p / \bar{\rho}_p^b \\ \bar{\mathbf{b}}_p^H \mathbf{J} / \bar{\rho}_p^b, & 1 / \bar{\rho}_p^b \end{pmatrix}. \quad (3.13)$$

Similarly the inverse matrix of Eq. 3.6 may be written as

$$\hat{\mathbf{R}}_p^{-1} = \begin{pmatrix} 1/\bar{\rho}_p^a, & \bar{\mathbf{a}}_p^H/\bar{\rho}_p^a \\ \bar{\mathbf{a}}_p/\bar{\rho}_p^a, & \hat{\mathbf{R}}_{p-1}^{-1} + \bar{\mathbf{c}}_{p-1}\bar{\mathbf{c}}_{p-1}^H/\bar{\rho}_{p-1}^c + \bar{\mathbf{a}}_p\bar{\mathbf{a}}_p^H/\bar{\rho}_p^a \end{pmatrix} \quad (3.14)$$

in which the gain adjustment factor of $\bar{\mathbf{c}}$ is $\bar{\rho}_{p-1}^c = 1 - \gamma_{p-1}^c$, where $\gamma_{p-1}^c = \mathbf{x}_{p-1}^H[N]\hat{\mathbf{R}}_{p-1}^{-1}\mathbf{x}_{p-1}[N]$ is a positive real-valued scalar in the range $[0, 1]$. Assume $\bar{u}_p[j, k]$ is an element of $\hat{\mathbf{R}}_p^{-1}$. From the above, the following relations may be found

$$\begin{aligned} \bar{u}_p[0, 0] &= 1/\bar{\rho}_p^a, \quad \bar{u}_p[p, p] = 1/\bar{\rho}_p^b, \quad \bar{u}_p[j, 0] = \bar{a}_p[j]/\bar{\rho}_p^a, \quad \bar{u}_p[0, k] = \bar{a}_p^*[k]/\bar{\rho}_p^a, \\ \bar{u}_p[p, p-k] &= \bar{b}_p^*[k]/\bar{\rho}_p^b, \quad \bar{u}_p[p-j, p] = \bar{b}_p[j]/\bar{\rho}_p^b \end{aligned}$$

for $1 \leq j, k \leq p$, and

$$\begin{aligned} \bar{u}_p[j, k] &= \bar{u}_{p-1}[j, k] + \bar{d}_{p-1}[j]\bar{d}_{p-1}^*[k]/\bar{\rho}_{p-1}^d + \bar{b}_p[p-j]\bar{b}_p^*[p-k]/\bar{\rho}_p^b, \\ \bar{u}_p[j+1, k+1] &= \bar{u}_{p-1}[j, k] + \bar{c}_{p-1}[j]\bar{c}_{p-1}^*[k]/\bar{\rho}_{p-1}^c + \bar{a}_p[j+1]\bar{a}_p^*[k+1]/\bar{\rho}_p^a \end{aligned}$$

for $0 \leq j, k \leq p-1$. Combine the last two equations to eliminate $\bar{u}_{p-1}[j, k]$, yielding

$$\begin{aligned} \bar{u}_p[j+1, k+1] &= \bar{u}_p[j, k] + \bar{a}_p[j+1]\bar{a}_p^*[k+1]/\bar{\rho}_p^a - \bar{b}_p[p-j]\bar{b}_p^*[p-k]/\bar{\rho}_p^b \\ &\quad + \bar{\mathbf{c}}_{p-1}[j]\bar{\mathbf{\Phi}}_{p-1}^{-1}\bar{\mathbf{c}}_{p-1}^H[k] \end{aligned} \quad (3.15)$$

in which $\bar{\mathbf{c}}_{p-1} = (\bar{\mathbf{d}}_{p-1} \quad \bar{\mathbf{c}}_{p-1})$ is of dimension $(p+1) \times 2$, where $\bar{\mathbf{c}}_{p-1}[m] = (\bar{d}_{p-1}[m] \quad \bar{c}_{p-1}[m])$ for $0 \leq m \leq p-1$ is a 1×2 row vector, and the 2×2 diagonal matrix

$$\bar{\mathbf{\Phi}}_p = \begin{pmatrix} -\bar{\rho}_p^d & 0 \\ 0 & \bar{\rho}_p^c \end{pmatrix}$$

contains the gain adjustment factors $\bar{\rho}_p^d$ and $\bar{\rho}_p^c$ of $\bar{\mathbf{d}}$ and $\bar{\mathbf{c}}$, respectively. These are positive real-valued scalars in the range $[0, 1]$. Eq. 3.15 is a recursive relationship that permits all inverse elements to be computed from knowledge of only the LP parameters $\bar{\mathbf{a}}_p$ and $\bar{\mathbf{b}}_p$. The following matrix inverse may also be deduced from Eq. 3.15

$$\hat{\mathbf{R}}_p^{-1} = \frac{1}{\bar{\rho}_p^a} \bar{\mathbf{A}}_p \bar{\mathbf{A}}_p^H - \frac{1}{\bar{\rho}_p^b} \bar{\mathbf{B}}_p \bar{\mathbf{B}}_p^H + \bar{\mathbf{C}}_{p-1} \bar{\mathbf{P}}_{p-1}^{-1} \bar{\mathbf{C}}_{p-1}^H, \quad (3.16)$$

in which the $(p+1) \times (p+1)$ triangular Toeplitz matrices

$$\bar{\mathbf{A}}_p = \begin{pmatrix} 1 & 0 & \cdots & 0 & 0 \\ \bar{a}_p[1] & 1 & \cdots & 0 & 0 \\ \vdots & \ddots & \ddots & \vdots & \vdots \\ \bar{a}_p[p-1] & \bar{a}_p[p-2] & \ddots & 1 & 0 \\ \bar{a}_p[p] & \bar{a}_p[p-1] & \cdots & \bar{a}_p[1] & 1 \end{pmatrix}$$

$$\bar{\mathbf{B}}_p = \begin{pmatrix} 0 & 0 & \cdots & 0 & 0 \\ \bar{b}_p[p] & 0 & \cdots & 0 & 0 \\ \vdots & \ddots & \ddots & \vdots & \vdots \\ \bar{b}_p[2] & \bar{b}_p[3] & \ddots & 0 & 0 \\ \bar{b}_p[1] & \bar{b}_p[2] & \cdots & \bar{b}_p[p] & 0 \end{pmatrix}$$

the $(p+1) \times 2(p+1)$ triangular Toeplitz matrix

$$\bar{\mathbf{C}}_{p-1} = \begin{pmatrix} \mathbf{0} & \mathbf{0} & \cdots & \mathbf{0} & \mathbf{0} \\ \bar{\mathbf{c}}_{p-1}[0] & \mathbf{0} & \cdots & \mathbf{0} & \mathbf{0} \\ \vdots & \ddots & \ddots & \vdots & \vdots \\ \bar{\mathbf{c}}_{p-1}[p-2] & \bar{\mathbf{c}}_{p-1}[p-3] & \ddots & \mathbf{0} & \mathbf{0} \\ \bar{\mathbf{c}}_{p-1}[p-1] & \bar{\mathbf{c}}_{p-1}[p-2] & \cdots & \bar{\mathbf{c}}_{p-1}[0] & \mathbf{0} \end{pmatrix}$$

in which $\mathbf{0}$ is a 1×2 all-zero row vector element, and the $2(p+1) \times 2(p+1)$ block diagonal matrix is

$$\bar{\mathbf{P}}_{p-1}^{-1} = \begin{pmatrix} \bar{\Phi}_{p-1}^{-1} & \cdots & \mathbf{0} \\ \vdots & \ddots & \vdots \\ \mathbf{0} & \cdots & \bar{\Phi}_{p-1}^{-1} \end{pmatrix}$$

in which the all-zero block matrices $\mathbf{0}$ are of dimension 2×2 in this case. These matrices are formed from the forward LP parameters $\bar{\mathbf{a}}_p$, the forward LP error variance $\bar{\rho}_p^a$, the backward LP parameters $\bar{\mathbf{b}}_p$, the backward LP error variance $\bar{\rho}_p^b$, the 1×2 gain adjustment parameters $\bar{\mathbf{c}}_{p-1}[m]$, and the 2×2 gain adjustment matrix $\bar{\Phi}_{p-1}$. All of these parameters and factors are computed recursively as part of a normal execution of the fast computational solution to the least-squares-based covariance case of LP [15]. Substituting Eq. 3.16 into Eq. 2.11, the complex conjugate symmetric $\bar{\psi}_{\text{MV}}[k]$ coefficients lead to the following alternative relationship for the covariance LS-based MVSE

$$\hat{P}_{\text{MV-cov}}(f) = \frac{T}{\sum_{k=-p}^p \hat{\psi}_{\text{MV}}[k] \exp(-j2\pi f k T)} \quad (3.17)$$

in which the weighted autocorrelations of the LP parameters form the coefficients

$$\begin{aligned} \hat{\psi}_{\text{MV}}[k] = & \sum_{i=0}^{p-k} \frac{1}{\bar{\rho}_p^a} (p+1-k-i) \bar{a}_p[k+i] \bar{a}_p^*[i] - \frac{1}{\bar{\rho}_p^b} i \bar{b}_p[i] \bar{b}_p^*[k+i] \\ & + (p-k-i) \bar{\mathbf{c}}_{p-1}[k+i] \bar{\Phi}_{p-1}^{-1} \bar{\mathbf{c}}_{p-1}^H[i] \end{aligned} \quad (3.18)$$

for $0 \leq k \leq p$. Note that $\hat{\psi}_{\text{MV}}[k] = \hat{\psi}_{\text{MV}}^*[-k]$ for $-p \leq k \leq -1$. The following are additional useful mathematical facts: (a) $\bar{a}_p[0] = \bar{b}_p[0] = 1$ and $\bar{\mathbf{c}}_{p-1}[p] = [0 \ 0]$ by definition; (b) vector $\bar{\mathbf{c}}_{p-1}[0] = (\bar{d}_{p-1}[0] \ \bar{c}_{p-1}[0])$ is non-zero; (c) when calculating the LP parameters and the gain adjustment parameters, the maximum order p_{max} must satisfy $p_{\text{max}} < (N-1)/2$, otherwise $\hat{\mathbf{R}}_p$ is not invertible because the dimension of \mathbf{X}_p in Eq. 2.8 is $(N-p) \times (p+1)$.

3.2.2. Computation and Storage Counts

The computation and storage counts are summarized in Table 3.2. The new algorithm requires a number of multiplication operations and addition operations proportional to p^2 in order to calculate the set of $\bar{\psi}_{MV}[k]$ coefficients, for $0 \leq k \leq p$. An FFT is applied to the denominator of Eq. 3.17 to evaluate the LS-based MVSE over a range of frequencies $(-1/2T, 1/2T)$ in Hz. It only requires memory proportional to p storage values to save all of the parameters. This significantly reduces computational complexity and memory storage, compared with the direct evaluation method Eq. 2.11 that has computational complexity and memory storage requirements proportional to p^3 and p^2 , respectively. In Table 3.2, the computational complexity of the direct approach refers to the method described in [3].

1-D LS-based MVSE (Covariance Case)		
	Fast Solution	Direct Method
Computational	$\times \frac{23}{2}p^2 + (2N + \frac{47}{2})p + 3N + N_f \log_2(N_f)$	$\frac{2}{3}p^3 + (\frac{10}{3} + N_f)p^2 + (4 + N + 3N_f)p + (N + 2N_f)$
Complexity	$+ -\frac{1}{2}p^2 + (5N + \frac{23}{2})p + N + N_f \log_2(N_f)$	$\frac{2}{3}p^3 + (1 + N_f)p^2 - (\frac{2}{3} - N - 2N_f)p + N$
Storage	$5p + 13N + N_f$	$p^2 + (4 + N)p + N + N_f$

TABLE 3.2. Comparison of the Computation Complexity and Storage Counts for 1-D Covariance LS-Based MVSE. Note: p is the order of the estimator, N is the number of data sequence, N_f is the number of FFT frequency bins, \times is the number of complex multiplications, and $+$ is the number of complex additions. Note that the maximum order p_{max} must satisfy $p_{max} < (N - 1)/2$ for $\hat{\mathbf{R}}_p^{-1}$ exist.

3.3. Least-Squares-Based 1-D Minimum Variance Spectral Estimation: Modified Covariance Case

3.3.1. Development of Fast Computational Solution

In this section, we show the development of the inverse of the *near-to-Toeplitz* data product matrix, $\hat{\hat{\mathbf{R}}}_p^{-1}$ in Eq. 2.14, for the LS-based modified covariance case. The LP parameters have been recursively solved by Marple's fast algorithm [27].

Based on Eq. 2.15, the crucial partitions needed for the development of the fast algorithm of the modified covariance LS-based MVSE are the following order-index partitions of the $(p+1) \times (p+1)$ matrix $\hat{\hat{\mathbf{R}}}_p$

$$\hat{\hat{\mathbf{R}}}_p = \begin{pmatrix} \hat{\hat{\mathbf{R}}}_{p-1}' & \hat{\mathbf{r}}_p \\ \hat{\mathbf{r}}_p^H & \hat{r}_p[p, p] \end{pmatrix} \quad (3.19)$$

and

$$\hat{\hat{\mathbf{R}}}_p = \begin{pmatrix} \hat{r}_p[0, 0] & \hat{\mathbf{r}}_p^T \mathbf{J} \\ \mathbf{J} \hat{\mathbf{r}}_p^* & \mathbf{J} \hat{\hat{\mathbf{R}}}_{p-1}' \mathbf{J} \end{pmatrix} \quad (3.20)$$

in which

$$\hat{\hat{\mathbf{R}}}_p' = \sum_{n=p+2}^N (\mathbf{x}_p^*[n] \mathbf{x}_p^T[n] + \mathbf{J} \mathbf{x}_p[n] \mathbf{x}_p^H[n] \mathbf{J})$$

and the p -dimensional column vector $\hat{\mathbf{r}}_p^T = (\hat{r}_p[p, 0] \cdots \hat{r}_p[p, p-1])$. Note that $\hat{r}_p[p, p] = \hat{r}_p[0, 0] = \sum_{n=p+1}^N (|x[n]|^2 + |x[n-p]|^2)$ are real-valued scalars. The $\hat{\hat{\mathbf{R}}}_{p-1}'$ is a square hermitian matrix $\hat{\hat{\mathbf{R}}}_{p-1}' = \hat{\hat{\mathbf{R}}}_{p-1}^{'H}$.

Also crucial are the following time-index partitions

$$\hat{\mathbf{R}}_p = \hat{\mathbf{R}}_p' + \mathbf{x}_p^*[p+1]\mathbf{x}_p^T[p+1] + \mathbf{J}\mathbf{x}_p[N]\mathbf{x}_p^H[N]\mathbf{J}$$

and the centrosymmetric variant, $\mathbf{J}\hat{\mathbf{R}}_p^*\mathbf{J} = \hat{\mathbf{R}}_p$,

$$\hat{\mathbf{R}}_p = \mathbf{J}\hat{\mathbf{R}}_p'^*\mathbf{J} + \mathbf{J}\mathbf{x}_p[p+1]\mathbf{x}_p^H[p+1]\mathbf{J} + \mathbf{x}_p^*[N]\mathbf{x}_p^T[N].$$

The pair of auxiliary $(p+1) \times 1$ vectors $\tilde{\mathbf{c}}_p$ and $\tilde{\mathbf{d}}_p$ are also needed in the development of the fast algorithm. They are defined by

$$\hat{\mathbf{R}}_p\tilde{\mathbf{c}}_p = \mathbf{J}\mathbf{x}_p[N], \quad \hat{\mathbf{R}}_p\tilde{\mathbf{d}}_p = \mathbf{x}_p^*[p+1].$$

In an analogous procedure to Eq. 3.7 and Eq. 3.8, minimizing the estimated variance $\hat{\rho}_p$ in Eq. 2.13 yields the following normal equations of dimension $(p+1)$

$$\hat{\mathbf{R}}_p \begin{pmatrix} 1 \\ \tilde{\mathbf{a}}_p \end{pmatrix} = \begin{pmatrix} \tilde{\rho}_p^a \\ \mathbf{0}_p \end{pmatrix} \quad (3.21)$$

$$\hat{\mathbf{R}}_p \begin{pmatrix} \mathbf{J}\tilde{\mathbf{a}}_p^* \\ 1 \end{pmatrix} = \begin{pmatrix} \mathbf{0}_p \\ \tilde{\rho}_p^a \end{pmatrix} \quad (3.22)$$

in which $\mathbf{0}_p$ is a $p \times 1$ all-zeros column vector, and the forward LP error variance estimate $\tilde{\rho}_p^a$ is a positive real-valued scalar. Substituting the special matrix partitions Eq. 3.19 and Eq. 3.20 into the left sides of normal equations Eq. 3.22 and Eq. 3.21 yields, respectively,

$$\begin{pmatrix} \hat{\mathbf{R}}_{p-1}' & \hat{\mathbf{r}}_p \\ \hat{\mathbf{r}}_p^H & \hat{r}_p[p,p] \end{pmatrix} \begin{pmatrix} \mathbf{J}\tilde{\mathbf{a}}_p^* \\ 1 \end{pmatrix} = \begin{pmatrix} \mathbf{0}_p \\ \tilde{\rho}_p^a \end{pmatrix} \quad (3.23)$$

$$\begin{pmatrix} \hat{r}_p[0,0] & \hat{\mathbf{r}}_p^T\mathbf{J} \\ \mathbf{J}\hat{\mathbf{r}}_p^* & \mathbf{J}\hat{\mathbf{R}}_{p-1}'^*\mathbf{J} \end{pmatrix} \begin{pmatrix} 1 \\ \tilde{\mathbf{a}}_p \end{pmatrix} = \begin{pmatrix} \tilde{\rho}_p^a \\ \mathbf{0}_p \end{pmatrix}. \quad (3.24)$$

The following relations can be easily derived from Eq. 3.23 and Eq. 3.24

$$\begin{aligned}\hat{\mathbf{r}}_p &= -\hat{\mathbf{R}}_{p-1}' \mathbf{J} \hat{\mathbf{a}}_p^*, & \tilde{\rho}_p^a - \hat{r}_p[p, p] &= \hat{\mathbf{r}}_p^H \mathbf{J} \hat{\mathbf{a}}_p^*, \\ \mathbf{J} \hat{\mathbf{r}}_p^* &= -\mathbf{J} \hat{\mathbf{R}}_{p-1}'^* \mathbf{J} \hat{\mathbf{a}}_p, & \tilde{\rho}_p^a - \hat{r}_p[0, 0] &= \hat{\mathbf{r}}_p^T \mathbf{J} \hat{\mathbf{a}}_p.\end{aligned}$$

By using the partitioned matrix inversion lemma and the augmented matrix inversion lemma [15], the inverse matrix of Eq. 3.19 can be written as

$$\hat{\mathbf{R}}_p^{-1} = \begin{pmatrix} \hat{\mathbf{R}}_{p-1}'^{-1} + \hat{\mathbf{R}}_{p-1}'^{-1} \hat{\mathbf{r}}_p \Delta^{-1} \hat{\mathbf{r}}_p^H \hat{\mathbf{R}}_{p-1}'^{-1}, & -\hat{\mathbf{R}}_{p-1}'^{-1} \hat{\mathbf{r}}_p \Delta^{-1} \\ -\Delta^{-1} \hat{\mathbf{r}}_p^H \hat{\mathbf{R}}_{p-1}'^{-1}, & \Delta^{-1} \end{pmatrix} \quad (3.25)$$

in which

$$\Delta = \hat{r}_p[p, p] - \hat{\mathbf{r}}_p^H \hat{\mathbf{R}}_{p-1}'^{-1} \hat{\mathbf{r}}_p = \hat{r}_p[p, p] + \hat{\mathbf{r}}_p^H \mathbf{J} \hat{\mathbf{a}}_p^* = \tilde{\rho}_p^a.$$

So $\Delta^{-1} = 1/\tilde{\rho}_p^a$, and $\hat{\mathbf{R}}_p^{-1}$ can be rewritten as

$$\hat{\mathbf{R}}_p^{-1} = \begin{pmatrix} \hat{\mathbf{R}}_{p-1}'^{-1} + \mathbf{J} \hat{\mathbf{a}}_p^* \tilde{\mathbf{a}}_p^T \mathbf{J} & \mathbf{J} \hat{\mathbf{a}}_p^* \\ \tilde{\mathbf{a}}_p^T \mathbf{J} & 1 \end{pmatrix} \frac{1}{\tilde{\rho}_p^a} \quad (3.26)$$

in which

$$\begin{aligned}\hat{\mathbf{R}}_{p-1}'^{-1} &= \hat{\mathbf{R}}_{p-1}^{-1} + \hat{\mathbf{R}}_{p-1}^{-1} \bar{\mathbf{x}}_{p-1}^*[p] \left(-\bar{\mathbf{x}}_{p-1}^T[p] \hat{\mathbf{R}}_{p-1}^{-1} \bar{\mathbf{x}}_{p-1}^*[p] + \mathbf{I}_2 \right)^{-1} \bar{\mathbf{x}}_{p-1}^T[p] \hat{\mathbf{R}}_{p-1}^{-1} \\ &= \hat{\mathbf{R}}_{p-1}^{-1} + \tilde{\mathbf{c}}_{p-1} \tilde{\mathbf{\Phi}}_{p-1}^{-1} \tilde{\mathbf{c}}_{p-1}^H\end{aligned}$$

The matrices $\bar{\mathbf{x}}_p[n] = (\mathbf{x}_p[n] \quad \mathbf{J} \mathbf{x}_p^*[N + p + 1 - n])$ and $\tilde{\mathbf{c}}_p = (\tilde{\mathbf{d}}_p \quad \tilde{\mathbf{c}}_p)$ are each of dimension $(p+1) \times 2$, \mathbf{I}_2 is a 2×2 identity matrix, and the 2×2 hermitian matrix $\tilde{\mathbf{\Phi}}_{p-1}$ is

$$\begin{aligned}
\tilde{\Phi}_{p-1} &= \mathbf{I}_2 - \bar{\mathbf{x}}_{p-1}^T[p] \hat{\mathbf{R}}_{p-1}^{-1} \bar{\mathbf{x}}_{p-1}^*[p] \\
&= \mathbf{I}_2 - \begin{pmatrix} \mathbf{x}_{p-1}^T[p] \\ \mathbf{x}_{p-1}^H[N] \mathbf{J} \end{pmatrix} \hat{\mathbf{R}}_{p-1}^{-1} \begin{pmatrix} \mathbf{x}_{p-1}^*[p] & \mathbf{J} \mathbf{x}_{p-1}[N] \end{pmatrix} \\
&= \mathbf{I}_2 - \begin{pmatrix} \mathbf{x}_{p-1}^T[p] \\ \mathbf{x}_{p-1}^H[N] \mathbf{J} \end{pmatrix} \begin{pmatrix} \tilde{\mathbf{d}}_{p-1} & \tilde{\mathbf{c}}_{p-1} \end{pmatrix} \quad .
\end{aligned}$$

Alternatively, two forms of the inverse of $\hat{\mathbf{R}}_p^{-1}$ may be developed. Eq. 3.25 expresses the inverse

$$\hat{\mathbf{R}}_p^{-1} = \begin{pmatrix} \hat{\mathbf{R}}_{p-1}^{-1} + \tilde{\mathbf{c}}_{p-1} \tilde{\Phi}_{p-1}^{-1} \tilde{\mathbf{c}}_{p-1}^H + \mathbf{J} \tilde{\mathbf{a}}_p^* \tilde{\mathbf{a}}_p^T \mathbf{J} / \tilde{\rho}_p^a, & \mathbf{J} \tilde{\mathbf{a}}_p^* / \tilde{\rho}_p^a \\ \tilde{\mathbf{a}}_p^T \mathbf{J} / \tilde{\rho}_p^a, & 1 / \tilde{\rho}_p^a \end{pmatrix}, \quad (3.27)$$

and Eq. 3.20 may express the inverse as

$$\hat{\mathbf{R}}_p^{-1} = \begin{pmatrix} 1 / \tilde{\rho}_p^a, & \tilde{\mathbf{a}}_p^H / \tilde{\rho}_p^a \\ \tilde{\mathbf{a}}_p / \tilde{\rho}_p^a, & \hat{\mathbf{R}}_{p-1}^{-1} + \mathbf{J} \tilde{\mathbf{c}}_{p-1}^* \tilde{\Phi}_{p-1}^{-1} \tilde{\mathbf{c}}_{p-1}^T \mathbf{J} + \tilde{\mathbf{a}}_p \tilde{\mathbf{a}}_p^H / \tilde{\rho}_p^a \end{pmatrix}. \quad (3.28)$$

Assume $\tilde{u}_p[j, k]$ is an element of $\hat{\mathbf{R}}_p^{-1}$. From above, the following relations may be found

$$\begin{aligned}
\tilde{u}_p[0, 0] &= \tilde{u}_p[p, p] = 1 / \tilde{\rho}_p^a, \quad \tilde{u}_p[j, 0] = \tilde{a}_p[j] / \tilde{\rho}_p^a, \quad \tilde{u}_p[0, k] = \tilde{a}_p^*[k] / \tilde{\rho}_p^a, \\
\tilde{u}_p[p, p-k] &= \tilde{a}_p^*[k] / \tilde{\rho}_p^a, \quad \tilde{u}_p[p-j, p] = \tilde{a}_p[j] / \tilde{\rho}_p^a
\end{aligned}$$

for $1 \leq j, k \leq p$, and

$$\begin{aligned}
\tilde{u}_p[j, k] &= \tilde{u}_{p-1}[j, k] + \tilde{\mathbf{c}}_{p-1}[j] \tilde{\Phi}_{p-1}^{-1} \tilde{\mathbf{c}}_{p-1}^H[k] + \tilde{a}_p^*[p-j] \tilde{a}_p[p-k] / \tilde{\rho}_p^a, \\
\tilde{u}_p[j+1, k+1] &= \tilde{u}_{p-1}[j, k] + \left(\tilde{\mathbf{c}}_{p-1}[p-1-j] \tilde{\Phi}_{p-1}^{-1} \tilde{\mathbf{c}}_{p-1}^H[p-1-k] \right)^* \\
&\quad + \tilde{a}_p[j+1] \tilde{a}_p^*[k+1] / \tilde{\rho}_p^a
\end{aligned}$$

for $0 \leq j, k \leq p-1$. Combine the last two equations to eliminate $\tilde{u}_{p-1}[j, k]$, yielding

$$\begin{aligned} \tilde{u}_p[j+1, k+1] = & \tilde{u}_p[j, k] + \tilde{a}_p[j+1]\tilde{a}_p^*[k+1]/\tilde{\rho}_p^a - \tilde{a}_p^*[p-j]\tilde{a}_p[p-k]/\tilde{\rho}_p^a \quad (3.29) \\ & + \left(\tilde{\mathbf{c}}_{p-1}[p-1-j]\tilde{\mathbf{\Phi}}_{p-1}^{-1}\tilde{\mathbf{c}}_{p-1}^H[p-1-k] \right)^* - \tilde{\mathbf{c}}_{p-1}[j]\tilde{\mathbf{\Phi}}_{p-1}^{-1}\tilde{\mathbf{c}}_{p-1}^H[k]. \end{aligned}$$

Eq. 3.29 is a recursive relationship that permits all inverse elements to be computed from knowledge of only the modified covariance LP parameter vector $\tilde{\mathbf{a}}_p$. The following inverse matrix relationship may also be developed from Eq. 3.29

$$\hat{\mathbf{R}}_p^{-1} = \frac{1}{\tilde{\rho}_p^a} \tilde{\mathbf{A}}_p \tilde{\mathbf{A}}_p^H - \frac{1}{\tilde{\rho}_p^a} \tilde{\mathbf{B}}_p \tilde{\mathbf{B}}_p^H - \tilde{\mathbf{C}}_{p-1} \tilde{\mathbf{P}}_{p-1}^{-1} \tilde{\mathbf{C}}_{p-1}^H + \tilde{\mathbf{D}}_{p-1} \tilde{\mathbf{P}}_{p-1}^{*-1} \tilde{\mathbf{D}}_{p-1}^H \quad (3.30)$$

in which the $(p+1) \times (p+1)$ triangular Toeplitz matrices

$$\tilde{\mathbf{A}}_p = \begin{pmatrix} 1 & 0 & \cdots & 0 & 0 \\ \tilde{a}_p[1] & 1 & \cdots & 0 & 0 \\ \vdots & \ddots & \ddots & \vdots & \vdots \\ \tilde{a}_p[p-1] & \tilde{a}_p[p-2] & \ddots & 1 & 0 \\ \tilde{a}_p[p] & \tilde{a}_p[p-1] & \cdots & \tilde{a}_p[1] & 1 \end{pmatrix}$$

$$\tilde{\mathbf{B}}_p = \begin{pmatrix} 0 & 0 & \cdots & 0 & 0 \\ \tilde{a}_p^*[p] & 0 & \cdots & 0 & 0 \\ \vdots & \ddots & \ddots & \vdots & \vdots \\ \tilde{a}_p^*[2] & \tilde{a}_p^*[3] & \ddots & 0 & 0 \\ \tilde{a}_p^*[1] & \tilde{a}_p^*[2] & \ddots & \tilde{a}_p^*[p] & 0 \end{pmatrix}$$

and the $(p+1) \times 2(p+1)$ triangular vector-block Toeplitz matrices

$$\tilde{\mathbf{C}}_{p-1} = \begin{pmatrix} \mathbf{0} & \mathbf{0} & \cdots & \mathbf{0} & \mathbf{0} \\ \tilde{\mathbf{c}}_{p-1}[0] & \mathbf{0} & \cdots & \mathbf{0} & \mathbf{0} \\ \vdots & \ddots & \ddots & \vdots & \vdots \\ \tilde{\mathbf{c}}_{p-1}[p-2] & \tilde{\mathbf{c}}_{p-1}[p-3] & \ddots & \mathbf{0} & \mathbf{0} \\ \tilde{\mathbf{c}}_{p-1}[p-1] & \tilde{\mathbf{c}}_{p-1}[p-2] & \cdots & \tilde{\mathbf{c}}_{p-1}[0] & \mathbf{0} \end{pmatrix}$$

$$\tilde{\mathbf{D}}_{p-1} = \begin{pmatrix} \mathbf{0} & \mathbf{0} & \cdots & \mathbf{0} & \mathbf{0} \\ \tilde{\mathbf{c}}_{p-1}^*[p-1] & \mathbf{0} & \cdots & \mathbf{0} & \mathbf{0} \\ \vdots & \ddots & \ddots & \vdots & \vdots \\ \tilde{\mathbf{c}}_{p-1}^*[1] & \tilde{\mathbf{c}}_{p-1}^*[2] & \ddots & \mathbf{0} & \mathbf{0} \\ \tilde{\mathbf{c}}_{p-1}^*[0] & \tilde{\mathbf{c}}_{p-1}^*[1] & \cdots & \tilde{\mathbf{c}}_{p-1}^*[p-1] & \mathbf{0} \end{pmatrix}$$

have 1×2 all-zero row vector elements $\mathbf{0}$ and 1×2 row vector elements $\tilde{\mathbf{c}}_{p-1}[m] = (\tilde{d}_{p-1}[m] \tilde{c}_{p-1}[m])$ for $0 \leq m \leq p-1$, and the $2(p+1) \times 2(p+1)$ block diagonal matrix

$$\tilde{\mathbf{P}}_{p-1}^{-1} = \begin{pmatrix} \tilde{\mathbf{\Phi}}_{p-1}^{-1} & \cdots & \mathbf{0} \\ \vdots & \ddots & \vdots \\ \mathbf{0} & \cdots & \tilde{\mathbf{\Phi}}_{p-1}^{-1} \end{pmatrix}$$

which has all-zero block elements $\mathbf{0}$ of 2×2 dimension. These matrices are formed from the modified covariance LP parameter vector $\tilde{\mathbf{a}}_p$, the modified covariance LP error variance estimate $\tilde{\rho}_p^a$, the 2×1 gain adjustment vector parameters $\tilde{\mathbf{c}}_{p-1}[m]$, and 2×2 gain adjustment matrix $\tilde{\mathbf{\Phi}}_{p-1}$. If Eq. 3.30 is substituted into Eq. 2.14, the complex conjugate symmetric $\tilde{\psi}_{\text{MV}}[k]$ coefficients form an alternative formulation of the least-squares-based modified covariance MVSE, in which

$$\hat{\tilde{P}}_{\text{MV-mod}}(f) = \frac{T}{\sum_{k=-p}^p \tilde{\psi}_{\text{MV}}[k] \exp(-j2\pi f k T)} \quad (3.31)$$

and

$$\begin{aligned} \hat{\psi}_{\text{MV}}[k] = & \sum_{i=0}^{p-k} \frac{1}{\tilde{\rho}_p^a} (p+1-k-2i) \tilde{a}_p[k+i] \tilde{a}_p^*[i] \\ & - (p-1-k-2i) \tilde{\mathbf{c}}_{p-1}[k+i] \tilde{\mathbf{\Phi}}_{p-1}^{-1} \tilde{\mathbf{c}}_{p-1}^H[i] \end{aligned} \quad (3.32)$$

for $0 \leq k \leq p$. Note that $\hat{\psi}_{\text{MV}}[k] = \hat{\psi}_{\text{MV}}^*[-k]$ for $-p \leq k \leq -1$. The following additional math facts are: (a) $\tilde{a}_p[0] = 1$ and $\tilde{\mathbf{c}}_{p-1}[p] = [0 \ 0]$ by definition; (b) the 1×2 row vector $\tilde{\mathbf{c}}_{p-1}[0]$ contains non-zero values; (c) when calculating the LP parameters and the gain adjustment parameters, the maximum order p_{\max} must satisfy $p_{\max} < (2N-1)/3$, otherwise $\hat{\mathbf{R}}_p$ is not invertible based on Eq. 3.30.

3.3.2. Computation and Storage Counts

The computation counts are summarized in the Table 3.3. The new algorithm requires a number of multiply operations and a number of add operations proportional to p^2 to calculate the set of $\tilde{\psi}_{\text{MV}}[k]$, $0 \leq k \leq p$, coefficients. An FFT may be used to evaluate the denominator of the LS-based MVSE Eq. 3.31 over a range of frequencies $(-1/2T, 1/2T)$. It only requires memory storage proportional to p in order to save all of the parameters. This significantly reduces the computational complexity and memory storage requirements, compared with the direct evaluation method Eq. 2.14 in which the computational complexity and memory storage requirements are proportional to p^3 and p^2 , respectively. In Table 3.3, the computational complexity of the direct approach refers to the method described in [3].

1-D LS-based MVSE (Modified Covariance Case)			
		Fast Solution	Direct Method
Computational Complexity	×	$-\frac{1}{2}p^2 + (10N + 41)p + 3N + N_f \log_2(N_f)$	$\frac{2}{3}p^3 + (\frac{4}{3} + N_f)p^2 + (3N + 3N_f + 2)p + (2 + N + 2N_f)$
	+	$-p^2 + (10N + \frac{53}{2})p + 2N + N_f \log_2(N_f)$	$\frac{2}{3}p^3 + N_f p^2 + (2N - \frac{8}{3} + 2N_f)p + 2N$
Storage		$10p + 16N + N_f$	$p^2 + (5 + N)p + N + N_f$

TABLE 3.3. Comparison of the Computation Complexity and Storage Counts for 1-D Modified Covariance LS-Based MVSE. Note: p is the order of the estimator, N is the number of data sequence, N_f is the number of FFT frequency bins, \times is the number of complex multiplications, and $+$ is the number of complex additions. Note that the maximum order p_{max} must satisfy $p_{max} < (2N - 1)/3$ for $\hat{\mathbf{R}}_p^{-1}$ exist.

4. IMPROVED-FEATURE DETAIL USING FAST ALGORITHMS FOR ONE-DIMENSIONAL MINIMUM VARIANCE SPECTRAL ESTIMATION

This chapter presents experimental results for four different 1-D data classes to test the performance of the two fast computational algorithms for 1-D LS-based MVSE in the covariance and the modified covariance cases. The narrow-band sinusoid data and the wide-band AR process are common test cases. A narrow-band sinusoidal data set is used to test the resolution capability and the improved-feature detail of each spectral estimation technique. A wide-band AR process is next used to examine the characteristic of the frequency variance and the power spectral density (PSD) variance [15] of our estimators. A simulated Doppler radar data set, generated as a combination of narrow-band and wide-band signals, is next used to evaluate the performance of the two 1-D fast computational solutions with mixed signal components. Finally, the performance of our spectral estimators using an actual 1-D Doppler radar data set is illustrated and analyzed.

4.1. Application One: Narrow-Band Sinusoidal Data

For the sake of a common test case that is analytically easy to understand, the 1-D 64-complex-point signal has been generated as the sum of six 1-D complex sinusoids corrupted by 1-D additive complex Gaussian white noise

$$x[n] = A \left[e^{(-j2\pi f_1 n T)} + e^{(-j2\pi f_2 n T)} + e^{(-j2\pi f_3 n T)} + e^{(-j2\pi f_4 n T)} + e^{(-j2\pi f_5 n T)} + e^{(-j2\pi f_6 n T)} \right] + \omega[n] \quad (4.1)$$

where $T = 1$ sec is the data sample interval, n is the sample index. The frequency axis shown through this thesis is expressed as a dimensionless fraction of the sam-

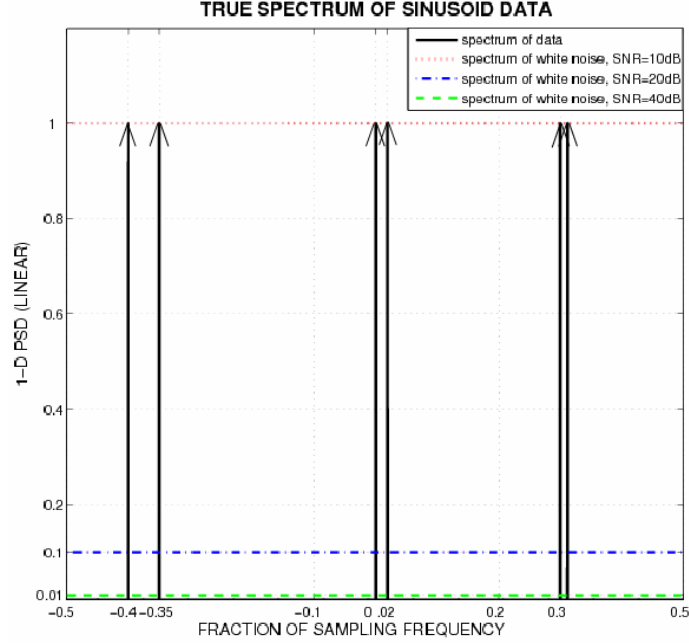


FIGURE 4.1. True spectral density of the six complex sinusoidal signals.

pling frequency, which means that the actual frequency f in Hz is normalized by the sampling frequency $f_s = 1/T$. Due to the sampling theorem for signals, the fractional frequencies must lie between -0.5 and 0.5 . The six sinusoids frequencies correspond to $f_1 = -0.4$, $f_2 = -0.35$, $f_3 = 0$, $f_4 = 0.02$, $f_5 = 0.3$ and $f_6 = 0.312$ in the fraction of sampling frequency axis, and the amplitude $A = 1$. The six sinusoids were carefully chosen for the analytical purpose of representing three different spectral resolution spacings, from a very narrow spacing to a larger spacing. $\omega[n]$ is white Gaussian noise. Fig. 4.1 illustrates the expected true spectral density of the sinusoidal data $x[n]$. Fig. 4.2, Fig. 4.3 and Fig. 4.5 illustrate the spectral estimates based on SNR from 40 dB to 10 dB. In this experiment, the model order $p = 14$, and the number of PSD frequencies $N_f = 7k$. This experiment compared the two fast computational algorithms estimates of the 1-D MVSE in the covariance and the modified covariance cases with the classic

Fourier-based periodogram estimator Eq. 4.2 [15], the AR Yule-Walker estimator Eq. 4.3 [15], and the lattice-Burg MV spectral estimator Eq. 3.3 [15].

$$P_{period}(f) = \frac{1}{N} \left| \sum_{n=0}^{N-1} x[n] e^{(-j2\pi f n T)} \right|^2 \quad (4.2)$$

where $x[n]$, for $0 \leq n \leq N - 1$, is the data vector.

$$P_{AR}(f) = \frac{\rho_p}{|1 + \sum_{k=1}^p a[k] e^{(-j2\pi f k T)}|^2} \quad (4.3)$$

where p is the order of a AR filter, $a[k]$, for $1 \leq k \leq p$, is an AR filter parameter, and ρ_p is the white noise variance of the driving sequence.

In Fig. 4.2, only the fast covariance and the fast modified covariance LS-based MV estimators [Fig. 4.2(d) and (e)] can distinguish the most closely spaced sinusoids located at $f_5 = 0.3$ and $f_6 = 0.312$ fraction of sampling frequency. In addition, their estimates for the other four sinusoids from $f_1 = -0.4$ fraction of sampling frequency through $f_4 = 0.02$ fraction of sampling frequency are sharper than the periodogram estimates, the AR Yule-Walker estimates and the lattice-Burg estimates [Fig. 4.2 (a),(b) and (c)]. Therefore, the two fast solution algorithms of the 1-D LS-based MV spectral estimators achieve $0.02/0.012 \approx 1.67$ times higher resolution than the other three spectral estimators, where 0.02 is the frequency spacing between sinusoids $f_3 = 0.0$ and $f_4 = 0.02$ fraction of sampling frequency, and 0.012 is the frequency spacing between sinusoids $f_5 = 0.3$ and $f_6 = 0.312$ fraction of sampling frequency.

In Fig. 4.3, for a SNR of 20 dB, no method can distinguish the most closely spaced pair of sinusoids at $f_5 = 0.3$ and $f_6 = 0.312$ fraction of sampling frequency. However, the peaks at $f_3 = 0$ and $f_4 = 0.02$ fraction of sampling frequency, as estimated by the fast covariance and the fast modified covariance estimators, Fig. 4.3 (d) and (e), are still sharper than those in Fig. 4.3 (a) (b) and (c), which

can be easily observed in the zoomed figures shown in Fig. 4.4. When the SNR is reduced to 10 dB, only the most widely spaced pair of sinusoids can be resolved in Fig. 4.5. A closeup of Fig. 4.5 the sinusoids at $f_1 = -0.4$ and $f_2 = -0.35$ fraction of sampling frequency, Fig. 4.6, shows that the lattice-Burg estimates Fig. 4.6 (b) has biased frequency peaks which are not exactly at $f_1 = -0.4$ and $f_2 = -0.35$ fraction of sampling frequency. There is no bias in the peak location found in the 1-D fast covariance and the 1-D fast modified covariance estimates [Fig. 4.6 (c) and (d)].

The two new 1-D fast algorithms not only inherit the improved-feature detail from the non-fast direct evaluation versions of the LS-based MVSE, they also generate and optionally save all of the parameters of intermediate order solutions due to the recursive structure of the fast algorithms, which generate all the LP parameters from order 0 to the maximum order p_{max} . If we monitor the output LP error variances ρ_a (forward) and ρ_b (backward), we will observe that they decrease as the order increases, as illustrated in Fig. 4.7. We can select an optimal fitting order (for example, $p_{opt} = 14$ in Fig. 4.7) at the point where either ρ_a or ρ_b has decreased to a desired low level. Since all intermediate order parameter values have been generated, we do not need to recompute to obtain the optimal parameters, as they are already available from the recursive algorithms. It is especially helpful in applications for which the appropriate order is not known a priori. Once the optimal order is selected, the saved parameters can then be used to compute the LS-based MVSE for that selected order. Therefore the two new fast computational solutions of the 1-D LS-based MVSE are both computationally-efficient and order-selectable.

4.2. Application Two: Wide-Band Autoregressive Process

The wide-band AR process, another common test case, is often used in the journal literature to test the PSD variance and the frequency variance of a spectral estimator. In this experiment, the AR(6) process of Eq. 4.4 is generated, with three poles inside the unit circle in Fig. 4.8(a) at $0.2 \pm j0.9$, $0.6 \pm j0.7$ and $0.8 \pm j0.6$:

$$\begin{aligned} x[k] = & -a[1]x[k-1] - a[2]x[k-2] - a[3]x[k-3] \\ & -a[4]x[k-4] - a[5]x[k-5] - a[6]x[k-6] + \omega[k], \end{aligned} \quad (4.4)$$

where the AR parameters are $a[1] = 3.22$, $a[2] = -5.74$, $a[3] = 6.468$, $a[4] = -5.0865$, $a[5] = 2.533$, $a[6] = -0.7225$. $\omega[k]$ is a white Gaussian noise process with variance $\rho_\omega = 0.01$. The true AR spectrum in Fig. 4.8(b) is computed as

$$P_{ar}(f) = \frac{T\rho_\omega}{|1 + \sum_{n=1}^6 a[n]e^{(-j2\pi f n T)}|^2} \quad (4.5)$$

over frequency range $(-1/2T, 1/2T)$ in Hz, where $T = 1$ sec is the sampling interval. The driving noise variance is $\rho_\omega = 0.01$. The spectra of the three pairs of poles should exhibit peaks at ± 0.215 , ± 0.138 and ± 0.093 fraction of sampling frequency along the frequency axis, respectively. Since the AR spectrum is symmetric about 0 fraction of sampling frequency, Fig. 4.8(b) only shows the positive frequency half axis. Fig. 4.9 illustrates overlapped spectral estimates for 50 data realizations of 400 samples each of the AR(6) process. The model order $p = 40$ and the number of PSD frequencies $N_f = 6k$. The 1-D fast covariance estimator in Fig. 4.9(c) and the 1-D fast modified covariance estimates in Fig. 4.9(d) have less frequency variance than the 1-D lattice-Burg estimates in Fig. 4.9(b), which provides less PSD variance. This observation was also reported by Nuttall [5] and Shon and Mehrotra [12]. The larger PSD variance of the LP-based methods may

come from the fact that the linear prediction methods do not require stable pole estimates, unlike the lattice method that restricts the pole estimates to fall only inside the unit circle. The Yule-Walker algorithm generates the poorest estimator of the AR(6) spectrum, which also was observed by Marple in [15].

4.3. Application Three: Simulated Doppler Radar Data

In this experiment, a test case is generated as a combination of both narrow-band and wide-band signals. A 64-complex-point simulated Doppler radar data set [15] is used to test the resolution capability of the two new 1-D fast solutions for the LS-based MVSE. The Doppler frequency F_d is proportional to (Vf_c/c) [29], where V is the radial velocity of an object moving toward/away from a radar, f_c is the carrier frequency (assumed here as 10 GHz), and c is the light speed (3×10^8 m/sec). The true spectrum of the test data, calculated by analytical means, is illustrated in Fig. 4.10(a). The frequency axis is expressed as a fraction of the sampling frequency ($f_s = 2500$ Hz in this simulation). The five stems at -0.3 , -0.1 , 0.2 , 0.21 and 0.4 in the fraction of sampling frequency axis simulate five aircraft flying at different radial velocities toward or away from the radar. The two closest stems with highest power at 0.2 and 0.21 fraction of sampling frequency are used to test the resolution capability of an estimator. The short stem at 0.4 fraction of sampling frequency with lower power is used to test if an estimator can pick out a weak signal component among strong noise content. The colored noise process is created by passing white noise through a filter, (with a truncated cosine shaped frequency response), to simulate typical low frequency clutter effects due as wind (0 to 231 m/h) [37], cloud motions (0 to 100 m/h) [22], flying birds (0 to 100 m/h) [36] and moving traffic on a road (0 to 70 m/h) [38].

The estimator spectral responses produced from the 64-complex-samples are illustrated in Fig. 4.10 for order $p = 12$. In Fig. 4.10(b), the Nuttall window has been used to reduce the sidelobe artifacts in the classical periodogram spectral estimate. The expected resolution of the classic periodogram is $1/64T \div 1/T = 0.0156$ [15, page 134], so it can not resolve the two closest sinusoids at 0.2 and 0.21 fraction of sampling frequency. However these are resolved in Fig. 4.10(d) and even more clearly distinguished in Figs. 4.10(e) and (f), all of which are MVSE estimators. By using the Musicus fast algorithm to evaluate MVSE [13] and the AR Yule-Walker algorithm to estimate the AR parameters, the resulting MVSE in Fig. 4.10(c) does not provide the desired high-resolution result. The sinusoid peak at 0.4 fraction of sampling frequency is even too weak to be trusted. Although the performance of the Musicus algorithm that uses the lattice-based Burg algorithm estimate of the AR parameters, instead of the Yule-Walker-based AR algorithm, provides a better resolved MVSE spectra in Fig. 4.10(d), it has peaks that are biased wider than the spectra estimated by the two new LS-based MVSEs with fast algorithms that are shown in Figs. 4.10(e) and (f). Therefore, the new fast algorithms of the LS-based MVSE achieve improved resolution over the previous ACS-based versions of the MVSE. Moreover, a closeup of the PSD reveals that there is one biased peak in the Burg spectral estimate in Fig. 4.11(a) which is not exactly at 0.21 fraction of sampling frequency. However, the peaks derived by the new fast algorithms are unbiased and align with the correct frequency locations, as shown in Fig. 4.11(b). Furthermore, Fig. 4.12 illustrates that the spectra of the new fast algorithms do not exhibit the spectral line splitting phenomenon of the Burg algorithm [15], as one increases the order p from 12 to 16. For the sake of brevity, only one of the new fast algorithms of the LS-based MVSE is illustrated

in Fig. 4.11 and Fig. 4.12, since both have essentially identical performance for this test case.

4.4. Application Four: Actual 1-D Doppler Radar Data

A test case with 1-D Doppler radar data derived from anechoic chamber radar data echos off an actual truck target is presented here. It is used to validate the improved-feature capability of the two new fast solutions of the 1-D LS-based MVSE. The experimental results show that the two new fast 1-D solutions are able to resolve more scattering centers detected in single lines of a synthetic aperture radar processing of the anechoic chamber data when compared with the 1-D classical periodogram method and the 1-D covariance AR estimator.

Before the experimental results are demonstrated, ISAR radar acquisition and processing steps to create radar images will be briefly described. The radar data was collected in a 10-story microwave anechoic chamber, shown in Fig. 4.13, located in Rancho Bernardo, CA. This data is provided by Dr. Marple with permission to use by the author of this thesis. Radar can use frequencies from 3 MHz to over 40 GHz. A radar system is characterized by its operating frequency. For example, a high frequency (HF) radar can detect targets beyond the horizon by utilizing the ionosphere to reflect electromagnetic waves off of it. Radars in the very high frequency (VHF) range have been used as early warning radar systems. For applications of most medium range radars for ships, aircraft and ground-based units, S-band radars are widely used [35]. The chamber radar data of the truck presented here has been acquired in S-band in the range 3.093 GHz to 3.947 GHz. In the middle of the chamber, the truck was raised on a pylon and slowly rotated on the pylon shown in Fig. 4.13. The rotation is stepped in degrees of azimuth

(the head-on view of the truck is the 0° reference of the azimuth). The radar illuminates the rotating truck with a stepped RF frequency and receives echoed signals from the truck. The acquisition equipment captures the echo signals at every stepped azimuth angle (0.015°) and every stepped frequency (10.67 MHz). Due to azimuth (rotating) data acquisition, the ISAR raw radar data is collected in a polar grid acquisition format. Polar-to-cartesian interpolation is then used to format the ISAR raw data to a uniform rectangular data grid, a requirement needed by all 1-D and 2-D spectral estimation techniques [23] that assume uniformly spaced cartesian data grids (which is the case for the methods described in this thesis).

Fig. 4.14 outlines a diagram of the interpolation and estimation steps for 1-D Doppler data processing (path 2) and 2-D ISAR imagery processing (path 1). In path 1, 2-D radar imagery is obtained by application of a 2-D inverse FFT (IFFT). Alternatively, 2-D spectral estimation techniques can be applied to predict the scattering centers to a greater precision or resolution, which will be introduced in Chapter 7.3. In path 2, 1-D Doppler data is extracted from the acquired and interpolated 2-D data by selecting either one row or one column for processing. Different 1-D spectral estimation techniques are then applied to estimate the spectra of the selected row or column radar data vector. Fig. 4.15 and Fig. 4.16 show the estimated spectra of the selected data at the center of the down range dimension at 3.78 GHz with 200 MHz bandwidth and measurement polarization of $V_T V_R$ which means the target response signal is captured by a vertically polarized transmission V_T and a vertically polarized reception V_R . The model order is $p = 30$ and the number of FFT frequencies is $N_f = 256$. Fig. 4.15 is the processed results at center azimuth angle of 47° , while Fig. 4.16 is processed results at center azimuth angle of 75° . Both results show that the two new fast

solutions of the 1-D LS-based MVSE reveal more and sharper peaks than the 1-D classical periodogram method and the 1-D covariance AR estimator. The results of 2-D estimator will be demonstrated in Chapter 7.3.

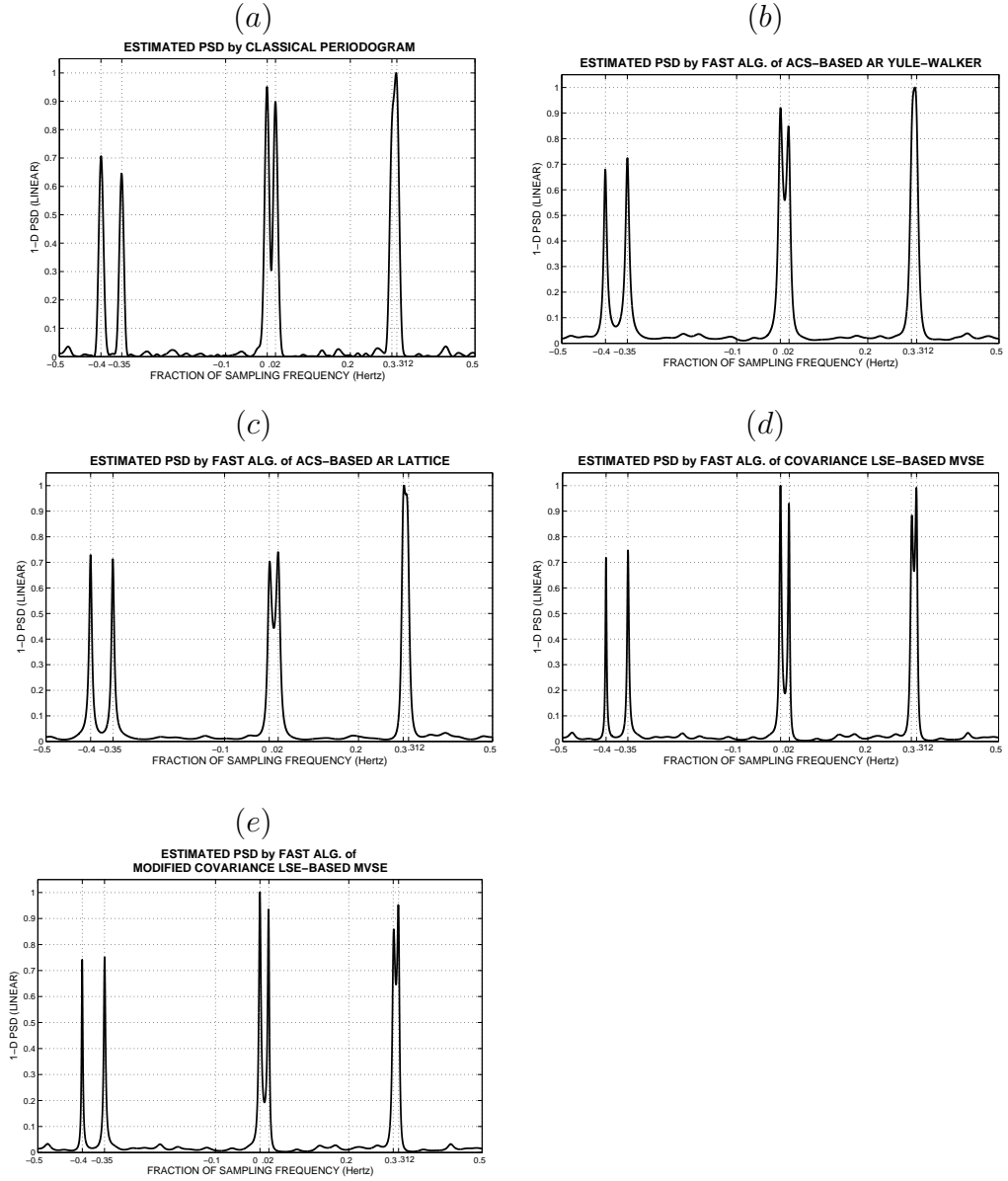


FIGURE 4.2. Comparing the capability for improved-feature detail for the different spectral estimators with $SNR = 40$ dB. (a) 1-D classical periodogram estimator. (b) 1-D AR Yule-Walker estimator. (c) 1-D lattice-Burg estimator. (d) the new fast 1-D covariance LS-based MV estimator. (e) the new fast 1-D modified covariance LS-based MV estimator.

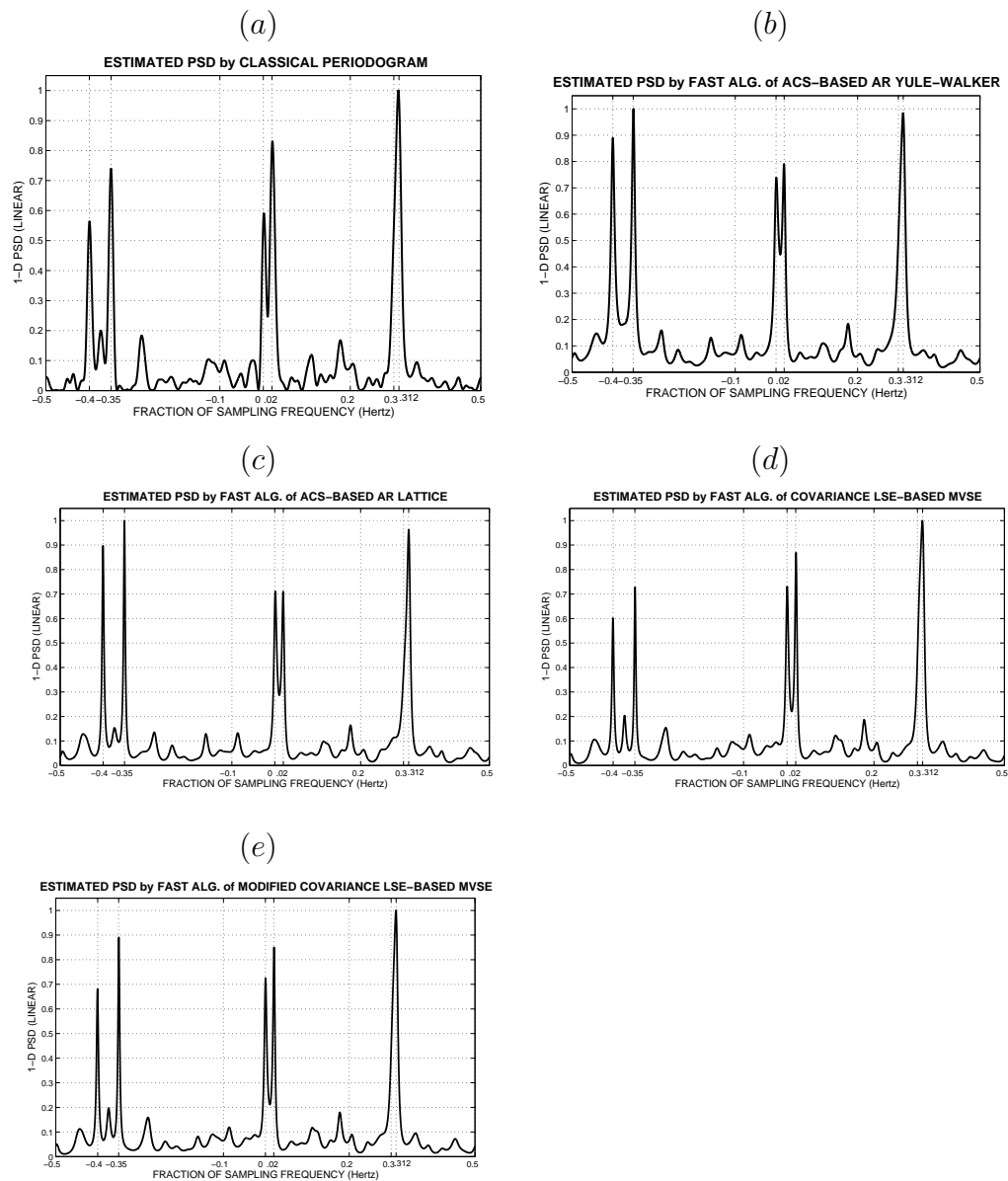


FIGURE 4.3. Comparing the capability for improved-feature detail for the different spectral estimators with $SNR = 20$ dB. (a) 1-D classical periodogram estimator. (b) 1-D AR Yule-Walker estimator. (c) 1-D lattice-Burg estimator. (d) the new fast 1-D covariance LS-based MV estimator. (e) the new fast 1-D modified covariance LS-based MV estimator.

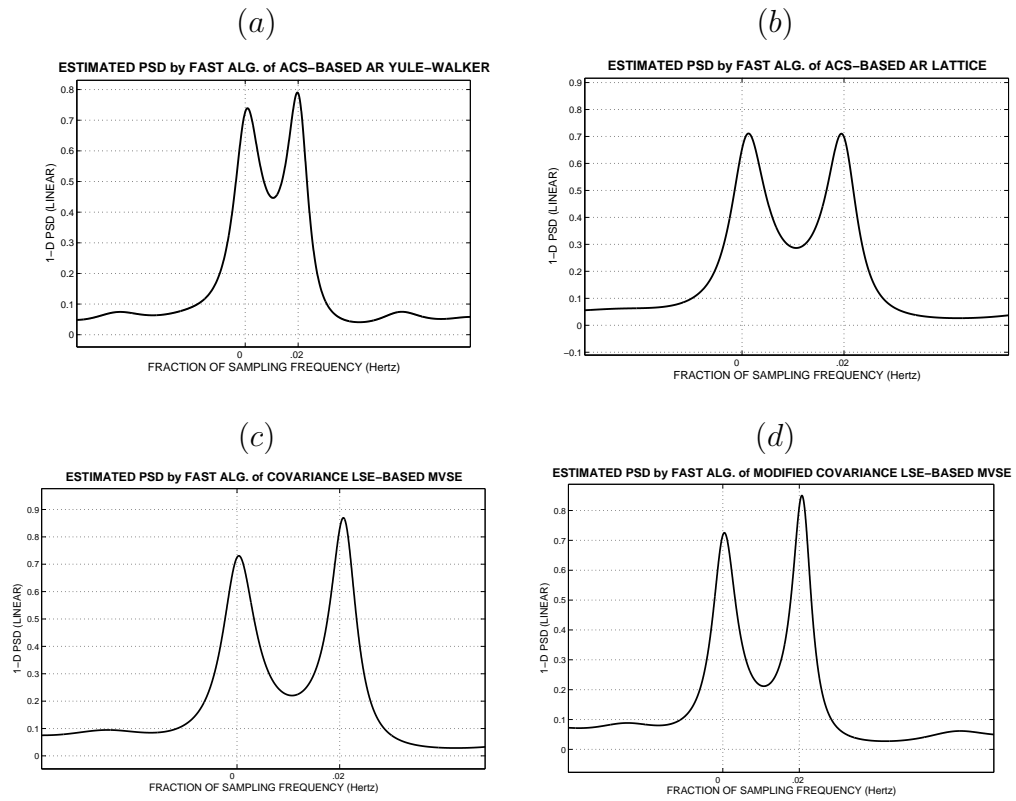


FIGURE 4.4. Close up of the peaks in different spectral estimators. (a) 1-D AR-Yule Walker estimator. (b) 1-D lattice-Burg estimator. (c) the new fast 1-D covariance LS-based MV estimator. (d) the new fast 1-D modified covariance LS-based MV estimator (zoomed in from Fig. 4.3).

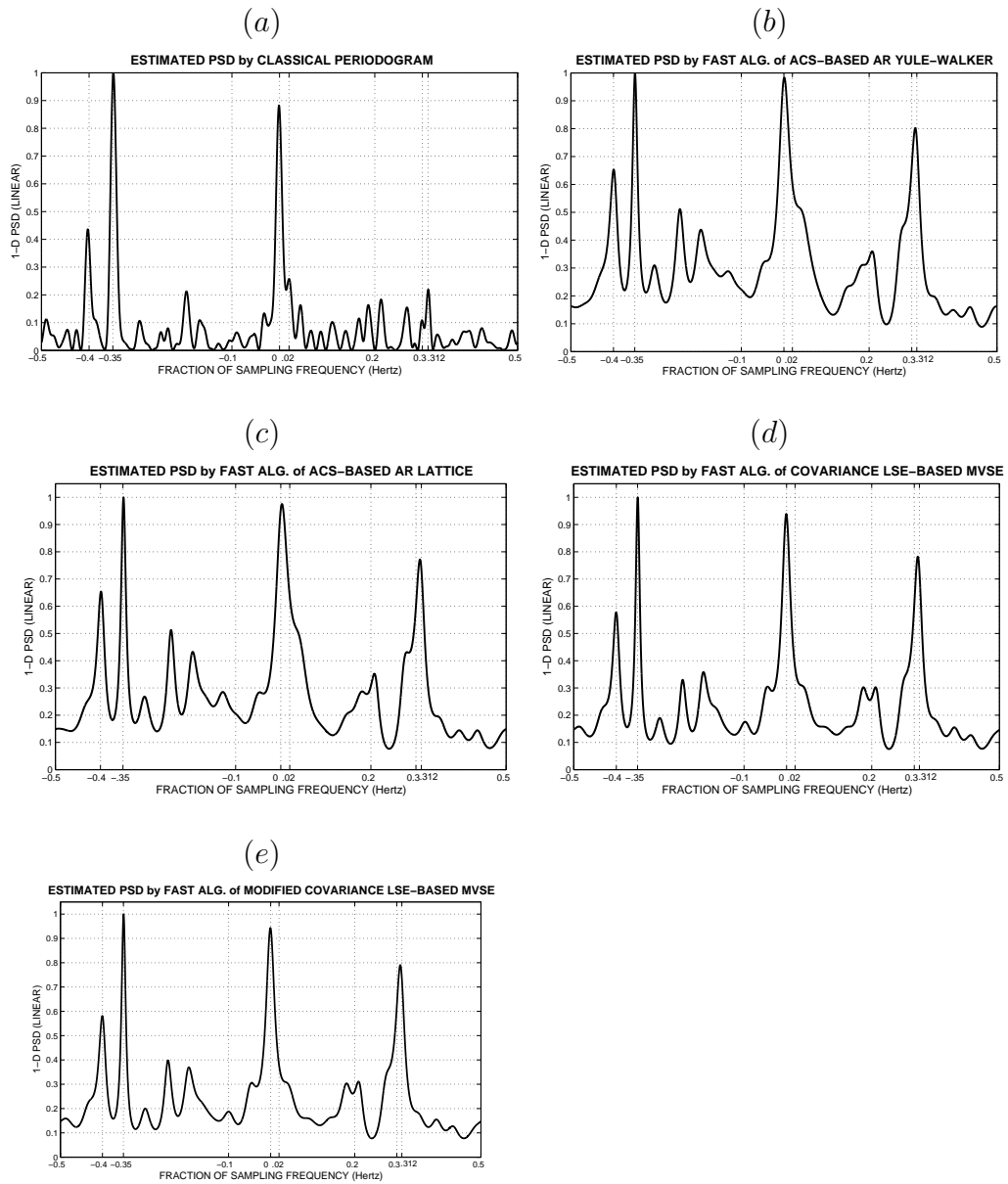


FIGURE 4.5. Comparing the capability for improved-feature detail for the different spectral estimators with $SNR = 10$ dB. (a) 1-D classical periodogram estimator. (b) 1-D AR Yule-Walker estimator. (c) 1-D lattice-Burg estimator. (d) the new fast 1-D covariance LS-based MV estimator. (e) the new fast 1-D modified covariance LS-based MV estimator.

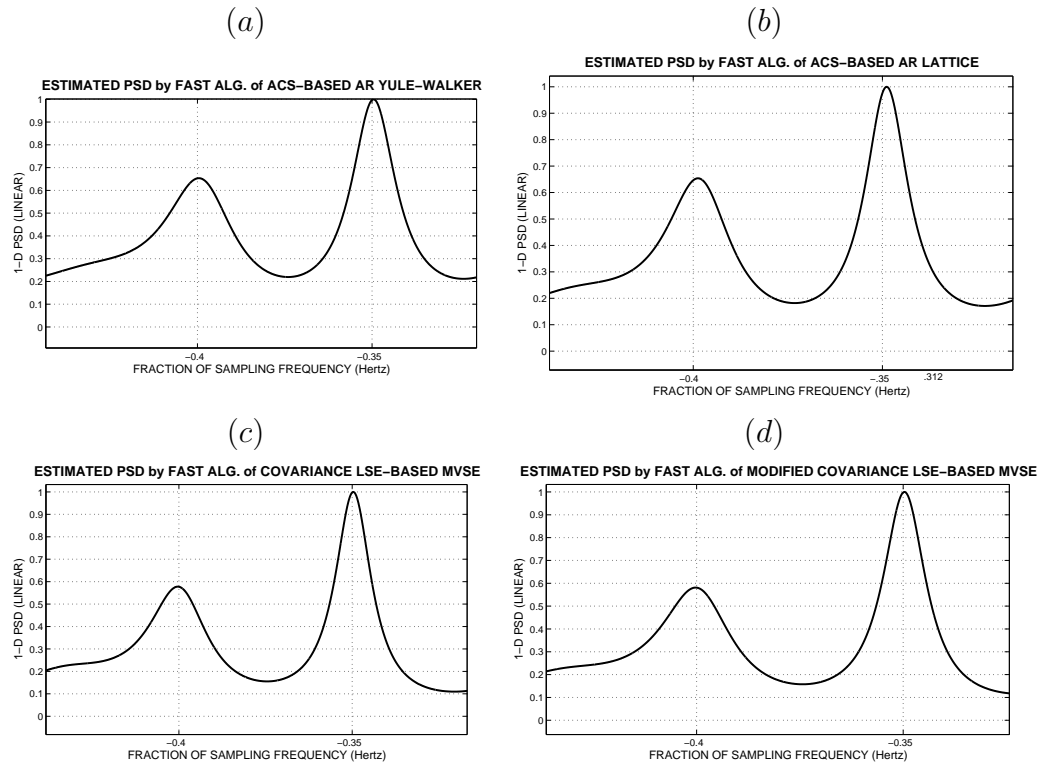


FIGURE 4.6. Close up of the biased phenomenon in different estimators. (a) 1-D AR-Yule Walker estimator. (b) 1-D lattice-Burg estimator. (c) the new fast 1-D covariance LS-based MV estimator. (d) the new fast 1-D modified covariance LS-based MV estimator (zoomed in from Fig. 4.5).

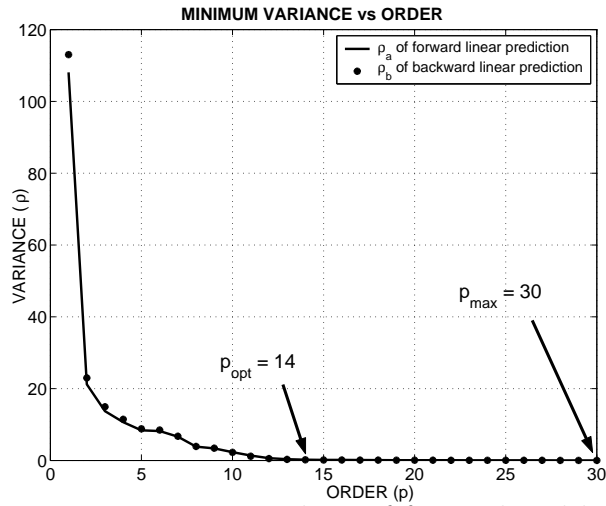


FIGURE 4.7. Output variances, ρ_a and ρ_b , of forward and backward linear prediction error decrease as order p increases.

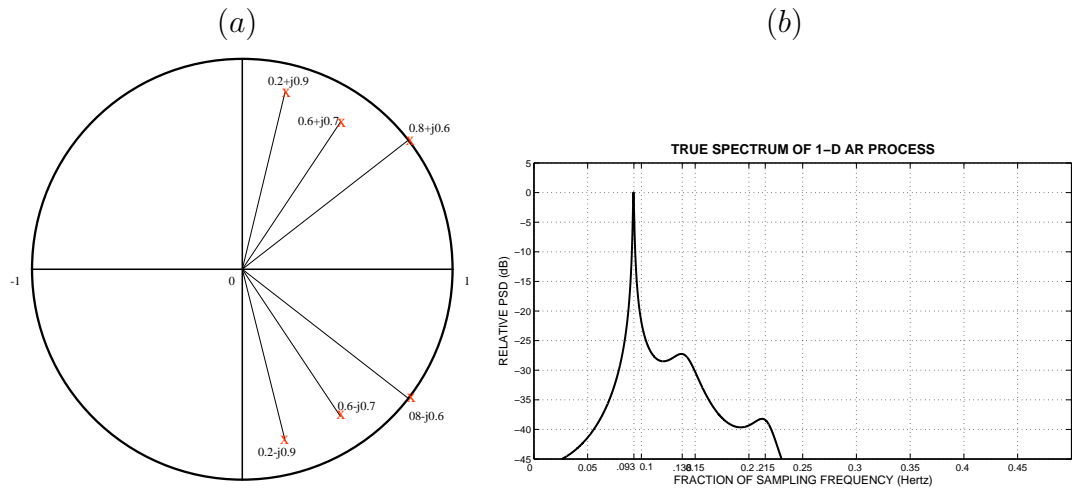


FIGURE 4.8. A six-order AR(6) process with driving noise variance $\rho_\omega = 0.01$ described by Eq. 4.4. (a) The positions of its poles. (b) True spectral density of the AR(6) process.

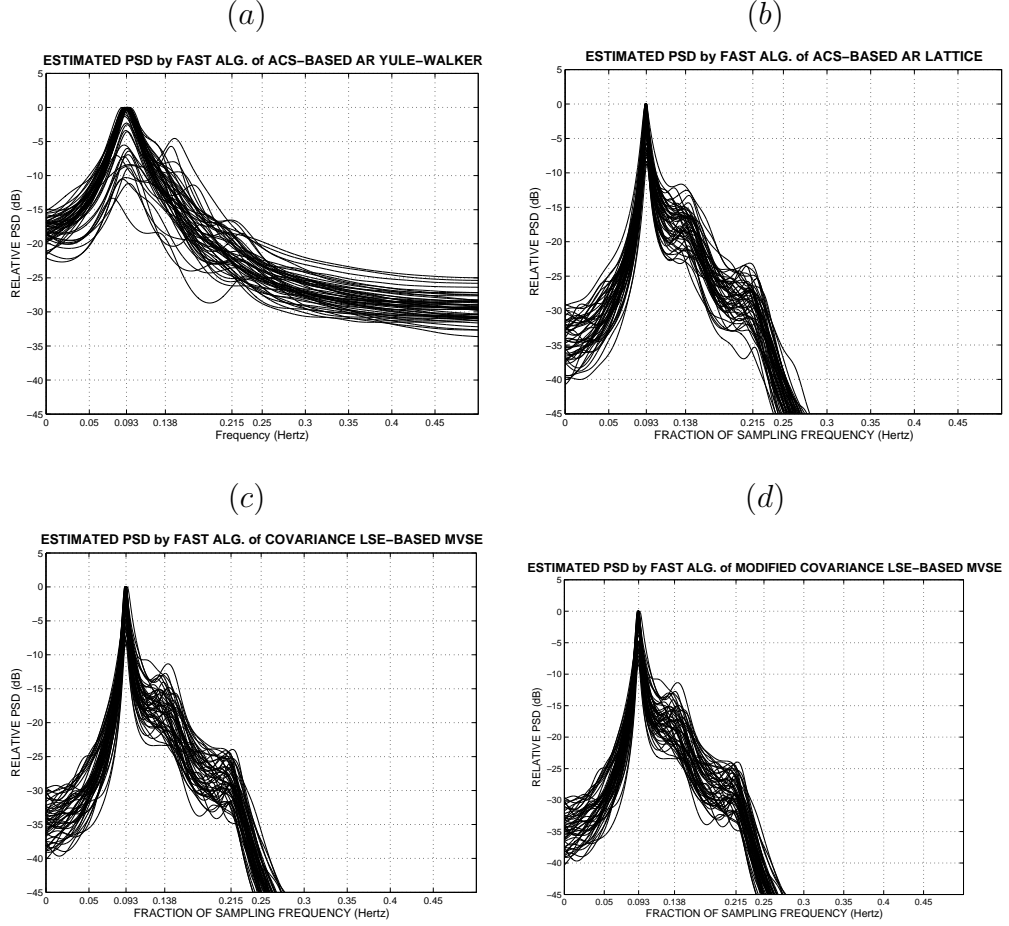


FIGURE 4.9. Response of four spectral estimators to the AR(6) process. Overlapped estimates of 50 realizations, each of 400-samples, are shown for each method. (a) 1-D AR Yule-Walker estimator. (b) 1-D lattice-Burg estimator. (c) the new fast 1-D covariance LS-based MV estimator. (d) the new fast 1-D modified covariance LS-based MV estimator.

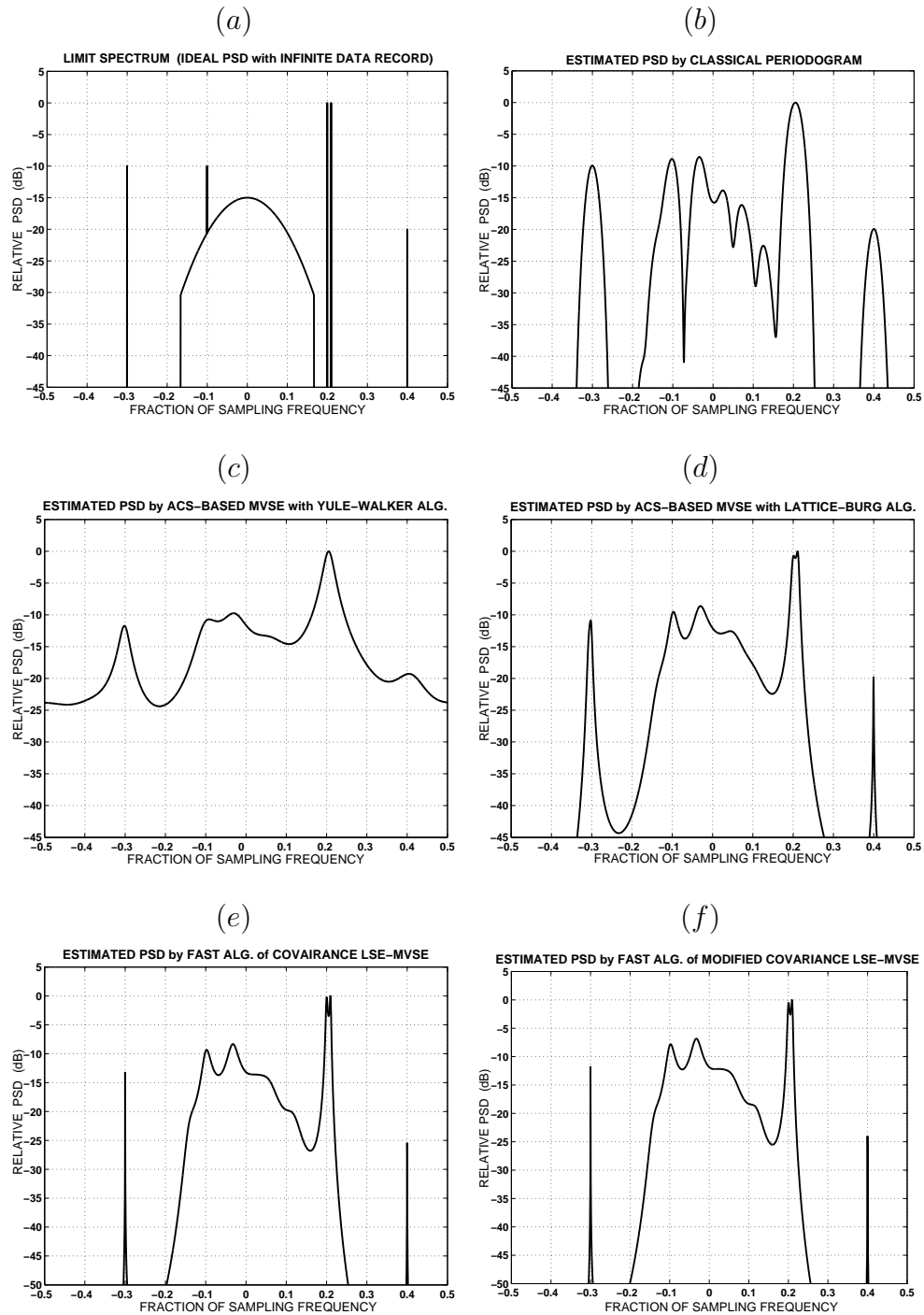


FIGURE 4.10. A set of 1-D spectral estimators of a 64-complex-point test sequence (order $p = 12$, sampling frequency $f_s = 2500$ Hz). (a) true spectra. (b) 1-D classical periodogram estimate. (c) 1-D AR Yule-Walker estimator. (d) 1-D lattice-Burg estimator. (e) the new fast 1-D covariance LS-based MV estimator. (f) the new fast 1-D modified covariance LS-based MV estimator.

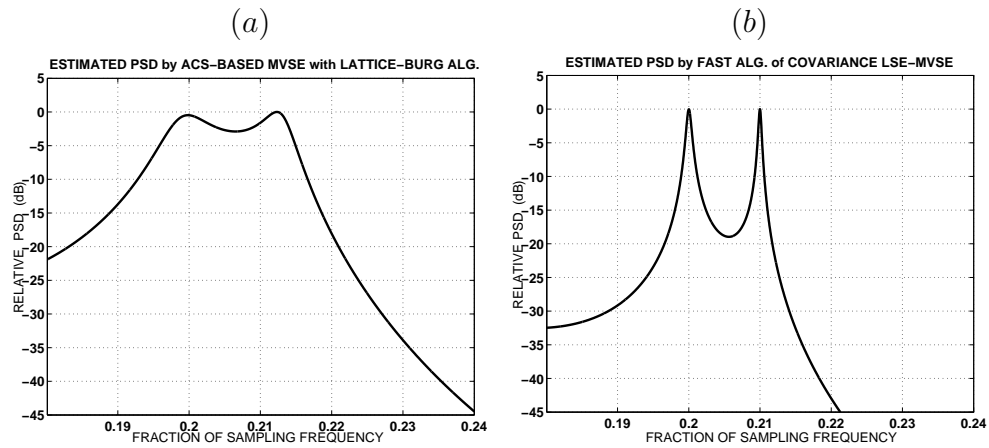


FIGURE 4.11. Close up of the biased peak phenomenon in different estimators (order $p = 12$). (a) 1-D lattice-Burg estimator. (b) the new fast 1-D covariance LS-based MV estimator (zoomed in from Fig. 4.10).

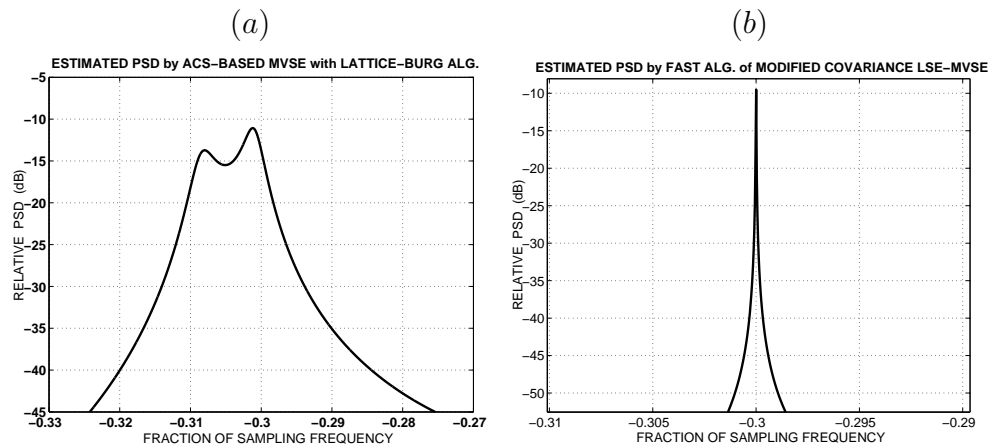


FIGURE 4.12. Close up of the line splitting phenomenon in different estimators (order $p = 16$). (a) 1-D lattice-Burg estimator. (b) the new fast 1-D modified covariance LS-based MV estimator (zoomed in from Fig. 4.10).

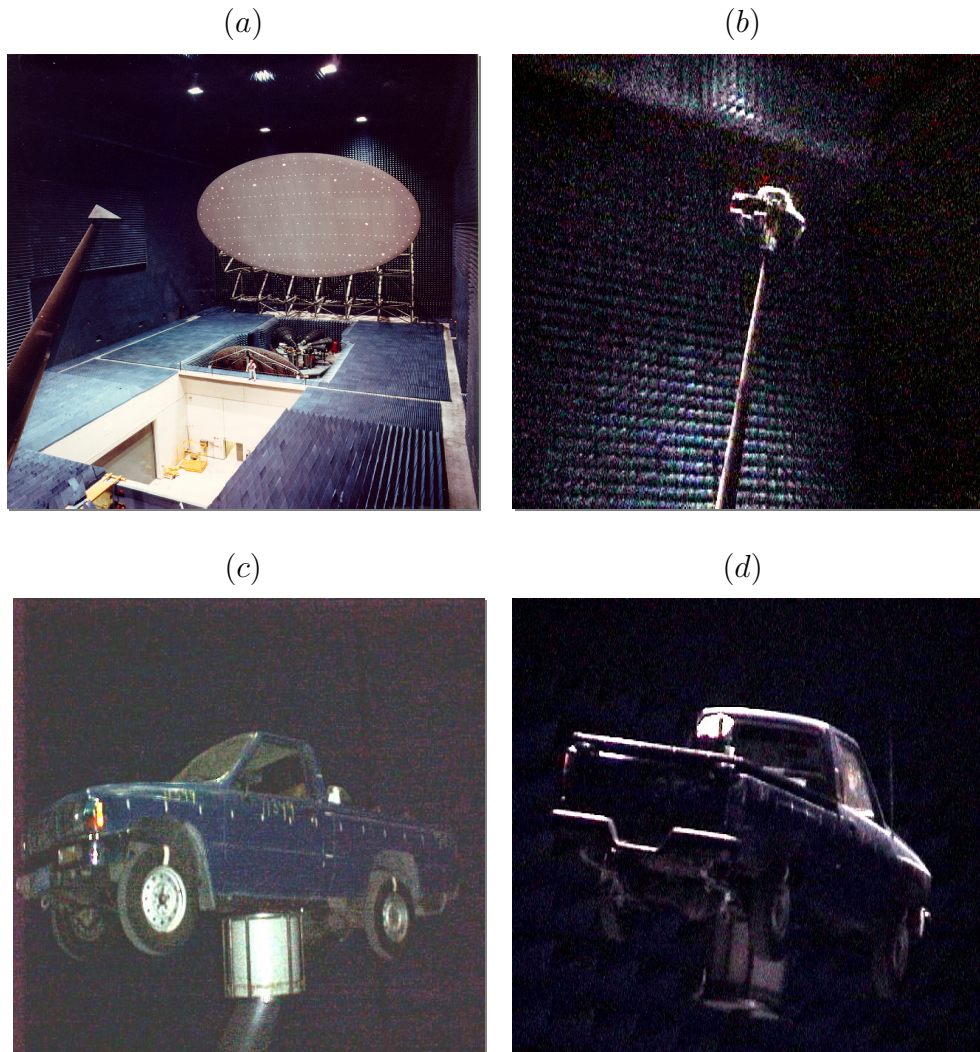


FIGURE 4.13. Photos of the acquisition system of ISAR radar data for an actual truck. (a) 10-story microwave anechoic chamber. (b) truck was set on a pylon in the middle of the chamber. (c) close up the front of truck. (d) close up the rear of the truck. (The data were collected by Dr.Marple with permission for use in this thesis.)

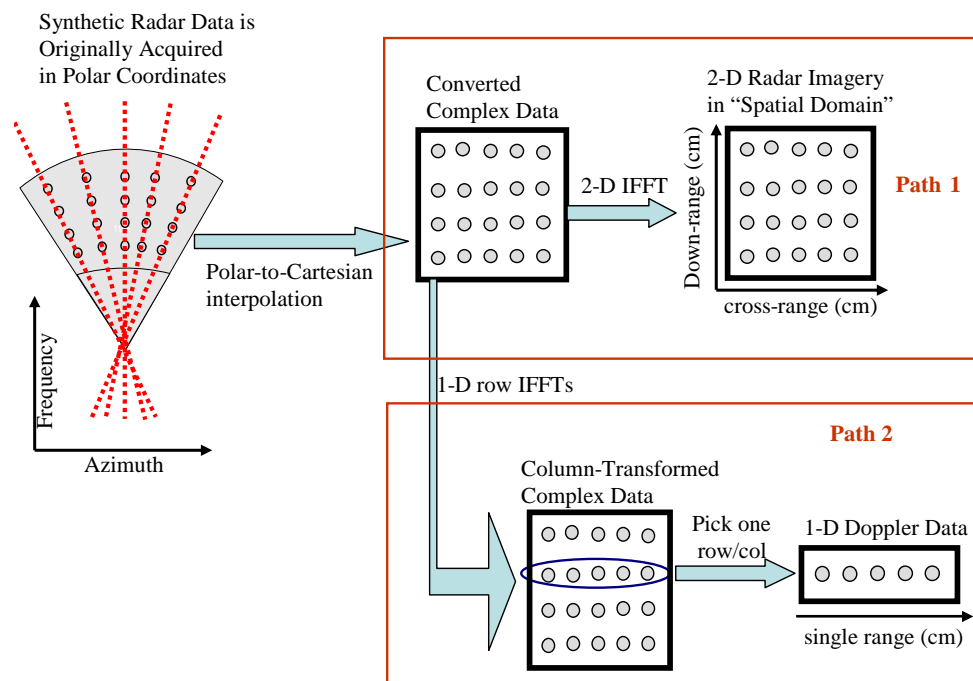


FIGURE 4.14. Illustration of basic steps to create 1-D Doppler radar data and 2-D synthetic aperture radar data that can be used to create radar imagery by 2-D spectral analysis.

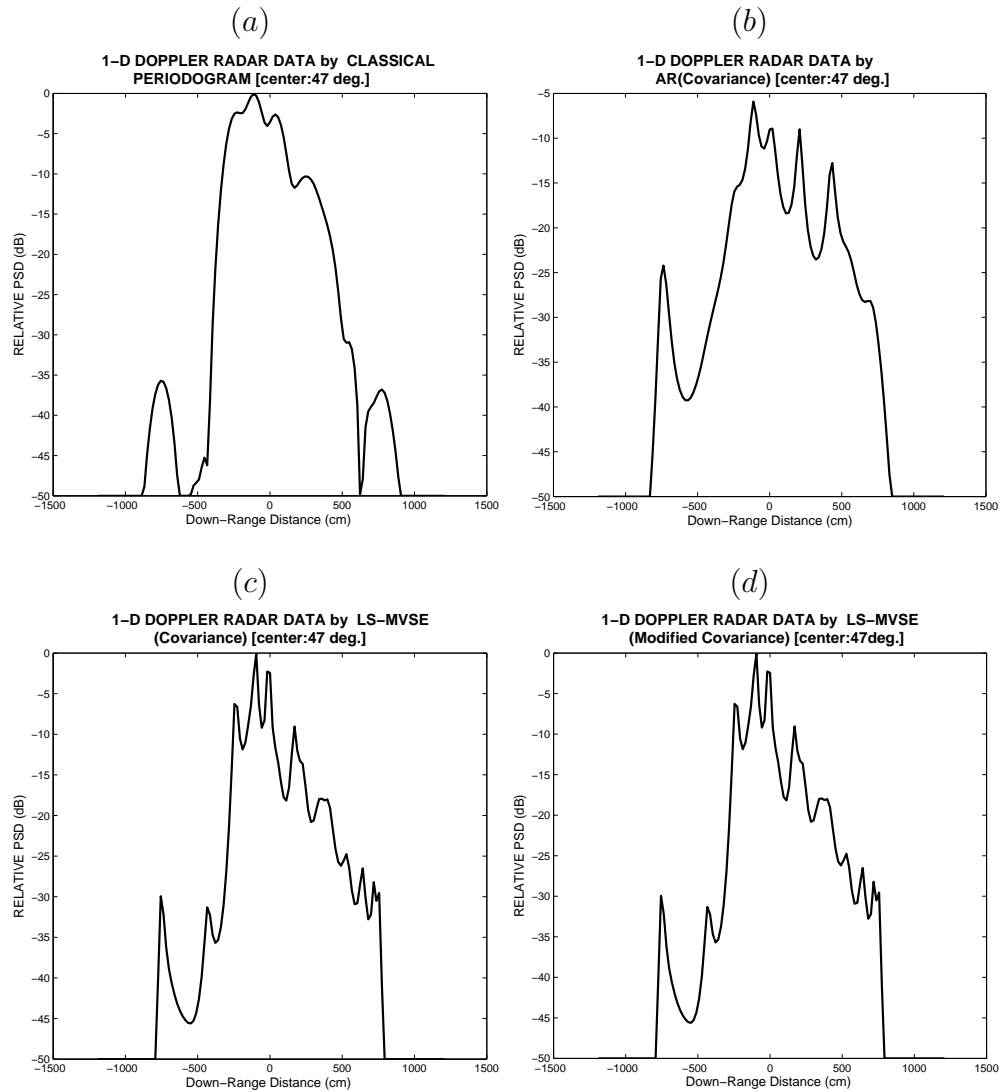


FIGURE 4.15. Truck radar echoes spectral estimates by different 1-D spectral estimators (center azimuth is 47 degrees). (a) 1-D classical periodogram estimator. (b) 1-D covariance AR estimator. (c) the new fast 1-D covariance LS-based MV estimator. (d) the new fast 1-D modified covariance LS-based MV estimator.

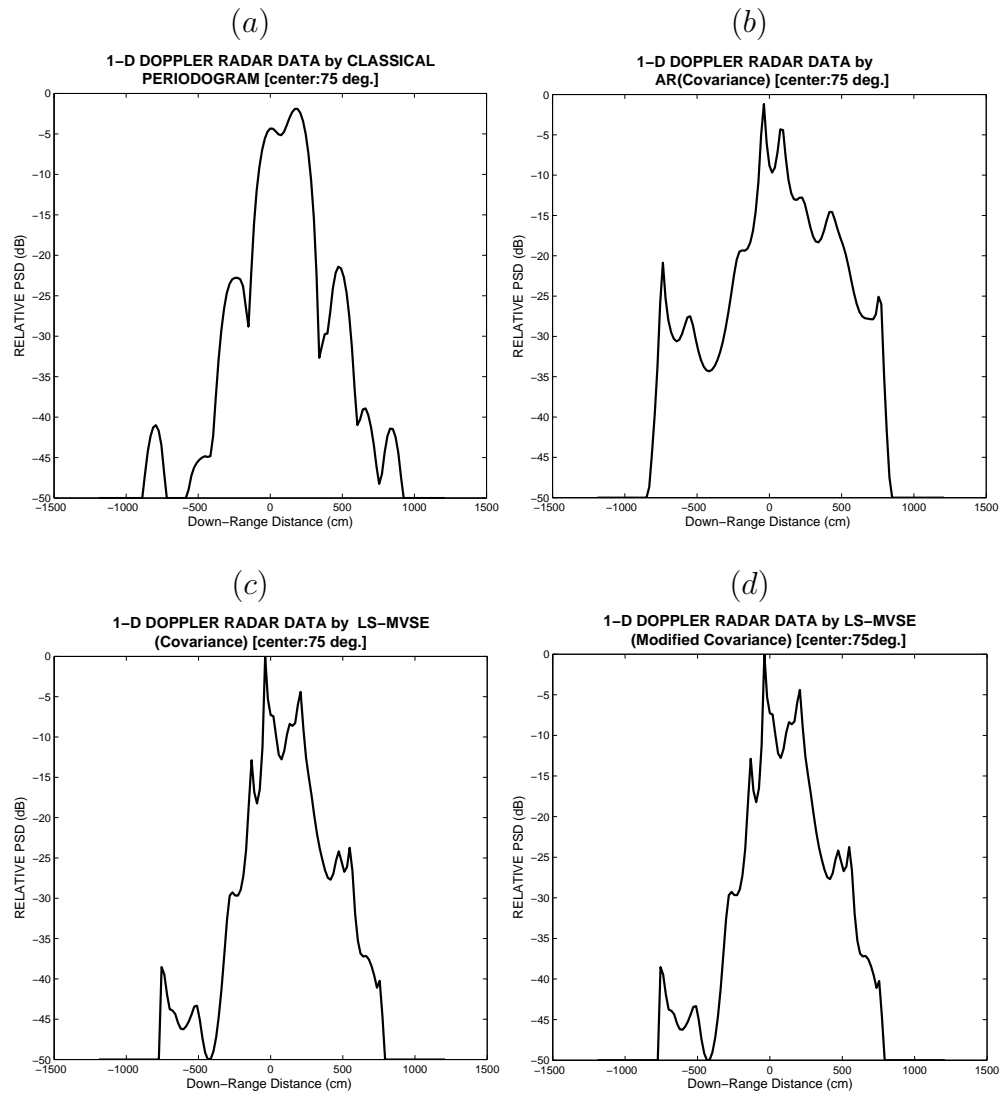


FIGURE 4.16. Truck spectral estimator by different 1-D spectral estimates (center azimuth is 75 degrees). (a) 1-D classical periodogram estimator. (b) 1-D covariance AR estimator. (c) the new fast 1-D covariance LS-based MV estimator. (d) the new fast 1-D modified covariance LS-based MV estimator.

5. TWO-DIMENSIONAL MINIMUM VARIANCE SPECTRAL ESTIMATORS: CONCEPTUAL AND ESTIMATION TECHNIQUES

5.1. Autocorrelation-Based 2-D Minimum Variance Spectral Estimation: Doubly-Toeplitz Autocorrelation Case

To develop a 2-D version of the minimum variance spectral estimator, it is convenient to consider the case of a 2-D $[p_1, p_2]$ -th order adaptive filter with parameters $h_p[k_1, k_2]$ defined over $[0 \leq k_1 \leq p_1, 0 \leq k_2 \leq p_2]$ in the first-quadrant (Q_1) plane. Assume that a 2-D discrete random process $x[n_1, n_2]$, $1 \leq n_1 \leq N_1$ and $1 \leq n_2 \leq N_2$, complex-valued (in general) and zero-mean, passes through the 2-D FIR filter. The filter output $y[n_1, n_2]$ is defined as

$$y[n_1, n_2] = \sum_{k_2=0}^{p_2} \sum_{k_1=0}^{p_1} h_p[k_1, k_2] x[n_1 - k_1, n_2 - k_2] = \mathbf{x}_p^T[n_1, n_2] \mathbf{h}_p \quad (5.1)$$

of row order p_1 and column order p_2 . Note that, for purposes of the algorithms to be described, one assumes that the row order p_1 is a fixed order while the column order p_2 is a variable order, so that the recursive order will be $p = p_2$ in Eq. 5.1. We shall also assume that $p_2 \geq p_1$ for most efficient computation, otherwise we should switch the roles of p_1 and p_2 , and let the recursive order be $p = p_1$. When either p_1 or p_2 equals zero, the 2-D adaptive filter reduces to the usual 1-D adaptive filter. In practice, we choose $p_1 < N_1$ and $p_2 < N_2$. In Eq. 5.1, the row vector of 2-D adaptive filter parameters

$$\mathbf{h}_{p_2}^T = \left(h_{p_2}[0, 0], \dots, h_{p_2}[p_1, 0], h_{p_2}[0, 1], \dots, h_{p_2}[p_1, 1], \right. \\ \left. \dots, h_{p_2}[0, p_2], \dots, h_{p_2}[p_1, p_2] \right) \quad (5.2)$$

has dimension $(p_1 + 1)(p_2 + 1) \times 1$. The column vector of 2-D data vector $\mathbf{x}_{p_2}[n_1, n_2]$ has dimension $(p_1 + 1)(p_2 + 1) \times 1$

$$\mathbf{x}_{p_2}^T[n_1, n_2] = \left(x[n_1, n_2], \dots, x[n_1 - p_1, n_2], x[n_1, n_2 - 1], \dots, x[n_1 - p_1, n_2 - 1], \right. \\ \left. \dots, x[n_1, n_2 - p_2], \dots, x[n_1 - p_1, n_2 - p_2] \right) \quad (5.3)$$

where T represents transpose. The statistical expectation of the 2-D adaptive filter output variance (which has a subscript p_2 to denote its recursive dependence on the variable dimension p_2) is

$$\rho_{p_2} = \mathcal{E}\{|y[n_1, n_2]|^2\} = \mathbf{h}_{p_2}^H \mathcal{E}\{\mathbf{x}_{p_2}^*[n_1, n_2] \mathbf{x}_{p_2}^T[n_1, n_2]\} \mathbf{h}_{p_2} = \mathbf{h}_{p_2}^H \underline{\mathbf{R}}_{p_2} \mathbf{h}_{p_2} \quad (5.4)$$

in which a bold font symbol with a bar under it, such as $\underline{\mathbf{R}}$, denotes a block matrix or a block vector. The $(p_1 + 1)(p_2 + 1) \times (p_1 + 1)(p_2 + 1)$ doubly-Toeplitz autocorrelation matrix is

$$\underline{\mathbf{R}}_{p_2} = \begin{pmatrix} r[0, 0] & \cdots & r[-p_1, 0] & r[0, -p_2] & \cdots & r[-p_1, -p_2] \\ \vdots & \ddots & \vdots & \dots & \vdots & \ddots & \vdots \\ r[p_1, 0] & \cdots & r[0, 0] & r[p_1, -p_2] & \cdots & r[0, -p_2] \\ & & \vdots & \ddots & & \vdots \\ r[0, p_2] & \cdots & r[-p_1, p_2] & r[0, 0] & \cdots & r[-p_1, 0] \\ \vdots & \ddots & \vdots & \dots & \vdots & \ddots & \vdots \\ r[p_1, p_2] & \cdots & r[0, p_2] & r[p_1, 0] & \cdots & r[0, 0] \end{pmatrix} \quad (5.5)$$

and $r[m_1, m_2] = \mathcal{E}\{x[n_1 + m_1, n_2 + m_2]x^*[n_1, n_2]\}$ are the autocorrelation sequence elements. The autocorrelation matrix $\underline{\mathbf{R}}_{p_2}$ has an alternative representation

$$\underline{\mathbf{R}}_{p_2} = \begin{pmatrix} \mathbf{R}_{p_2}[0] & \mathbf{R}_{p_2}[-1] & \cdots & \mathbf{R}_{p_2}[-p_2] \\ \mathbf{R}_{p_2}[1] & \mathbf{R}_{p_2}[0] & \cdots & \mathbf{R}_{p_2}[-(p_2 - 1)] \\ \vdots & \vdots & \ddots & \vdots \\ \mathbf{R}_{p_2}[p_2] & \mathbf{R}_{p_2}[p_2 - 1] & \cdots & \mathbf{R}_{p_2}[0] \end{pmatrix} \quad (5.6)$$

in which each block element has the structure

$$\mathbf{R}_{p_2}[i] = \begin{pmatrix} r[0, i] & r[-1, i] & \cdots & r[-p_1, i] \\ r[1, i] & r[0, i] & \cdots & r[-(p_1 - 1), i] \\ \vdots & \vdots & \ddots & \vdots \\ r[p_1, i] & r[p_1 - 1, i] & \cdots & r[0, i] \end{pmatrix} \quad (5.7)$$

for $-p_2 \leq i \leq p_2$ is a $(p_1 + 1) \times (p_1 + 1)$ Toeplitz matrix. The 2-D doubly-Toeplitz autocorrelation matrix is hermitian and centrosymmetric, that is,

$$\underline{\mathbf{R}}_{p_2} = \underline{\mathbf{R}}_{p_2}^H, \quad \underline{\mathbf{R}}_{p_2} = \underline{\mathbf{J}} \underline{\mathbf{R}}_{p_2}^* \underline{\mathbf{J}},$$

where \mathbf{J} is a $(p_1 + 1)(p_2 + 1) \times (p_1 + 1)(p_2 + 1)$ reflection matrix with the property $\mathbf{J}\mathbf{J} = \mathbf{I}$, where \mathbf{I} is an identity matrix. Although, each element matrix $\mathbf{R}_{p_2}[i]$ is not hermitian, it is Toeplitz, and it satisfies the following conjugate property

$$\mathbf{R}_{p_2}[-i] = \mathbf{R}_{p_2}^*[i].$$

The minimum variance spectral estimator of the 2-D random process is obtained by minimizing the 2-D output variance subject to the constraint that, at a selected dual frequency (f_1, f_2) , the gain is unity, that is, $\mathbf{e}_{p_2}^H(f_1, f_2) \mathbf{h}_{p_2} = 1$. The complex sinusoidal vector in Q_1 is defined as

$$\mathbf{e}_{p_2}^T(f_1, f_2) = \left(\mathbf{e}_{p_2}(f_1), \exp(j2\pi f_2 T_2) \mathbf{e}_{p_2}(f_1), \cdots, \exp(j2\pi f_2 [p_2] T_2) \mathbf{e}_{p_2}(f_1) \right) \quad (5.8)$$

with dimension $1 \times (p_2 + 1)$, in which $\mathbf{e}(f_1)$ is of dimension $1 \times (p_1 + 1)$

$$\mathbf{e}_{p_2}^T(f_1) = \left(1, \exp(j2\pi f_1 T_1), \cdots, \exp(j2\pi f_1 [p_1] T_1) \right) \quad (5.9)$$

and T_1 and T_2 are the sampling intervals. The result of the constrained minimization of the variance is

$$\rho_{2\text{DMV-acs}} = \frac{1}{\mathbf{e}_{p_2}^H(f_1, f_2) \underline{\mathbf{R}}_{p_2}^{-1} \mathbf{e}_{p_2}(f_1, f_2)} \quad (5.10)$$

Scaling the variance by $T_1 T_2$ yields units of power per Hz of bandwidth, that is, it is a 2-D power spectral density. Letting the frequencies range over $(-1/2T_1 \leq f_1 \leq 1/2T_1, -1/2T_2 \leq f_2 \leq 1/2T_2)$ in Hz or meters/cycle, we arrive at the definition of the 2D MVSE [15]

$$P_{2\text{DMV-acs}}(f_1, f_2) = T_1 T_2 \rho_{MV} = \frac{T_1 T_2}{\mathbf{e}_{p_2}^H(f_1, f_2) \mathbf{R}_{p_2}^{-1} \mathbf{e}_{p_2}(f_1, f_2)} \quad (5.11)$$

5.2. Least-Squares-Based 2-D Minimum Variance Spectral Estimation: Covariance Case

Assume that a 2-D finite data record of $N_1 \times N_2$ complex-valued (in general) samples is used to construct the 2-D adaptive FIR filter for the MVSE in Q_1 . The least-squares covariance 2-D MVSE is based on the concept of separately filtering the 2-D sampled data $x[n_1, n_2]$ over the intervals $[1 \leq n_1 \leq N_1, 1 \leq n_2 \leq N_2]$ in both a forward and a backward direction through the 2-D FIR filter of row order p_1 and column order p_2 . In anticipation of the fast computational algorithm to be proposed in the next section, we assume that the order p_1 is fixed and the order p_2 is adjustable. Normally $p_1 < N_1$ and $p_2 < N_2$. The forward filtered output y^f and the backward filtered output y^b are defined respectively as

$$\begin{aligned} y^f[n_1, n_2] &= \sum_{k_2=0}^{p_2} \sum_{k_1=0}^{p_1} \bar{h}_p^a[k_1, k_2] x[n_1 - k_1, n_2 - k_2] = \mathbf{x}_p^T[n_1, n_2] \bar{\mathbf{h}}_p^a \\ y^b[n_1, n_2] &= \sum_{k_2=0}^{p_2} \sum_{k_1=0}^{p_1} \bar{h}_p^b[k_1, k_2] x[n_1 - p_1 + k_1, n_2 - p_2 + k_2] = \mathbf{x}_p^T[n_1, n_2] \mathbf{J} \bar{\mathbf{h}}_p^b \end{aligned} \quad (5.12)$$

where $\bar{\mathbf{h}}_p^a$ and $\bar{\mathbf{h}}_p^b$ are the forward and backward 2-D FIR filter parameters, respectively. Similar to the discussion in Section 5.1, we select $p = p_2$. For most efficient computation, we shall assume $p_2 \geq p_1$. If not, the one can switch the roles of p_1 and p_2 , in which case $p = p_1$ for a variable p_1 and a fixed p_2 . The forward

parameter vector $\bar{\mathbf{h}}_{p_2}^a$ of the 2-D FIR filter is similar to the definition in Eq. 5.2, in which its alternative expression

$$(\bar{\mathbf{h}}_{p_2}^a)^T = \left((\bar{\mathbf{h}}_{p_2}^a[0])^T, (\bar{\mathbf{h}}_{p_2}^a[1])^T, \dots, (\bar{\mathbf{h}}_{p_2}^a[p_2])^T \right) \quad (5.13)$$

is a block vector of block dimension $1 \times (p_2 + 1)$. Each vector element is of dimension $1 \times (p_1 + 1)$

$$(\bar{\mathbf{h}}_{p_2}^a[k])^T = \left(\bar{h}_{p_2}^a[0, k], \bar{h}_{p_2}^a[1, k], \dots, \bar{h}_{p_2}^a[p_1, k] \right) \quad (5.14)$$

for $0 \leq k \leq p_2$. The definition of the data vector $\mathbf{x}_{p_2}[n_1, n_2]$ of dimension $(p_1 + 1)(p_2 + 1) \times 1$ was defined previously in Eq. 5.3. The backward parameter vector

$$(\bar{\mathbf{h}}_{p_2}^b)^T = \left((\bar{\mathbf{h}}_{p_2}^b[0])^T, (\bar{\mathbf{h}}_{p_2}^b[1])^T, \dots, (\bar{\mathbf{h}}_{p_2}^b[p_2])^T \right) \quad (5.15)$$

is of dimension $1 \times (p_2 + 1)$ with vector elements each of dimension $1 \times (p_1 + 1)$

$$(\bar{\mathbf{h}}_{p_2}^b[k])^T = \left(\bar{h}_{p_2}^b[0, k], \bar{h}_{p_2}^b[1, k], \dots, \bar{h}_{p_2}^b[p_1, k] \right) \quad (5.16)$$

for $0 \leq k \leq p_2$. Thus, Eq. 5.12 could be reformulated as

$$y^f[n_1, n_2] = \mathbf{x}_{p_2}^T[n_1, n_2] \bar{\mathbf{h}}_{p_2}^a \quad (5.17)$$

$$y^b[n_1, n_2] = \mathbf{x}_{p_2}^T[n_1, n_2] \mathbf{J} \bar{\mathbf{h}}_{p_2}^b.$$

To solve the 2-D least squares normal equations of the 2-D covariance interval window of linear prediction, we shall assume that 2-D data is only available over a 2-D range of $1 \leq n_1 \leq N_1, 1 \leq n_2 \leq N_2$, so that valid 2-D FIR outputs for Q_1 can only be formed over the intervals $p_1 + 1 \leq n_1 \leq N_1$ and $p_2 + 1 \leq n_2 \leq N_2$ without running off the ends of the data. The statistical expectation of the forward filter output variance may then be estimated as, if normalized by $1/[(N_1 - p_1)(N_2 - p_2)]$,

$$\begin{aligned}
\hat{\rho}_{p_2} &= \frac{1}{(N_1 - p_1)(N_2 - p_2)} \sum_{n_2=p_2+1}^{N_2} \sum_{n_1=p_1+1}^{N_1} |y^f[n_1, n_2]|^2 \\
&= \frac{1}{(N_1 - p_1)(N_2 - p_2)} (\bar{\mathbf{h}}_{p_2}^a)^H \left(\sum_{n_2=p_2+1}^{N_2} \sum_{n_1=p_1+1}^{N_1} \mathbf{x}_{p_2}^*[n_1, n_2] \mathbf{x}_{p_2}^T[n_1, n_2] \right) \bar{\mathbf{h}}_{p_2}^a \\
&= \frac{1}{(N_1 - p_1)(N_2 - p_2)} (\bar{\mathbf{h}}_{p_2}^a)^H (\mathbf{X}_{p_2}^H \mathbf{X}_{p_2}) \bar{\mathbf{h}}_{p_2}^a
\end{aligned} \tag{5.18}$$

in which the $(N_2 - p_2) \times (p_2 + 1)$ rectangular block Toeplitz data matrix

$$\mathbf{X}_{p_2} = \begin{pmatrix} \mathbf{x}[p_2 + 1] & \mathbf{x}[p_2] & \cdots & \mathbf{x}[1] \\ \mathbf{x}[p_2 + 2] & \mathbf{x}[p_2 + 1] & \cdots & \mathbf{x}[2] \\ \vdots & \vdots & \ddots & \vdots \\ \mathbf{x}[N_2] & \mathbf{x}[N_2 - 1] & \cdots & \mathbf{x}[N_2 - p_2] \end{pmatrix} \tag{5.19}$$

also has elements

$$\mathbf{x}[k] = \begin{pmatrix} x[p_1 + 1, k] & x[p_1, k] & \cdots & x[1, k] \\ x[p_1 + 2, k] & x[p_1 + 1, k] & \cdots & x[2, k] \\ \vdots & \vdots & \ddots & \vdots \\ x[N_1, k] & x[N_2 - 1, k] & \cdots & x[N_1 - p_1, k] \end{pmatrix} \tag{5.20}$$

which themselves form rectangular Toeplitz 2-D data matrices of dimension $(N_1 - p_1) \times (p_1 + 1)$ over $1 \leq k \leq N_2$.

We minimize the estimated filter output variance $\hat{\rho}_{p_2}$ subject to the same unit gain constraint as applied to the 2-D ACS-based MVSE, at a 2-D frequency (f_{0_1}, f_{0_2}) , that is $\mathbf{e}_{p_2}^H(f_{0_1}, f_{0_2}) \bar{\mathbf{h}}_{p_2}^a = 1$, and then scale the minimized variance $\hat{\rho}_{2DMV}$ by $T_1 T_2$ to yield the following 2-D PSD. Letting the 2-D frequency range over $(-1/2T_1 \leq f_1 \leq 1/2T_1, -1/2T_2 \leq f_2 \leq 1/2T_2)$ in Hz or meters/cycle, the 2-D covariance LS-based MVSE has the formulation

$$\hat{P}_{2DMV-\text{cov}}(f_1, f_2) = T_1 T_2 \hat{\rho}_{p_2} = \frac{T_1 T_2}{\mathbf{e}_{p_2}^H(f_1, f_2) \hat{\mathbf{R}}_{p_2}^{-1} \mathbf{e}_{p_2}(f_1, f_2)} \tag{5.21}$$

in which the complex sinusoidal vector $\mathbf{e}(f_1, f_2)$ for Q_1 is defined in Eq. 5.8 and Eq. 5.9, and the product of the block data matrices Eq. 5.19 is

$$\hat{\mathbf{R}}_{p_2} = \mathbf{X}_{p_2}^H \mathbf{X}_{p_2} = \begin{pmatrix} \hat{\mathbf{R}}_{p_2}[0, 0] & \hat{\mathbf{R}}_{p_2}[0, 1] & \cdots & \hat{\mathbf{R}}_{p_2}[0, p_2] \\ \hat{\mathbf{R}}_{p_2}[1, 0] & \hat{\mathbf{R}}_{p_2}[1, 1] & \cdots & \hat{\mathbf{R}}_{p_2}[1, p_2] \\ \vdots & \vdots & \ddots & \vdots \\ \hat{\mathbf{R}}_{p_2}[p_2, 0] & \hat{\mathbf{R}}_{p_2}[p_2, 1] & \cdots & \hat{\mathbf{R}}_{p_2}[p_2, p_2] \end{pmatrix} \quad (5.22)$$

of dimension $(p_1 + 1)(p_2 + 1) \times (p_1 + 1)(p_2 + 1)$, and $\hat{\mathbf{R}}_{p_2}[i, j]$ for $0 \leq i, j \leq p_2$ is defined as

$$\hat{\mathbf{R}}_{p_2}[i, j] = \sum_{m=p_2+1}^{N_2} \mathbf{x}^H[m - i] \mathbf{x}[m - j] \quad (5.23)$$

which forms a $(p_1 + 1) \times (p_1 + 1)$ square matrix

$$\hat{\mathbf{R}}_{p_2}[i, j] = \begin{pmatrix} \hat{r}_{p_2}[0, j - i] & \hat{r}_{p_2}[1, j - i] & \cdots & \hat{r}_{p_2}[p_1, j - i] \\ \hat{r}_{p_2}[-1, j - i] & \hat{r}_{p_2}[0, j - i] & \cdots & \hat{r}_{p_2}[p_1 - 1, j - i] \\ \vdots & \vdots & \ddots & \vdots \\ \hat{r}_{p_2}[-p_1, j - i] & \hat{r}_{p_2}[-(p_1 - 1), j - i] & \cdots & \hat{r}_{p_2}[0, j - i] \end{pmatrix} \quad (5.24)$$

where $\hat{r}_{p_2}[i, j] = \sum_{k=p_1+1}^{N_1} x^H[k, m - i] x[k - l, m - j]$, for $-p_1 \leq l \leq p_1$, is an element of $\hat{\mathbf{R}}_{p_2}[i, j]$. $\hat{\mathbf{R}}_{p_2}$ is a LS-based stochastic approximation of the $(p_1 + 1)(p_2 + 1) \times (p_1 + 1)(p_2 + 1)$ autocorrelation matrix \mathbf{R}_{p_2} in the known autocorrelation case; it does not have the doubly Toeplitz structure of the known autocorrelation case, but it does have a *near-to-doubly-Toeplitz* structure which will be exploited to develop a computationally efficient algorithm for the solution of the 2-D covariance LS-based MVSE, which will be presented in Section 6.2.1. If either p_1 or p_2 is equal to zero, the 2-D linear prediction then reduces to the 1-D usual linear prediction solution, in which case the 2-D covariance LS-based MVSE in Eq. 5.21 will yield numerical results identical to the 1-D covariance LS-based MVSE solution [30].

One can define the 2-D covariance LS-MVSE in Eq. 5.21 for the three other quarter planes Q_2 , Q_3 and Q_4 in a similar manner. Analogous to Eq. 5.8 and Eq. 5.9, the complex sinusoidal vectors \mathbf{e}^i , ($i = 2, 3, 4$) for Q_2 to Q_4 are defined as

$$(\mathbf{e}_{p_2}^2(f_1, f_2))^T = \left(\exp(-j2\pi f_2 [p_2] T_2) \mathbf{e}_{p_2}^2(f_1), \exp(-j2\pi f_2 [p_2 - 1] T_2) \mathbf{e}_{p_2}^2(f_1), \dots, \right. \\ \left. \exp(-j2\pi f_2 T_2) \mathbf{e}_{p_2}^2(f_1), \mathbf{e}_{p_2}^2(f_1) \right)$$

$$(\mathbf{e}_{p_2}^2(f_1))^T = \left(1, \exp(j2\pi f_1 T_1), \dots, \exp(j2\pi f_1 [p_1] T_1) \right),$$

and

$$(\mathbf{e}_{p_2}^3(f_1, f_2))^T = \left(\exp(-j2\pi f_2 [p_2] T_2) \mathbf{e}_{p_2}^3(f_1), \exp(-j2\pi f_2 [p_2 - 1] T_2) \mathbf{e}_{p_2}^3(f_1), \dots \right. \\ \left. \exp(-j2\pi f_2 T_2) \mathbf{e}_{p_2}^3(f_1), \mathbf{e}_{p_2}^3(f_1) \right)^T$$

$$(\mathbf{e}_{p_2}^3(f_1))^T = \left(\exp(-j2\pi f_1 [p_1] T_1), \exp(-j2\pi f_1 [p_1 - 1] T_1), \dots, 1 \right),$$

and

$$(\mathbf{e}_{p_2}^4(f_1, f_2))^T = \left(\mathbf{e}_{p_2}^4(f_1), \exp(j2\pi f_2 T_2) \mathbf{e}_{p_2}^4(f_1), \dots, \exp(j2\pi f_2 [p_2 - 1] T_2) \mathbf{e}_{p_2}^4(f_1), \right. \\ \left. \exp(j2\pi f_2 [p_2] T_2) \mathbf{e}_{p_2}^4(f_1) \right)^T$$

$$(\mathbf{e}_{p_2}^4(f_1))^T = \left(\exp(-j2\pi f_1 [p_1] T_1), \exp(-j2\pi f_1 [p_1 - 1] T_1), \dots, 1 \right).$$

Substituting $\mathbf{e}_{p_2}^i$ ($i = 2, 3, 4$) into Eq. 5.21 yields the 2-D covariance LS-based MVSE formulation for the second, third and fourth quadrants (Q_2 , Q_3 and Q_4). Each formulation in Q_2 , Q_3 and Q_4 achieves identically numerical results of the 2-D covariance LS-based MVSE formulated in Eq. 5.21 for Q_1 . Although MVSE is a nonparametric spectral estimation, it is developed starting from an adaptive 2-D filter with 2-D AR parameters. However, the adaptive parameters disappear in the

final PSD expression in Eq. 5.21; that expression only depends on the inverse data product matrix $\hat{\mathbf{R}}_{p_2}^{-1}$, independent of the quadrant selected. Therefore, it is not necessary to calculate the 2-D covariance LS-based MVSE for all four quadrants. This is in contrast to the 2-D AR estimator, in which each 2-D AR quadrant estimates skews the spectral estimate in different directions.

5.3. Least-Squares-Based 2-D Minimum Variance Spectral Estimation: Modified Covariance Case

The 2-D modified covariance LS-based MVSE was developed in the same manner as 1-D modified covariance LS-based MVSE. The 2-D modified covariance LS-based MVSE is a combination of filtering the signal process $x[n_1, n_2]$ over the intervals $[1 \leq n_1 \leq N_1, 1 \leq n_2 \leq N_2]$ in both forward and backward directions through the 2-D FIR filter in one variance expression. The forward filtered output y^f and the backward filtered output y^b are defined respectively as

$$\begin{aligned} y^f[n_1, n_2] &= \sum_{k_2=0}^{p_2} \sum_{k_1=0}^{p_1} \tilde{h}_p^a[k_1, k_2] x[n_1 - k_1, n_2 - k_2] = \mathbf{x}_p^T[n_1, n_2] \tilde{\mathbf{h}}_p^a \\ y^b[n_1, n_2] &= \sum_{k_2=0}^{p_2} \sum_{k_1=0}^{p_1} \tilde{h}_p^{a*}[k_1, k_2] x[n_1 - p_1 + k_1, n_2 - p_2 + k_2] \\ &= \mathbf{x}_p^T[n_1, n_2] \mathbf{J} \tilde{\mathbf{h}}_p^{a*} \end{aligned} \quad (5.25)$$

where $\tilde{\mathbf{h}}_p^a$ is forward 2-D FIR filter parameters. Similar to the discussion in Section 5.1, one selects $p = p_2$ and assumes that $p_2 \geq p_1$ and $p_1 < N_1, p_2 < N_2$. The alternative expression of the forward parameter vector is defined as

$$(\tilde{\mathbf{h}}_{p_2}^a)^T = \left((\tilde{\mathbf{h}}_{p_2}^a[0])^T, (\tilde{\mathbf{h}}_{p_2}^a[1])^T, \dots, (\tilde{\mathbf{h}}_{p_2}^a[p_2])^T \right) \quad (5.26)$$

which is a block vector of block dimension $(p_2 + 1) \times 1$ with vector elements, each of which has dimension $(p_1 + 1) \times 1$

$$(\tilde{\mathbf{h}}_{p_2}^a[k])^T = \left(\tilde{h}_{p_2}^a[0, k], \tilde{h}_{p_2}^a[1, k], \dots, \tilde{h}_{p_2}^a[p_1, k] \right) \quad (5.27)$$

for $0 \leq k \leq p_2$. The definition of the data vector $\mathbf{x}_{p_2}[n_1, n_2]$ of dimension $(p_1 + 1)(p_2 + 1) \times 1$ was defined in Eq. 5.3. Eq. 5.25 can be reformulated as

$$\begin{aligned} y^f[n_1, n_2] &= \mathbf{x}_{p_2}^T[n_1, n_2] \tilde{\mathbf{h}}_{p_2}^a \\ y^b[n_1, n_2] &= \mathbf{x}_{p_2}^T[n_1, n_2] \mathbf{J} \tilde{\mathbf{h}}_{p_2}^{a*} . \end{aligned} \quad (5.28)$$

To solve the 2-D least squares normal equations of the 2-D covariance interval window of LP, we shall assume that 2-D data is only available over the 2-D range $(1 \leq n_1 \leq N_1, 1 \leq n_2 \leq N_2)$, so that valid 2-D FIR outputs for Q_1 can only be formed over the intervals $p_1 + 1 \leq n_1 \leq N_1$ and $p_2 + 1 \leq n_2 \leq N_2$ without running off the ends of the data. The statistical expectation of the forward filter output variance may then be estimated as, if normalized by $1/[(N_1 - p_1)(N_2 - p_2)]$,

$$\begin{aligned} \hat{\rho}_{p_2} &= \frac{1}{(N_1 - p_1)(N_2 - p_2)} \sum_{n_2=p_2+1}^{N_2} \sum_{n_1=p_1+1}^{N_1} |y^f[n_1, n_2]|^2 \\ &= \frac{1}{(N_1 - p_1)(N_2 - p_2)} (\tilde{\mathbf{h}}_{p_2}^a)^H \left(\sum_{n_2=p_2+1}^{N_2} \sum_{n_1=p_1+1}^{N_1} \mathbf{x}_{p_2}^*[n_1, n_2] \mathbf{x}_{p_2}^T[n_1, n_2] \right. \\ &\quad \left. + \mathbf{J} \mathbf{x}_{p_2}[n_1, n_2] \mathbf{x}_{p_2}^H[n_1, n_2] \mathbf{J} \right) \tilde{\mathbf{h}}_{p_2}^a \\ &= \frac{1}{(N_1 - p_1)(N_2 - p_2)} (\tilde{\mathbf{h}}_{p_2}^a)^H (\mathbf{X}_{p_2}^H \mathbf{X}_{p_2} + \mathbf{J} \mathbf{X}_{p_2}^T \mathbf{X}_{p_2}^* \mathbf{J}) \tilde{\mathbf{h}}_{p_2}^a \end{aligned} \quad (5.29)$$

in which the $(N_2 - p_2) \times (p_2 + 1)$ rectangular block Toeplitz data matrix \mathbf{X}_{p_2} is defined in Eq. 5.19 .

The estimated filter output variance $\hat{\rho}_{p_2}$ is minimized, subject to the same unit gain constraint at a 2-D frequency (f_{0_1}, f_{0_2}) as applied to the 2-D ACS-based

MVSE, that is $\mathbf{e}_{p_2}^H(f_{0_1}, f_{0_2}) (\tilde{\mathbf{h}}_{p_2}^a) = 1$. Scaling the minimized variance $\hat{\rho}_{p_2}$ by $T_1 T_2$ then yields the following 2-D PSD. Letting the 2-D frequency range over $(-1/2T_1 \leq f_1 \leq 1/2T_1, -1/2T_2 \leq f_2 \leq 1/2T_2)$ in Hz or meters/cycle, the 2-D modified covariance LS-based MVSE has the formulation

$$\hat{P}_{2\text{DMV-mod}}(f_1, f_2) = T_1 T_2 \hat{\rho}_{2\text{DMV}} = \frac{T_1 T_2}{\mathbf{e}_{p_2}^H(f_1, f_2) \hat{\mathbf{R}}_{p_2}^{-1} \mathbf{e}_{p_2}(f_1, f_2)} \quad (5.30)$$

in which the complex sinusoidal vector $\mathbf{e}(f_1, f_2)$ for Q_1 is defined in Eq. 5.8 and Eq. 5.9, and the product of the block data matrices forms the $\hat{\mathbf{R}}_{p_2}$ matrix as

$$\hat{\mathbf{R}}_{p_2} = \mathbf{X}_{p_2}^H \mathbf{X}_{p_2} + \mathbf{J} \mathbf{X}_p^T \mathbf{X}_p^* \mathbf{J} = \begin{pmatrix} \hat{\mathbf{R}}_{p_2}[0, 0] & \hat{\mathbf{R}}_{p_2}[0, 1] & \cdots & \hat{\mathbf{R}}_{p_2}[0, p_2] \\ \hat{\mathbf{R}}_{p_2}[1, 0] & \hat{\mathbf{R}}_{p_2}[1, 1] & \cdots & \hat{\mathbf{R}}_{p_2}[1, p_2] \\ \vdots & \vdots & \ddots & \vdots \\ \hat{\mathbf{R}}_{p_2}[p_2, 0] & \hat{\mathbf{R}}_{p_2}[p_2, 1] & \cdots & \hat{\mathbf{R}}_{p_2}[p_2, p_2] \end{pmatrix} \quad (5.31)$$

which has dimension $(p_1 + 1)(p_2 + 1) \times (p_1 + 1)(p_2 + 1)$, and the block elements $\hat{\mathbf{R}}_{p_2}[i, j]$ for $0 \leq i, j \leq p_2$ are defined as

$$\begin{aligned} \hat{\mathbf{R}}_{p_2}[i, j] = \sum_{m=p_2+1}^{N_2} & \left(\mathbf{x}^H[m - i] \mathbf{x}[m - j] \right. \\ & \left. + \mathbf{J} \mathbf{x}^T[m - (p_2 + 1) + i] \mathbf{x}^*[m - (p_2 + 1) + j] \mathbf{J} \right) \end{aligned} \quad (5.32)$$

which forms a $(p_1 + 1) \times (p_1 + 1)$ square matrix

$$\hat{\mathbf{R}}_{p_2}[i, j] = \begin{pmatrix} \hat{r}_{p_2}[0, j - i] & \hat{r}_{p_2}[1, j - i] & \cdots & \hat{r}_{p_2}[p_1, j - i] \\ \hat{r}_{p_2}[-1, j - i] & \hat{r}_{p_2}[0, j - i] & \cdots & \hat{r}_{p_2}[p_1 - 1, j - i] \\ \vdots & \vdots & \ddots & \vdots \\ \hat{r}_{p_2}[-p_1, j - i] & \hat{r}_{p_2}[-(p_1 - 1), j - i] & \cdots & \hat{r}_{p_2}[0, j - i] \end{pmatrix} \quad (5.33)$$

where each element

$$\begin{aligned} \hat{r}_{p_2}[l, j - i] = \sum_{k=p_1+1}^{N_1} & \left(x^*[k, m - i] x[k - l, m - j] \right. \\ & \left. + x[k, m - (p_1 + 1) + i] x^*[k - l, m - (p_1 + 1) + j] \right), \end{aligned}$$

for $-p_1 \leq l \leq p_1$. Note that $\hat{\underline{\mathbf{R}}}_{p_2}$ is centrosymmetric and hermitian

$$\hat{\underline{\mathbf{R}}}_{p_2} = \mathbf{J} \hat{\underline{\mathbf{R}}}_{p_2}^* \mathbf{J}, \quad \hat{\underline{\mathbf{R}}}_{p_2} = \hat{\underline{\mathbf{R}}}_{p_2}^H.$$

$\hat{\underline{\mathbf{R}}}_{p_2}$ is a LS-based stochastic approximation of the $(p_1 + 1)(p_2 + 1) \times (p_1 + 1)(p_2 + 1)$ autocorrelation matrix $\underline{\mathbf{R}}_{p_2}$ in the known autocorrelation case; however, it does not have the doubly Toeplitz structure of the known autocorrelation case, but it does have a *near-to-doubly-Toeplitz* structure which can be exploited to develop a computationally efficient algorithm for the solution of the 2-D modified covariance LS-based MVSE, which will be presented in Section 6.3.1. When either p_1 or p_2 is equal to zero, the 2-D LP solution reduces to the usual 1-D LP solution, so that the 2-D modified covariance LS-based MVSE in Eq. 5.30 yields numerical results equal to the 1-D modified covariance LS-based MVSE solution. The 2-D covariance LS-based MVSE has same dimension-reduction solution property.

Similarly, the 2-D modified covariance LS-based MVSE has identical numerical solutions in Q_2 , Q_3 and Q_4 as that obtained in Q_1 . Therefore, it is not necessary to calculate the 2-D modified covariance LS-based MVSE for quadrants Q_2 to Q_4 as well.

6. FAST SOLUTIONS FOR TWO-DIMENSIONAL MINIMUM VARIANCE SPECTRAL ESTIMATION

This chapter presents the development of the two new fast computational solutions of the 2-D LS-based MVSE in the covariance case and modified covariance cases, whose flowcharts are illustrated in Fig. 1.4 and Fig. 1.5. We will start from a review of the fast computational solution of the 2-D ACS-based MVSE.

6.1. Autocorrelation-Based 2-D Minimum Variance Spectral Estimation: Doubly-Toeplitz Autocorrelation Case

6.1.1. Review Fast Computational Solution

Marple [24] developed a fast algorithm in the case of the 2-D lattice method. This algorithm was developed as the result of insights into the fast algorithm of the multichannel MVSE [14], which recursively solved the multichannel Yule-Walker normal equations for all intermediate orders from order 1 to the desired highest order p_2 . The fast 2-D algorithm is based on solving for a block parameter AR matrix \mathbf{A} of the 2-D lattice linear prediction, rather than based on the direct solution for \mathbf{h} in Eq. 5.2. The special Yule-Walker normal equations of order p_2 are

$$\underline{\mathbf{R}}_{p_2} \begin{pmatrix} \mathbf{I} \\ \mathbf{A}_{p_2}[1] \\ \vdots \\ \mathbf{A}_{p_2}[p_2] \end{pmatrix} = \begin{pmatrix} \mathbf{P}_{p_2} \\ \mathbf{0} \\ \vdots \\ \mathbf{0} \end{pmatrix}. \quad (6.1)$$

Since the doubly-Toeplitz autocorrelation matrix $\underline{\mathbf{R}}_{p_2}$ is hermitian and centrosymmetric, the Yule-Walker normal equation Eq. 6.1 may alternatively be expressed

as

$$\underline{\mathbf{R}}_{p_2} \begin{pmatrix} \mathbf{J} \mathbf{A}_{p_2}^* [p_2] \mathbf{J} \\ \mathbf{J} \mathbf{A}_{p_2}^* [p_2 - 1] \mathbf{J} \\ \vdots \\ \mathbf{I} \end{pmatrix} = \begin{pmatrix} \mathbf{0} \\ \mathbf{0} \\ \vdots \\ \mathbf{J} \mathbf{P}_{p_2}^* \mathbf{J} \end{pmatrix} \quad (6.2)$$

in which the $(p_1 + 1)(p_2 + 1) \times (p_1 + 1)(p_2 + 1)$ dimensional block matrix $\underline{\mathbf{R}}_{p_2}$ is defined in Eq. 5.5 and Eq. 5.6. The special 2-D AR parameters $\mathbf{A}_{p_2}[k]$ for $0 \leq k \leq p_2$ and special 2-D AR variance \mathbf{P}_{p_2} are $(p_1 + 1) \times (p_1 + 1)$ square matrices. The variance \mathbf{P}_{p_2} is a positive definite hermitian matrix. The \mathbf{I} , $\mathbf{0}$ and \mathbf{J} matrices are the $(p_1 + 1) \times (p_1 + 1)$ identity matrix, zero matrix, and reflection matrix, respectively. The $(p_1 + 1) \times (p_1 + 1)$ dimensional special 2-D AR parameters $\mathbf{A}_m[m]$ and special 2-D AR variance \mathbf{P}_m for $0 \leq m \leq p_2$ can be solved by the 2-D Levinson recursion for the Yule-Walker equations Eq. 6.1. Analogous to the inverse expressions of the 1-D autocorrelation matrix and the multichannel autocorrelation matrix in [15], one can develop a similar inverse formula for the 2-D doubly-Toeplitz autocorrelation matrix, which is expressed as the difference of the products of triangular Toeplitz matrices

$$\underline{\mathbf{R}}_{p_2}^{-1} = \underline{\mathbf{A}}_{p_2} (\underline{\mathbf{P}}_{p_2}^A)^{-1} \underline{\mathbf{A}}_{p_2}^H - \underline{\mathbf{B}}_{p_2} (\underline{\mathbf{P}}_{p_2}^B)^{-1} \underline{\mathbf{B}}_{p_2}^H \quad (6.3)$$

where the $(p_2 + 1) \times (p_2 + 1)$ block matrices are formed as

$$\underline{\mathbf{A}}_{p_2} = \begin{pmatrix} \mathbf{I} & \mathbf{0} & \cdots & \mathbf{0} \\ \mathbf{A}_{p_2}[1] & \ddots & \ddots & \vdots \\ \vdots & \ddots & \ddots & \mathbf{0} \\ \mathbf{A}_{p_2}[p_2] & \cdots & \mathbf{A}_{p_2}[1] & \mathbf{I} \end{pmatrix}, \quad (6.4)$$

$$\underline{\mathbf{B}}_{p_2} = \begin{pmatrix} \mathbf{0} & \mathbf{0} & \cdots & \mathbf{0} \\ (\mathbf{J}\mathbf{A}_{p_2}^*[p_2]\mathbf{J}) & \ddots & \ddots & \vdots \\ \vdots & \ddots & \ddots & \mathbf{0} \\ (\mathbf{J}\mathbf{A}_{p_2}^*[1]\mathbf{J}) & \cdots & (\mathbf{J}\mathbf{A}_{p_2}^*[p_2]\mathbf{J}) & \mathbf{0} \end{pmatrix}, \quad (6.5)$$

and the $(p_2 + 1) \times (p_2 + 1)$ block matrices are

$$\underline{\mathbf{P}}_{p_2}^A = \begin{pmatrix} \mathbf{P}_{p_2} & \mathbf{0} & \cdots & \mathbf{0} \\ \mathbf{0} & \ddots & \ddots & \vdots \\ \vdots & \ddots & \ddots & \mathbf{0} \\ \mathbf{0} & \cdots & \mathbf{0} & \mathbf{P}_{p_2} \end{pmatrix}, \quad (6.6)$$

$$\underline{\mathbf{P}}_{p_2}^B = \begin{pmatrix} (\mathbf{J}\mathbf{P}_{p_2}^*\mathbf{J}) & \mathbf{0} & \cdots & \mathbf{0} \\ \mathbf{0} & \ddots & \ddots & \vdots \\ \vdots & \ddots & \ddots & \mathbf{0} \\ \mathbf{0} & \cdots & \mathbf{0} & (\mathbf{J}\mathbf{P}_{p_2}^*\mathbf{J}) \end{pmatrix}, \quad (6.7)$$

and the $(p_1 + 1) \times (p_1 + 1)$ matrix

$$\mathbf{P}_{p_2} = \begin{pmatrix} \rho_{p_2} & \cdots & 0 \\ \vdots & \ddots & \vdots \\ 0 & \cdots & \rho_{p_2} \end{pmatrix} \quad (6.8)$$

is formed from the ρ_{p_2} output variance of linear prediction. Substituting the inverse formula Eq. 6.3 into Eq. 5.11 and performing some matrix algebra yields the alternative 2-D MVSE formulation

$$P_{2\text{DMV-acs}}(f_1, f_2) = \frac{T_1 T_2}{\sum_{m=-p_1}^{p_1} \sum_{k=-p_2}^{p_2} \alpha[m, k] e^{-j2\pi[f_1 m T_1 + f_2 k T_2]}} \quad (6.9)$$

where $\alpha[m, k]$ is obtained from the 2-D FIR filter parameters \mathbf{A} by a weighted correlation. For its definition and derivation one could refer to Eq. 6.36 in Section 6.2.1. A 2-D FFT can be used for both the fast correlation computation of $\alpha[m, k]$ and for evaluating the denominator expression of Eq. 6.9 over the range $[-1/2T_1 \leq f_1 \leq 1/2T_1, -1/2T_2 \leq f_2 \leq 1/2T_2]$. The fast computational algorithm requires computational complexity proportional to order p^5 and memory storage proportional to order p^3 , compared to the computational complexity of p^6 and storage of p^4 required by direct evaluation of the 2-D MVSE function in Eq. 5.11.

In a similar manner, one can define the PSD of Eq. 5.11 in the second, third and forth quadrants (Q_2 , Q_3 and Q_4). The numerical results will be identical to Eq. 5.11 and Eq. 6.9, that is, there is no numerical difference among the first, second, third and fourth quadrant minimum variance estimators, in contrast to the quadrant-based AR spectral estimates which are generally numerically different and biased [11].

The next two sections will introduce the derivation of 2-D covariance least-squares-based minimum variance spectral estimation and its fast computational algorithm.

6.1.2. Computation and Storage Counts

The Table 6.1 summarizes the savings of the computational complexity and the memory storage required by the fast 2-D ACS-based MVSE in Eq. 6.9 versus the direct method in Eq. 5.11. The computational complexity of the fast solutions of the 2-D ACS-based MVSE is proportional to p^5 , with memory storage requirements proportional to p^3 , versus p^6 computation and p^4 storage if solved by using the direct 2-D solution approach.

2-D ACS-based MVSE		
$(p_1 = p_2 = p, N_1 = N_2 = N, N_{f1} = N_{f2} = N_f)$		
	Fast Solution	Direct Method
Computational	$\times \frac{13}{8}p^5 + 2N_f \log_2(N_f)$	$\frac{2}{3}p^6 + \frac{5}{3}p^4 - \frac{1}{3}p^2 + 2N_f^2$
Complexity	$+ \frac{3}{2}p^5 + 2N_f \log_2(N_f)$	$\frac{2}{3}p^6 - \frac{2}{3}p^2 + 2N_f^2$
Storage	$3p^3 + 2 + N_f$	$p^4 + N_f$

TABLE 6.1. Comparison of the Computation and Storage Counts for 2-D auto-correlation-based (ACS-Based) MVSE. Note: p_1, p_2 are the orders of the estimator in 2-D directions, N_1, N_2 are the size of 2-D data sequence, N_{f1}, N_{f2} are the numbers of 2-D FFT frequency bins, \times is the number of complex multiplications, and $+$ is the number of complex additions.

6.2. Least-Squares-Based 2-D Minimum Variance Spectral Estimation: Covariance Case

6.2.1. Development of Fast Computational Solution

The computational burden of 2-D LS-MVSE is twofold. First, calculating the inverse autocorrelation matrix is time consuming. Second, the power spectral estimator has to be calculated over all frequencies (f_1, f_2) of interest. To develop a fast computational algorithm of the 2-D least-squares-based minimum variance spectral estimator, the first step is to decompose the inverse matrix of the *near-to-doubly-Toeplitz* 2-D data product matrix. Our proof is analogous to the development of the inverse doubly Toeplitz autocorrelation matrix in Eq. 6.3, which was expressed in terms of differences of products of triangular Toeplitz matrices

formed from the 2-D AR parameters. This section will develop the derivation of the inverse formula of the *near-to-doubly-Toeplitz* 2-D data product matrix.

Inspired by Eq. 6.1 and Eq. 6.2, the decomposition of the inverse 2-D *near-to-doubly-Toeplitz* data product matrix $\hat{\underline{\mathbf{R}}}_{p_2}^{-1}$ is based on the solution of the Yule-Walker normal equations of order p_2

$$\hat{\underline{\mathbf{R}}}_{p_2} \begin{pmatrix} \mathbf{I} \\ \bar{\underline{\mathbf{a}}}_{p_2} \end{pmatrix} = \begin{pmatrix} \bar{\mathbf{P}}_{p_2}^A \\ \mathbf{0} \end{pmatrix} \quad (6.10)$$

and

$$\hat{\underline{\mathbf{R}}}_{p_2} \begin{pmatrix} \mathbf{J} \bar{\underline{\mathbf{b}}}_{p_2} \\ \mathbf{I} \end{pmatrix} = \begin{pmatrix} \mathbf{0} \\ \bar{\mathbf{P}}_{p_2}^B \end{pmatrix} \quad (6.11)$$

where the new special AR vectors of dimension $(p_1 + 1)(p_2 + 1) \times (p_1 + 1)$ are

$$\bar{\underline{\mathbf{a}}}_{p_2}^T = \left(\bar{\mathbf{A}}_{p_2}^T[1], \dots, \bar{\mathbf{A}}_{p_2}^T[p_2] \right) \quad (6.12)$$

and

$$\bar{\underline{\mathbf{b}}}_{p_2}^T = \left(\bar{\mathbf{B}}_{p_2}^T[1], \dots, \bar{\mathbf{B}}_{p_2}^T[p_2] \right), \quad (6.13)$$

in which $\bar{\mathbf{A}}_{p_2}[k]$ and $\bar{\mathbf{B}}_{p_2}[k]$ for $0 \leq k \leq p_2$ are $(p_1 + 1) \times (p_1 + 1)$ square matrices and $\bar{\mathbf{A}}_{p_2}[0] = \bar{\mathbf{B}}_{p_2}[0] = \mathbf{I}$ by definition. The solutions of the Yule-Walker normal equations have been developed by Marple in [20]. Both $\bar{\mathbf{P}}_{p_2}^A$ and $\bar{\mathbf{P}}_{p_2}^B$ are positive definite square hermitian matrices of dimension $(p_1 + 1) \times (p_1 + 1)$. The $(p_1 + 1)(p_2 + 1) \times (p_1 + 1)(p_2 + 1)$ dimensional $\hat{\underline{\mathbf{R}}}_{p_2}$ is defined in Eq. 5.22. $\hat{\underline{\mathbf{R}}}_{p_2}$ is not Toeplitz, but it does have hermitian symmetry,

$$\hat{\underline{\mathbf{R}}}_{p_2} = (\hat{\underline{\mathbf{R}}}_{p_2})^H.$$

Based on Eq. 5.22, the crucial decompositions of the inverse of a *near-to-doubly-Toeplitz* data product matrix are the following order-index partitions of the $(p_1 + 1)(p_2 + 1) \times (p_1 + 1)(p_2 + 1)$ dimensional matrix $\hat{\underline{\mathbf{R}}}_{p_2}$

$$\hat{\underline{\mathbf{R}}}_{p_2} = \begin{pmatrix} \hat{\underline{\mathbf{R}}}'_{p_2-1} & \hat{\underline{\mathbf{r}}}'_{p_2} \\ (\hat{\underline{\mathbf{r}}}'_{p_2})^H & \hat{\underline{\mathbf{R}}}_{p_2}[p_2, p_2] \end{pmatrix} \quad (6.14)$$

or

$$\hat{\underline{\mathbf{R}}}_{p_2} = \begin{pmatrix} \hat{\underline{\mathbf{R}}}_{p_2}[0, 0] & (\hat{\underline{\mathbf{r}}}'')^H_{p_2} \\ \hat{\underline{\mathbf{r}}}_{p_2}'' & \hat{\underline{\mathbf{R}}}_{p_2-1}'' \end{pmatrix} \quad (6.15)$$

in which the $(p_1 + 1)(p_2 + 1) \times (p_1 + 1)$ block vectors are defined as

$$(\hat{\underline{\mathbf{r}}}'_{p_2})^H = \left(\hat{\underline{\mathbf{R}}}_{p_2}^H[0, p_2], \dots, \hat{\underline{\mathbf{R}}}_{p_2}^H[p_2 - 1, p_2] \right), \quad (\hat{\underline{\mathbf{r}}}'')^H_{p_2} = \left(\hat{\underline{\mathbf{R}}}_{p_2}^H[1, 0], \dots, \hat{\underline{\mathbf{R}}}_{p_2}^H[p_2, 0] \right).$$

Also crucial are the following time-index partitions,

$$\hat{\underline{\mathbf{R}}}'_{p_2} = \sum_{m=p_2+2}^{N_2} \underline{\mathbf{x}}_{p_2}^H[m] \underline{\mathbf{x}}_{p_2}[m] = \hat{\underline{\mathbf{R}}}_{p_2} - \underline{\mathbf{x}}_{p_2}^H[p_2 + 1] \underline{\mathbf{x}}_{p_2}[p_2 + 1] \quad (6.16)$$

and

$$\hat{\underline{\mathbf{R}}}_{p_2}'' = \sum_{m=p_2+1}^{N_2-1} \underline{\mathbf{x}}_{p_2}^H[m] \underline{\mathbf{x}}_{p_2}[m] = \hat{\underline{\mathbf{R}}}_{p_2} - \underline{\mathbf{x}}_{p_2}^H[N_2] \underline{\mathbf{x}}_{p_2}[N_2], \quad (6.17)$$

where the $(N_1 - p_1) \times (p_1 + 1)(p_2 + 1)$ dimensional data column block vector is

$$\underline{\mathbf{x}}_{p_2}[m] = (\mathbf{x}[m], \mathbf{x}[m - 1], \dots, \mathbf{x}[m - p_2]) \quad (6.18)$$

in which $\mathbf{x}[m]$, $1 \leq m \leq N_2$, are rectangular Toeplitz data matrices of dimension $(N_1 - p_1) \times (p_1 + 1)$ defined in Eq. 5.20. Note that Eq. 5.19 can be alternatively expressed as

$$\underline{\mathbf{X}}_{p_2} = \begin{pmatrix} \underline{\mathbf{x}}_{p_2}[p_2 + 1] \\ \underline{\mathbf{x}}_{p_2}[p_2] \\ \vdots \\ \underline{\mathbf{x}}_{p_2}[N_2] \end{pmatrix}.$$

of dimension $(N_1 - p_1)(N_2 - p_2) \times (p_1 + 1)(p_2 + 1)$. The pair of auxiliary $(p_1 + 1)(p_2 + 1) \times (N_1 - p_1)$ -dimensional block vectors $\bar{\underline{\mathbf{c}}}_{p_2}^T = (\bar{\mathbf{C}}_{p_2}^T[0], \dots, \bar{\mathbf{C}}_{p_2}^T[p_2])$ and $\bar{\underline{\mathbf{d}}}_{p_2}^T = (\bar{\mathbf{D}}_{p_2}^T[0], \dots, \bar{\mathbf{D}}_{p_2}^T[p_2])$ are also critical to the fast algorithm. They are defined by

$$\hat{\underline{\mathbf{R}}}_{p_2} \bar{\underline{\mathbf{c}}}_{p_2} = \underline{\mathbf{x}}_{p_2}^*[N_2], \quad \bar{\mathbf{P}}_{p_2}^C = \mathbf{I} - \underline{\mathbf{x}}_{p_2}[N_2] \bar{\underline{\mathbf{c}}}_{p_2} \quad (6.19)$$

and

$$\hat{\underline{\mathbf{R}}}_{p_2} \bar{\underline{\mathbf{d}}}_{p_2} = \underline{\mathbf{x}}_{p_2}^*[p_2 + 1], \quad \bar{\mathbf{P}}_{p_2}^D = \mathbf{I} - \underline{\mathbf{x}}_{p_2}[p_2 + 1] \bar{\underline{\mathbf{d}}}_{p_2} \quad (6.20)$$

where $(p_1 + 1) \times (p_1 + 1)$ -dimensional positive definite square hermitian matrices $\bar{\mathbf{P}}_{p_2}^C$ and $\bar{\mathbf{P}}_{p_2}^D$, considered as matrix gain adjustment factors associated with the gain adjustment parameter vectors $\bar{\underline{\mathbf{c}}}_{p_2}$ and $\bar{\underline{\mathbf{d}}}_{p_2}$. The diagonal values of both $\bar{\mathbf{P}}_{p_2}^C$ and $\bar{\mathbf{P}}_{p_2}^D$ are real-valued. The initial conditions of Eq. 6.19 and Eq. 6.20 are

$$\hat{\underline{\mathbf{R}}}_0[0, 0] \bar{\mathbf{C}}_0[0] = \mathbf{x}^*[N_2] \quad (6.21)$$

and

$$\hat{\underline{\mathbf{R}}}_0[0, 0] \bar{\mathbf{D}}_0[0] = \mathbf{x}^*[p_2 + 1]. \quad (6.22)$$

The solutions of Eq.6.19 and Eq.6.20 have been reported by Marple in [20].

Substituting the submatrix partitions Eq. 6.14 and Eq. 6.15 into the left sides of the Yule-Walker normal equations Eq. 6.11 and Eq. 6.10 yields, respectively,

$$\begin{pmatrix} \hat{\underline{\mathbf{R}}}_{p_2-1}' & \hat{\underline{\mathbf{r}}}_{p_2}' \\ (\hat{\underline{\mathbf{r}}}_{p_2}')^H & \hat{\mathbf{R}}_{p_2}[p_2, p_2] \end{pmatrix} \begin{pmatrix} \bar{\mathbf{B}}_{p_2}[p_2+1] \\ \vdots \\ \bar{\mathbf{B}}_{p_2}[1] \\ \mathbf{I} \end{pmatrix} = \begin{pmatrix} \mathbf{0} \\ \vdots \\ \mathbf{0} \\ \bar{\mathbf{P}}_{p_2}^B \end{pmatrix} \quad (6.23)$$

$$\begin{pmatrix} \hat{\mathbf{R}}_{p_2}[0, 0] & (\hat{\underline{\mathbf{r}}}_{p_2}'')^H \\ \hat{\underline{\mathbf{r}}}_{p_2}'' & \hat{\underline{\mathbf{R}}}_{p_2-1}'' \end{pmatrix} \begin{pmatrix} \mathbf{I} \\ \bar{\mathbf{A}}_{p_2}[1] \\ \vdots \\ \bar{\mathbf{A}}_{p_2}[p_2+1] \end{pmatrix} = \begin{pmatrix} \bar{\mathbf{P}}_{p_2}^A \\ \mathbf{0} \\ \vdots \\ \mathbf{0} \end{pmatrix}. \quad (6.24)$$

The following relations can be easily derived from Eq. 6.23 and Eq. 6.24

$$\hat{\underline{\mathbf{r}}}_{p_2}' = -\hat{\underline{\mathbf{R}}}_{p_2-1}' \mathbf{J} \bar{\underline{\mathbf{b}}}_{p_2}, \quad (\hat{\underline{\mathbf{r}}}_{p_2}')^H \mathbf{J} \bar{\underline{\mathbf{b}}}_{p_2} + \hat{\mathbf{R}}_{p_2}[p_2, p_2] = \bar{\mathbf{P}}_{p_2}^B \quad (6.25)$$

and

$$\hat{\underline{\mathbf{r}}}_{p_2}'' = -\hat{\underline{\mathbf{R}}}_{p_2-1}'' \bar{\underline{\mathbf{a}}}_{p_2}, \quad (\hat{\underline{\mathbf{r}}}_{p_2}'')^H \bar{\underline{\mathbf{a}}}_{p_2} + \hat{\mathbf{R}}_{p_2}[0, 0] = \bar{\mathbf{P}}_{p_2}^A. \quad (6.26)$$

Analogous to the partitioned matrix inversion lemma and the specialized form of the augmented matrix inversion lemma in [15], the inverse matrix of Eq. 6.14 can be expressed as

$$\hat{\underline{\mathbf{R}}}_{p_2}^{-1} = \begin{pmatrix} (\hat{\underline{\mathbf{R}}}_{p_2-1}')^{-1} + (\hat{\underline{\mathbf{R}}}_{p_2-1}')^{-1} \hat{\underline{\mathbf{r}}}_{p_2}' \Delta_{p_2}^{-1} (\hat{\underline{\mathbf{r}}}_{p_2}')^H (\hat{\underline{\mathbf{R}}}_{p_2-1}')^{-1}, & -(\hat{\underline{\mathbf{R}}}_{p_2-1}')^{-1} \hat{\underline{\mathbf{r}}}_{p_2}' \Delta_{p_2}^{-1} \\ -\Delta_{p_2}^{-1} (\hat{\underline{\mathbf{r}}}_{p_2}')^H (\hat{\underline{\mathbf{R}}}_{p_2-1}')^{-1}, & \Delta_{p_2}^{-1} \end{pmatrix} \quad (6.27)$$

in which

$$\begin{aligned} \Delta_{p_2} &= \hat{\mathbf{R}}_{p_2}[p_2, p_2] - (\hat{\underline{\mathbf{r}}}_{p_2}')^H (\hat{\underline{\mathbf{R}}}_{p_2-1}')^{-1} \hat{\underline{\mathbf{r}}}_{p_2}' \\ &= \hat{\mathbf{R}}_{p_2}[p_2, p_2] + (\hat{\underline{\mathbf{r}}}_{p_2}')^H \mathbf{J} \bar{\underline{\mathbf{b}}}_{p_2} = \bar{\mathbf{P}}_{p_2}^B, \end{aligned} \quad (6.28)$$

so that $\mathbf{\Delta}_{p_2}^{-1} = (\bar{\mathbf{P}}_{p_2}^B)^{-1}$. Substituting Eq. 6.28, Eq. 6.25 and Eq. 6.20 into Eq. 6.27, $\hat{\mathbf{R}}_{p_2}^{-1}$ can then be rewritten as

$$\begin{aligned} \hat{\mathbf{R}}_{p_2}^{-1} &= \begin{pmatrix} (\hat{\mathbf{R}}'_{p_2-1})^{-1} + \mathbf{J} \bar{\mathbf{b}}_{p_2} (\bar{\mathbf{P}}_{p_2}^B)^{-1} \bar{\mathbf{b}}_{p_2}^H \mathbf{J}, & \mathbf{J} \bar{\mathbf{b}}_{p_2} (\bar{\mathbf{P}}_{p_2}^B)^{-1} \\ (\bar{\mathbf{P}}_{p_2}^B)^{-1} \bar{\mathbf{b}}_{p_2}^H \mathbf{J}, & (\bar{\mathbf{P}}_{p_2}^B)^{-1} \end{pmatrix} \\ &= \begin{pmatrix} (\hat{\mathbf{R}}'_{p_2-1})^{-1} + \bar{\mathbf{d}}_{p_2-1} (\bar{\mathbf{P}}_{p_2-1}^D)^{-1} \bar{\mathbf{d}}_{p_2-1}^H + \mathbf{J} \bar{\mathbf{b}}_{p_2} (\bar{\mathbf{P}}_{p_2}^B)^{-1} \bar{\mathbf{b}}_{p_2}^H \mathbf{J}, & \mathbf{J} \bar{\mathbf{b}}_{p_2} (\bar{\mathbf{P}}_{p_2}^B)^{-1} \\ (\bar{\mathbf{P}}_{p_2}^B)^{-1} \bar{\mathbf{b}}_{p_2}^H \mathbf{J}, & (\bar{\mathbf{P}}_{p_2}^B)^{-1} \end{pmatrix} \end{aligned} \quad (6.29)$$

Alternatively, the inverse matrix Eq. 6.15 can also be expressed as

$$\hat{\mathbf{R}}_{p_2}^{-1} = \begin{pmatrix} (\bar{\mathbf{P}}_{p_2}^A)^{-1}, & (\bar{\mathbf{P}}_{p_2}^A)^{-1} \bar{\mathbf{a}}_{p_2}^H \\ \bar{\mathbf{a}}_{p_2} (\bar{\mathbf{P}}_{p_2}^A)^{-1}, & \hat{\mathbf{R}}_{p_2-1}^{-1} + \bar{\mathbf{c}}_{p_2-1} (\bar{\mathbf{P}}_{p_2-1}^C)^{-1} \bar{\mathbf{c}}_{p_2-1}^H + \bar{\mathbf{a}}_{p_2} (\bar{\mathbf{P}}_{p_2}^A)^{-1} \bar{\mathbf{a}}_{p_2}^H \end{pmatrix}. \quad (6.30)$$

Assume $\bar{\mathbf{u}}_{p_2}[j, k]$ is a $(p_1 + 1) \times (p_1 + 1)$ block element of $\hat{\mathbf{R}}_{p_2}^{-1}$

$$\hat{\mathbf{R}}_{p_2}^{-1} = \begin{pmatrix} \bar{\mathbf{u}}_{p_2}[0, 0] & \bar{\mathbf{u}}_{p_2}[0, 1] & \cdots & \bar{\mathbf{u}}_{p_2}[0, p_2] \\ \bar{\mathbf{u}}_{p_2}[1, 0] & \bar{\mathbf{u}}_{p_2}[1, 1] & \cdots & \bar{\mathbf{u}}_{p_2}[1, p_2] \\ \vdots & \vdots & \ddots & \vdots \\ \bar{\mathbf{u}}_{p_2}[p_2, 0] & \bar{\mathbf{u}}_{p_2}[p_2, 1] & \cdots & \bar{\mathbf{u}}_{p_2}[p_2, p_2] \end{pmatrix} \quad (6.31)$$

of $(p_1 + 1)(p_2 + 1) \times (p_1 + 1)(p_2 + 1)$ dimension. From above, the following relations may be found

$$\begin{aligned} \bar{\mathbf{u}}_{p_2}[0, 0] &= (\bar{\mathbf{P}}_{p_2}^A)^{-1}, & \bar{\mathbf{u}}_{p_2}[p_2, p_2] &= (\bar{\mathbf{P}}_{p_2}^B)^{-1}, \\ \bar{\mathbf{u}}_{p_2}[j, 0] &= \bar{\mathbf{A}}_{p_2}[j] (\bar{\mathbf{P}}_{p_2}^A)^{-1}, & \bar{\mathbf{u}}_{p_2}[0, k] &= (\bar{\mathbf{P}}_{p_2}^A)^{-1} \bar{\mathbf{A}}_{p_2}^H[k], \\ \bar{\mathbf{u}}_{p_2}[p_2, p_2 - k] &= (\bar{\mathbf{P}}_{p_2}^B)^{-1} \bar{\mathbf{B}}_{p_2}^H[k], & \bar{\mathbf{u}}_{p_2}[p_2 - j, p_2] &= \bar{\mathbf{B}}_{p_2}[j] (\bar{\mathbf{P}}_{p_2}^B)^{-1} \end{aligned}$$

for $1 \leq j, k \leq p_2$, and

$$\begin{aligned}
\bar{\mathbf{u}}_{p_2}[j, k] &= \bar{\mathbf{u}}_{p_2-1}[j, k] + \bar{\mathbf{D}}_{p_2-1}[j](\bar{\mathbf{P}}_{p_2-1}^D)^{-1}\bar{\mathbf{D}}_{p_2-1}^H[k] \\
&\quad + \bar{\mathbf{B}}_{p_2}[p_2 - j](\bar{\mathbf{P}}_{p_2}^B)^{-1}\bar{\mathbf{B}}_{p_2}^H[p_2 - k], \\
\bar{\mathbf{u}}_{p_2}[j + 1, k + 1] &= \bar{\mathbf{u}}_{p_2-1}[j, k] + \bar{\mathbf{C}}_{p_2-1}[j](\bar{\mathbf{P}}_{p_2-1}^C)^{-1}\bar{\mathbf{C}}_{p_2-1}^H[k] \\
&\quad + \bar{\mathbf{A}}_{p_2}[j + 1](\bar{\mathbf{P}}_{p_2}^A)^{-1}\bar{\mathbf{A}}_{p_2}^H[k + 1],
\end{aligned}$$

for $0 \leq j, k \leq p_2 - 1$. Combining the last two equations as follows to eliminate $\bar{\mathbf{u}}_{p_2}[j, k]$ will then yield

$$\begin{aligned}
\bar{\mathbf{u}}_{p_2}[j + 1, k + 1] &= \bar{\mathbf{u}}_{p_2}[j, k] + \bar{\mathbf{A}}_{p_2}[j + 1](\bar{\mathbf{P}}_{p_2}^A)^{-1}\bar{\mathbf{A}}_{p_2}^H[k + 1] \\
&\quad - \bar{\mathbf{B}}_{p_2}[p_2 - j](\bar{\mathbf{P}}_{p_2}^B)^{-1}\bar{\mathbf{B}}_{p_2}^H[p_2 - k] + \bar{\mathbf{C}}_{p_2-1}[j](\bar{\mathbf{P}}_{p_2-1}^C)^{-1}\bar{\mathbf{C}}_{p_2-1}^H[k] \\
&\quad - \bar{\mathbf{D}}_{p_2-1}[j](\bar{\mathbf{P}}_{p_2-1}^D)^{-1}\bar{\mathbf{D}}_{p_2-1}^H[k].
\end{aligned} \tag{6.32}$$

Eq. 6.33 is a recursive relationship that permits all inverse elements to be computed from knowledge of only the $\bar{\mathbf{A}}$ and $\bar{\mathbf{B}}$ vectors. The following inverse matrix relationship may also be developed from Eq. 6.33

$$\begin{aligned}
\hat{\underline{\mathbf{R}}}_{p_2}^{-1} &= \underline{\bar{\mathbf{A}}}_{p_2}(\bar{\mathbf{P}}_{p_2}^A)^{-1}\underline{\bar{\mathbf{A}}}_{p_2}^H - \underline{\bar{\mathbf{B}}}_{p_2}(\bar{\mathbf{P}}_{p_2}^B)^{-1}\underline{\bar{\mathbf{B}}}_{p_2}^H \\
&\quad + \underline{\bar{\mathbf{C}}}_{p_2-1}(\bar{\mathbf{P}}_{p_2-1}^C)^{-1}\underline{\bar{\mathbf{C}}}_{p_2-1}^H - \underline{\bar{\mathbf{D}}}_{p_2-1}(\bar{\mathbf{P}}_{p_2-1}^D)^{-1}\underline{\bar{\mathbf{D}}}_{p_2-1}^H
\end{aligned} \tag{6.33}$$

in which the $(p_1 + 1)(p_2 + 1) \times (p_1 + 1)(p_2 + 1)$ block triangular Toeplitz matrices

$$\begin{aligned}
\underline{\bar{\mathbf{A}}}_{p_2} &= \begin{pmatrix} \mathbf{I} & \mathbf{0} & \cdots & \mathbf{0} \\ \bar{\mathbf{A}}_{p_2}[1] & \ddots & \ddots & \vdots \\ \vdots & \ddots & \ddots & \mathbf{0} \\ \bar{\mathbf{A}}_{p_2}[p_2] & \cdots & \bar{\mathbf{A}}_{p_2}[1] & \mathbf{I} \end{pmatrix} \\
\underline{\bar{\mathbf{B}}}_{p_2} &= \begin{pmatrix} \mathbf{0} & \cdots & \cdots & \mathbf{0} \\ \bar{\mathbf{B}}_{p_2}[p_2] & \ddots & \ddots & \mathbf{0} \\ \vdots & \ddots & \ddots & \vdots \\ \bar{\mathbf{B}}_{p_2}[1] & \cdots & \bar{\mathbf{B}}_{p_2}[p_2] & \mathbf{0} \end{pmatrix}
\end{aligned}$$

and block diagonal matrices

$$(\bar{\mathbf{P}}_{p_2}^A)^{-1} = \begin{pmatrix} (\bar{\mathbf{P}}_{p_2}^A)^{-1} & \cdots & \mathbf{0} \\ \vdots & \ddots & \vdots \\ \mathbf{0} & \cdots & (\bar{\mathbf{P}}_{p_2}^A)^{-1} \end{pmatrix}$$

$$(\bar{\mathbf{P}}_{p_2}^B)^{-1} = \begin{pmatrix} (\bar{\mathbf{P}}_{p_2}^B)^{-1} & \cdots & \mathbf{0} \\ \vdots & \ddots & \vdots \\ \mathbf{0} & \cdots & (\bar{\mathbf{P}}_{p_2}^B)^{-1} \end{pmatrix}$$

where each block element is a $(p_1 + 1) \times (p_1 + 1)$ dimensional matrix. The $(p_1 + 1)(p_2 + 1) \times (N_1 - p_1)(p_2 + 1)$ -dimensional triangular Toeplitz matrices

$$\bar{\mathbf{C}}_{p_2-1} = \begin{pmatrix} \mathbf{0} & \cdots & \cdots & \mathbf{0} \\ \bar{\mathbf{C}}_{p_2-1}[0] & \ddots & \ddots & \mathbf{0} \\ \vdots & \ddots & \ddots & \vdots \\ \bar{\mathbf{C}}_{p_2-1}[p_2 - 1] & \cdots & \bar{\mathbf{C}}_{p_2-1}[0] & \mathbf{0} \end{pmatrix}$$

$$\bar{\mathbf{D}}_{p_2-1} = \begin{pmatrix} \mathbf{0} & \cdots & \cdots & \mathbf{0} \\ \bar{\mathbf{D}}_{p_2-1}[0] & \ddots & \ddots & \mathbf{0} \\ \vdots & \ddots & \ddots & \vdots \\ \bar{\mathbf{D}}_{p_2-1}[p_2 - 1] & \cdots & \bar{\mathbf{D}}_{p_2-1}[0] & \mathbf{0} \end{pmatrix}$$

each has block elements that are $(p_1 + 1) \times (N_1 - p_1)$ dimensional matrices. The block diagonal matrices

$$(\bar{\mathbf{P}}_{p_2-1}^C)^{-1} = \begin{pmatrix} (\bar{\mathbf{P}}_{p_2-1}^C)^{-1} & \cdots & \mathbf{0} \\ \vdots & \ddots & \vdots \\ \mathbf{0} & \cdots & (\bar{\mathbf{P}}_{p_2-1}^C)^{-1} \end{pmatrix}$$

$$(\bar{\mathbf{P}}_{p_2-1}^D)^{-1} = \begin{pmatrix} (\bar{\mathbf{P}}_{p_2-1}^D)^{-1} & \cdots & \mathbf{0} \\ \vdots & \ddots & \vdots \\ \mathbf{0} & \cdots & (\bar{\mathbf{P}}_{p_2-1}^D)^{-1} \end{pmatrix}$$

are of dimension $(N_1 - p_1)(p_2 + 1) \times (N_1 - p_1)(p_2 + 1)$ and each block element is of dimension $(N_1 - p_1) \times (N_1 - p_1)$. Based on the substitution of Eq. 6.33 into Eq. 5.21, the 2-D covariance LS-MVSE can be formulated as

$$\hat{P}_{2\text{DMV-cov}}(f_1, f_2) = \frac{T_1 T_2}{\mathbf{e}_{p_2}^H(f_1) \left(\sum_{k=-p_2}^{p_2} \hat{\Psi}[k] e^{-j2\pi f_2 k T_2} \right) \mathbf{e}_{p_2}(f_1)} \quad (6.34)$$

in which the $(p_1+1) \times (p_1+1)$ dimension matrix $\hat{\Psi}$, formed as a weighted correlation of $\bar{\mathbf{A}}$ and $\bar{\mathbf{B}}$ elements, is defined as

$$\hat{\Psi}[k] = \begin{cases} \sum_{i=0}^{p_2-k} \left[(p_2 + 1 - k - i) \cdot \bar{\mathbf{A}}_{p_2}[i] (\bar{\mathbf{P}}_{p_2}^A)^{-1} \bar{\mathbf{A}}_{p_2}^H[k+i] \right. \\ \quad - i \cdot \bar{\mathbf{B}}_{p_2}[k+i] (\bar{\mathbf{P}}_{p_2}^B)^{-1} \bar{\mathbf{B}}_{p_2}^H[i] \\ \quad + (p_2 - k - i) \cdot \bar{\mathbf{C}}_{p_2}[i] (\bar{\mathbf{P}}_{p_2}^C)^{-1} \bar{\mathbf{C}}_{p_2}^H[k+i] \\ \quad \left. - (p_2 - k - i) \cdot \bar{\mathbf{D}}_{p_2}[i] (\bar{\mathbf{P}}_{p_2}^D)^{-1} \bar{\mathbf{D}}_{p_2}^H[k+i] \right] \text{ for } 0 \leq k \leq p_2 \\ \hat{\Psi}^H[-k] \text{ for } -p_2 \leq k \leq 0 \end{cases}$$

where $\bar{\mathbf{A}}_{p_2}[0] = \bar{\mathbf{B}}_{p_2}[0] = \mathbf{I}$, by definition. If we now define the elements of the $\hat{\Psi}$ matrix as

$$\hat{\Psi}[\mathbf{k}] = \begin{pmatrix} \hat{\Psi}_k[0,0] & \cdots & \hat{\Psi}_k[0,p_1] \\ \vdots & \ddots & \vdots \\ \hat{\Psi}_k[p_1,0] & \cdots & \hat{\Psi}_k[p_1,p_1] \end{pmatrix} \quad (6.35)$$

and the $\hat{\alpha}$ terms as sums along diagonals of the $\hat{\Psi}$ matrix for $0 \leq k \leq p_2$

$$\hat{\alpha}[m, k] = \begin{cases} \sum_{n=0}^{p_1-m} \hat{\Psi}_k[n, n+m], \text{ for } 0 \leq m \leq p_1 \\ \sum_{n=0}^{p_1+m} \hat{\Psi}_k[n-m, n], \text{ for } -p_1 \leq m < 0, \end{cases} \quad (6.36)$$

then Eq. 6.34 can be alternatively expressed as

$$\hat{P}_{2\text{DMV-cov}}(f_1, f_2) = \frac{T_1 T_2}{\sum_{m=-p_1}^{p_1} \sum_{k=-p_2}^{p_2} \hat{\alpha}[m, k] e^{-j2\pi[f_1 m T_1 + f_2 k T_2]}} \cdot \quad (6.37)$$

Note that the symmetry property $\hat{\alpha}[m, -k] = \hat{\alpha}[-m, k]$ has been used in Eq. 6.37. The 2-D parameter $\hat{\alpha}$ is obtained from the 2-D forward and backward AR filter parameters $\bar{\mathbf{A}}$ and $\bar{\mathbf{B}}$. It can be observed that the structure of the denominator of Eq. 6.37 can be computed using the 2-D FFT of $\hat{\alpha}[m, k]$ over the interval $(-1/2T_1 \leq f_1 \leq 1/2T_1, -1/2T_2 \leq f_2 \leq 1/2T_2)$ in Hz or meters/cycle. The fast computational algorithm requires computational complexity proportional to p^5 and memory storage proportional to p^3 . This is more efficient than direct evaluation of the original 2-D LS-MVSE defined in Eq. 5.21, which requires computational complexity proportional to p^6 and memory storage proportional to p^4 . The fast algorithm of 2-D LS-MVSE is able to save all intermediate order parameters when it recursively calculates the parameters from order 1 to p_2 . By solving and saving all intermediate order parameter values, it allows us to search for the optimal order fit to the data samples. The order selection process does not cost any extra computation of the set of required parameters. The PSD estimate in Eq. 6.37 in Q_1 is the same as those in Q_2 , Q_3 and Q_4 as well, since the special AR parameter vectors $\bar{\mathbf{a}}$ and $\bar{\mathbf{b}}$, and the auxiliary factor vectors $\bar{\mathbf{c}}$ and $\bar{\mathbf{d}}$, do not depend on the selected quadrant. Therefore, the computation of the 2-D least-squares-based minimum variance spectral estimate based on $\hat{\mathbf{R}}_{p_2}^{-1}$ does not have to reprocess the data range into four quadrants, which reduces the overall computational complexity, compared with 2-D AR spectral estimators that depend upon quadrant selection.

6.2.2. Computation and Storage Counts

The computation and storage count is summarized in the Table 6.2. The new algorithm requires a number of multiply operations and a number of add operations proportional to p^5 in order to calculate the set of $\hat{\Psi}[k]$, $0 \leq k \leq p_2$, coefficients. A 2-D FFT in Eq. 6.37 is then used to evaluate the denominator of the LS-based MVSE over a range of frequencies ($-1/2T_1 \leq f_1 \leq 1/2T_1$, $-1/2T_2 \leq f_2 \leq 1/2T_2$) in Hz or meters/cycle. It only requires memory storage proportional to p^3 to save all of the parameters. This significantly reduces the computational complexity and memory storage requirements, compared with the direct evaluation method Eq. 5.21, whose computational complexity and memory storage requirements are proportional to p^6 and p^5 , respectively.

6.3. Least-Squares-Based 2-D Minimum Variance Spectral Estimation: Modified Covariance Case

6.3.1. Development of Fast Computational Solution

In this section, we show the development of the inverse of the *near-to-Toeplitz* data product matrix, $\hat{\underline{\mathbf{R}}}_p^{-1}$ in Eq. 5.31.

Inspired by Eq. 6.1 and Eq. 6.2, the decomposition of the inverse 2-D *near-to-doubly-Toeplitz* data product matrix $\hat{\underline{\mathbf{R}}}_{p_2}^{-1}$ is based on the solution of the Yule-Walker normal equations of order p_2

$$\hat{\underline{\mathbf{R}}}_{p_2} \begin{pmatrix} \mathbf{I} \\ \tilde{\underline{\mathbf{a}}}_{p_2} \end{pmatrix} = \begin{pmatrix} \tilde{\underline{\mathbf{P}}}_{p_2}^A \\ \mathbf{0} \end{pmatrix} \quad (6.38)$$

2-D LS-based MVSE (Covariance Case)		
$(p_1 = p_2 = p, N_1 = N_2 = N, N_{f1} = N_{f2} = N_f)$		
	Fast Solution	Direct Method
Computational Complexity	\times $\begin{aligned} & \frac{17}{2}p^5 - (\frac{3}{2}N - \frac{87}{2})p^4 + (2N^2 + \frac{N}{2} + \frac{181}{2})p^3 \\ & - (3N^3 + N^2 - \frac{21}{2}N - \frac{207}{2})p^2 \\ & + (2N^4 - N^3 - N^2 + \frac{33}{2}N + 65)p \\ & + (2N^4 + 4N^3 + 2N^2 + 8N) \\ & + 2N_f \log_2(N_f) \end{aligned}$	$\begin{aligned} & p^6 - (2N - 4)p^5 + (N^2 - 8N + 2N_f^2 + \frac{23}{3})p^4 \\ & + (4N^2 - 12N + 8N_f^2 + \frac{29}{3})p^3 \\ & + (6N^2 - 8N + 12N_f^2 + \frac{26}{3})p^2 \\ & + (4N^2 - 2N + 8N_f^2 + \frac{20}{3})p \\ & + (N^2 + 2N_f^2) \end{aligned}$
	$+$ $\begin{aligned} & 9p^5 - (3N - 40)p^4 \\ & + (2N^2 - 12N + 61)p^3 \\ & + (8N^2 - 37N - 44)p^2 \\ & - (N^3 - 22N^2 + 17N - 10)p \\ & + (2N^4 - 2N^3 + 7N^2 - N) \\ & + 2N_f \log_2(N_f) \end{aligned}$	$\begin{aligned} & \frac{5}{3}p^6 - (N^2 - 2N + 1)p^5 \\ & - (7N^2 - 14N - 2N_f^2 - 9)p^4 \\ & - (8N^2 - 16N - 4N_f^2 - \frac{28}{3})p^3 \\ & - (2N^2 - 40N - 2N_f^2 - \frac{28}{3})p^2 \\ & + (2N^2 - 2N + \frac{14}{3})p \\ & + (N^2 - 2N) \end{aligned}$
Storage	$\begin{aligned} & 2p^3 + (4N + 24)p^2 \\ & + (4N^2 - 5N + 39)p \\ & + (12N^2 + 5N + N_f^2) \end{aligned}$	$\begin{aligned} & 2p^4 - (2N - 6)p^3 \\ & + (N^2 - 4N + 7)p^2 \\ & + (2N^2 - 2N + 4)p + (N^2 + N_f^2) \end{aligned}$

TABLE 6.2. Comparison of the Computation and Storage Counts for 2-D Covariance LS-Based MVSE. Note: p_1, p_2 are the orders of the estimator in 2-D directions, N_1, N_2 are the size of 2-D data sequence, N_{f1}, N_{f2} are the numbers of 2-D FFT frequency bins, \times is the number of complex multiplications, and $+$ is the number of complex additions. Note that the maximum 2-D order p_{max} must satisfy $p_{max} < (N - 1)/2$ for $\hat{\mathbf{R}}_p^{-1}$ exist.

and

$$\hat{\underline{\mathbf{R}}}_{p_2} \begin{pmatrix} \mathbf{J} \tilde{\mathbf{a}}_{p_2}^* \mathbf{J} \\ \mathbf{I} \end{pmatrix} = \begin{pmatrix} \mathbf{0} \\ \mathbf{J}(\tilde{\mathbf{P}}_{p_2}^A)^* \mathbf{J} \end{pmatrix} \quad (6.39)$$

where the new special AR vectors of dimension $(p_1 + 1) \times (p_1 + 1)(p_2 + 1)$ are

$$\tilde{\mathbf{a}}_{p_2}^T = \left(\tilde{\mathbf{A}}_{p_2}^T[1], \dots, \tilde{\mathbf{A}}_{p_2}^T[p_2] \right) \quad (6.40)$$

and

$$(\mathbf{J} \tilde{\mathbf{a}}_{p_2}^* \mathbf{J})^T = \left((\mathbf{J} \tilde{\mathbf{A}}_{p_2}^*[1] \mathbf{J})^T, \dots, (\mathbf{J} \tilde{\mathbf{A}}_{p_2}^*[p_2] \mathbf{J})^T \right), \quad (6.41)$$

where $\tilde{\mathbf{A}}_{p_2}[k]$, $0 \leq k \leq p_2$, are $(p_1 + 1) \times (p_1 + 1)$ matrices and $\tilde{\mathbf{A}}_{p_2}[0] = \mathbf{I}$ by definition. The solutions of the Yule-Walker normal equations have been performed by Marple in [20]. $\tilde{\mathbf{P}}_{p_2}^A$ is a positive definite square hermitian matrix of dimension $(p_1 + 1) \times (p_1 + 1)$. The $(p_1 + 1)(p_2 + 1) \times (p_1 + 1)(p_2 + 1)$ -dimensional $\hat{\underline{\mathbf{R}}}_{p_2}$ is defined in Eq. 5.31. $\hat{\underline{\mathbf{R}}}_{p_2}$ is not Toeplitz, but it is centrosymmetric and hermitian

$$\hat{\underline{\mathbf{R}}}_{p_2} = \mathbf{J} \hat{\underline{\mathbf{R}}}_{p_2}^* \mathbf{J}, \quad \hat{\underline{\mathbf{R}}}_{p_2} = \hat{\underline{\mathbf{R}}}_{p_2}^H.$$

Based on Eq. 5.31, the crucial to the structure of the inverse *near-to-doubly-Toeplitz* data product matrix is the following order-index partitions of the $(p_1 + 1)(p_2 + 1) \times (p_1 + 1)(p_2 + 1)$ dimensional matrix $\hat{\underline{\mathbf{R}}}_{p_2}$

$$\hat{\underline{\mathbf{R}}}_{p_2} = \begin{pmatrix} \hat{\underline{\mathbf{R}}}_{p_2-1}' & \hat{\underline{\mathbf{r}}}_{p_2} \\ \hat{\underline{\mathbf{r}}}_{p_2}^H & \hat{\underline{\mathbf{R}}}_{p_2}[p_2, p_2] \end{pmatrix} \quad (6.42)$$

and

$$\hat{\underline{\mathbf{R}}}_{p_2} = \begin{pmatrix} \hat{\underline{\mathbf{R}}}_{p_2}[0, 0] & \mathbf{J} \hat{\underline{\mathbf{r}}}_{p_2}^T \mathbf{J} \\ \mathbf{J} \hat{\underline{\mathbf{r}}}_{p_2}^* \mathbf{J} & \mathbf{J} \hat{\underline{\mathbf{R}}}_{p_2-1}'^* \mathbf{J} \end{pmatrix} \quad (6.43)$$

in which the $(p_1 + 1)(p_2 + 1) \times (p_1 + 1)$ block vectors are defined as

$$\begin{aligned}\hat{\underline{\mathbf{r}}}_{p_2}^H &= \left(\hat{\underline{\mathbf{R}}}_{p_2}^H[0, p_2], \dots, \hat{\underline{\mathbf{R}}}_{p_2}^H[p_2 - 1, p_2] \right), \\ \mathbf{J} \hat{\underline{\mathbf{r}}}_{p_2}^T \mathbf{J} &= \left(\mathbf{J} \hat{\underline{\mathbf{R}}}_{p_2}^T[1, 0] \mathbf{J}, \dots, \mathbf{J} \hat{\underline{\mathbf{R}}}_{p_2}^T[p_2, 0] \mathbf{J} \right).\end{aligned}$$

Also crucial are the following time-index partitions,

$$\begin{aligned}\hat{\underline{\mathbf{R}}}_{p_2}' &= \sum_{m=p_2+2}^{N_2} (\underline{\mathbf{x}}_{p_2}^H[m] \underline{\mathbf{x}}_{p_2}[m] + \mathbf{J} \underline{\mathbf{x}}_{p_2}^T[m] \underline{\mathbf{x}}_{p_2}^*[m] \mathbf{J}) \\ &= \hat{\underline{\mathbf{R}}}_{p_2} - \underline{\mathbf{g}}_{p_2}^H[m+1] \underline{\mathbf{g}}_{p_2}^*[m+1]\end{aligned}\tag{6.44}$$

or

$$\mathbf{J} \hat{\underline{\mathbf{R}}}_{p_2}' \mathbf{J} = \mathbf{J} \hat{\underline{\mathbf{R}}}_{p_2} \mathbf{J} - \mathbf{J} \underline{\mathbf{g}}_{p_2}^T[p_2 + 1] \underline{\mathbf{g}}_{p_2}^*[p_2 + 1] \mathbf{J}\tag{6.45}$$

where the $(N_1 - p_1) \times (p_1 + 1)(p_2 + 1)$ -dimensional data column block vector $\underline{\mathbf{x}}_{p_2}[m]$ is defined in Eq. 6.18. The alternative $2(N_1 - p_1) \times (p_1 + 1)(p_2 + 1)$ -dimensional data matrix is

$$\underline{\mathbf{g}}_{p_2}[p_2] = \begin{pmatrix} \mathbf{x}[p_2] \\ \mathbf{J} \mathbf{x}^*[N_2] \end{pmatrix}.$$

The pair of auxiliary $(p_1 + 1)(p_2 + 1) \times (N_1 - p_1)$ -dimensional block vectors $\underline{\mathbf{c}}_{p_2}^T = (\tilde{\mathbf{C}}_{p_2}^T[0], \dots, \tilde{\mathbf{C}}_{p_2}^T[p_2])$ and $\underline{\mathbf{d}}_{p_2}^T = (\tilde{\mathbf{D}}_{p_2}^T[0], \dots, \tilde{\mathbf{D}}_{p_2}^T[p_2])$ are also critical to the fast algorithm. They are defined by

$$\hat{\underline{\mathbf{R}}}_{p_2} \underline{\mathbf{c}}_{p_2} = \mathbf{J} \underline{\mathbf{x}}_{p_2}[N_2], \quad \hat{\underline{\mathbf{R}}}_{p_2}^* \mathbf{J} \underline{\mathbf{c}}_{p_2} = \underline{\mathbf{x}}_{p_2}[N_2],\tag{6.46}$$

and

$$\hat{\underline{\mathbf{R}}}_{p_2} \underline{\mathbf{d}}_{p_2} = \underline{\mathbf{x}}_{p_2}^*[p_2 + 1], \quad \hat{\underline{\mathbf{R}}}_{p_2}^* \mathbf{J} \underline{\mathbf{d}}_{p_2} = \mathbf{J} \underline{\mathbf{x}}_{p_2}^*[p_2 + 1].\tag{6.47}$$

To simplify the derivation, a new $(p_1 + 1)(p_2 + 1) \times 2(N_1 - p_1)$ -dimensional column block vector is defined as

$$\underline{\mathbf{s}}_{p_2} = (\underline{\mathbf{d}}_{p_2}, \underline{\mathbf{c}}_{p_2})\tag{6.48}$$

where the auxiliary block vector $\tilde{\mathbf{s}}_{p_2}^T = (\tilde{\mathbf{S}}_{p_2}^T[0], \dots, \tilde{\mathbf{S}}_{p_2}^T[p_2])$ has block elements $\tilde{\mathbf{S}}_{p_2}[m] = (\tilde{\mathbf{D}}_{p_2}[m], \tilde{\mathbf{C}}_{p_2}[m])$, for $0 \leq m \leq p_2$, of dimension $(p_1 + 1) \times 2(N_1 - p_1)$. Based on Eq. 6.45, Eq. 6.46 and Eq. 6.47, we can infer the following relationship

$$\hat{\mathbf{R}}_{p_2} \tilde{\mathbf{s}}_{p_2} = \tilde{\mathbf{g}}_{p_2}^H, \quad \hat{\mathbf{R}}_{p_2}^* \mathbf{J} \tilde{\mathbf{s}}_{p_2} = \mathbf{J} \tilde{\mathbf{g}}_{p_2}^H \quad (6.49)$$

Substituting the submatrix partitions Eq. 6.42 and Eq. 6.43 into the left sides of the Yule-Walker normal equations Eq. 6.39 and Eq. 6.38 yields, respectively,

$$\begin{pmatrix} \hat{\mathbf{R}}_{p_2-1}' & \hat{\mathbf{r}}_{p_2} \\ \hat{\mathbf{r}}_{p_2}^H & \hat{\mathbf{R}}_{p_2}[p_2, p_2] \end{pmatrix} \begin{pmatrix} \mathbf{J} \tilde{\mathbf{A}}_{p_2}^*[p_2 + 1] \mathbf{J} \\ \vdots \\ \mathbf{J} \tilde{\mathbf{A}}_{p_2}^*[1] \mathbf{J} \\ \mathbf{I} \end{pmatrix} = \begin{pmatrix} \mathbf{0} \\ \vdots \\ \mathbf{0} \\ \mathbf{J}(\tilde{\mathbf{P}}_{p_2}^A)^* \mathbf{J} \end{pmatrix} \quad (6.50)$$

$$\begin{pmatrix} \hat{\mathbf{R}}_{p_2}[0, 0] & \mathbf{J} \hat{\mathbf{r}}_{p_2}^T \mathbf{J} \\ \mathbf{J} \hat{\mathbf{r}}_{p_2}^* \mathbf{J} & \mathbf{J}(\hat{\mathbf{R}}_{p_2-1}')^* \mathbf{J} \end{pmatrix} \begin{pmatrix} \mathbf{I} \\ \tilde{\mathbf{A}}_{p_2}[1] \\ \vdots \\ \tilde{\mathbf{A}}_{p_2}[p_2 + 1] \end{pmatrix} = \begin{pmatrix} \tilde{\mathbf{P}}_{p_2}^A \\ \mathbf{0} \\ \vdots \\ \mathbf{0} \end{pmatrix}. \quad (6.51)$$

The following relations can be derived from Eq. 6.50 and Eq. 6.24

$$\hat{\mathbf{r}}_{p_2} = -\hat{\mathbf{R}}_{p_2-1} \mathbf{J} \tilde{\mathbf{a}}_{p_2}^* \mathbf{J}, \quad \hat{\mathbf{r}}_{p_2}^H \mathbf{J} \tilde{\mathbf{a}}_{p_2}^* \mathbf{J} + \hat{\mathbf{R}}_{p_2}[p_2, p_2] = \mathbf{J}(\tilde{\mathbf{P}}_{p_2}^A)^* \mathbf{J} \quad (6.52)$$

and

$$\hat{\mathbf{r}}_{p_2}^* = -(\hat{\mathbf{R}}_{p_2-1}')^* \mathbf{J} \tilde{\mathbf{a}}_{p_2} \mathbf{J}, \quad \mathbf{J} \hat{\mathbf{r}}_{p_2}^T \mathbf{J} \tilde{\mathbf{a}}_{p_2} + \hat{\mathbf{R}}_{p_2}[0, 0] = \tilde{\mathbf{P}}_{p_2}^A. \quad (6.53)$$

Analogous to the partitioned matrix inversion lemma and the specialized form of the augmented matrix inversion lemma in [15], the inverse matrix of Eq. 6.42 can

be expressed as

$$\hat{\underline{\mathbf{R}}}_{p_2}^{-1} = \begin{pmatrix} (\hat{\underline{\mathbf{R}}}_{p_2-1})^{-1} + (\hat{\underline{\mathbf{R}}}_{p_2-1})^{-1} \hat{\underline{\mathbf{r}}}_{p_2} \Delta_{p_2}^{-1} \hat{\underline{\mathbf{r}}}_{p_2}^H (\hat{\underline{\mathbf{R}}}_{p_2-1})^{-1}, & -(\hat{\underline{\mathbf{R}}}_{p_2-1})^{-1} \hat{\underline{\mathbf{r}}}_{p_2} \Delta_{p_2}^{-1} \\ -\Delta_{p_2}^{-1} \hat{\underline{\mathbf{r}}}_{p_2}^H (\hat{\underline{\mathbf{R}}}_{p_2-1})^{-1}, & \Delta_{p_2}^{-1} \end{pmatrix} \quad (6.54)$$

in which

$$\begin{aligned} \Delta_{p_2} &= \hat{\underline{\mathbf{R}}}_{p_2}[p_2, p_2] - \hat{\underline{\mathbf{r}}}_{p_2}^H (\hat{\underline{\mathbf{R}}}_{p_2-1})^{-1} \hat{\underline{\mathbf{r}}}_{p_2} \\ &= \hat{\underline{\mathbf{R}}}_{p_2}[p_2, p_2] + \hat{\underline{\mathbf{r}}}_{p_2}^H \mathbf{J} \hat{\underline{\mathbf{a}}}_{p_2}^T \mathbf{J} = \mathbf{J}(\tilde{\mathbf{P}}_{p_2}^{A*}) \mathbf{J}, \end{aligned} \quad (6.55)$$

so that $\Delta_{p_2}^{-1} = (\tilde{\mathbf{P}}_{p_2}^{A*})^{-1}$. Substituting Eq. 6.56, Eq. 6.52 and Eq. 6.49 into Eq. 6.54, $\hat{\underline{\mathbf{R}}}_{p_2}^{-1}$ can then be rewritten as

$$\begin{aligned} \hat{\underline{\mathbf{R}}}_{p_2}^{-1} &= \begin{pmatrix} (\hat{\underline{\mathbf{R}}}_{p_2-1})^{-1} + (\mathbf{J} \hat{\underline{\mathbf{a}}}_{p_2}^* \mathbf{J}) \mathbf{J} (\tilde{\mathbf{P}}_{p_2}^{A*})^{-1} \mathbf{J} (\mathbf{J} \hat{\underline{\mathbf{a}}}_{p_2}^T \mathbf{J}), & (\mathbf{J} \hat{\underline{\mathbf{a}}}_{p_2}^* \mathbf{J}) \mathbf{J} (\tilde{\mathbf{P}}_{p_2}^{A*})^{-1} \mathbf{J} \\ \mathbf{J} (\tilde{\mathbf{P}}_{p_2}^{A*})^{-1} \mathbf{J} (\mathbf{J} \hat{\underline{\mathbf{a}}}_{p_2}^T \mathbf{J}), & \mathbf{J} (\tilde{\mathbf{P}}_{p_2}^{A*})^{-1} \mathbf{J} \end{pmatrix} \\ &= \begin{pmatrix} (\hat{\underline{\mathbf{R}}}_{p_2-1})^{-1} + \tilde{\underline{\mathbf{s}}}_{p_2-1} \tilde{\Phi}_{p_2-1}^{-1} \tilde{\underline{\mathbf{s}}}_{p_2-1}^H + \mathbf{J} \tilde{\underline{\mathbf{a}}}_{p_2}^* (\tilde{\mathbf{P}}_{p_2}^{A*})^{-1} \tilde{\underline{\mathbf{a}}}_{p_2}^T \mathbf{J}, & \mathbf{J} \tilde{\underline{\mathbf{a}}}_{p_2}^* (\tilde{\mathbf{P}}_{p_2}^{A*})^{-1} \mathbf{J} \\ \mathbf{J} (\tilde{\mathbf{P}}_{p_2}^{A*})^{-1} \tilde{\underline{\mathbf{a}}}_{p_2}^T \mathbf{J}, & \mathbf{J} (\tilde{\mathbf{P}}_{p_2}^{A*})^{-1} \mathbf{J} \end{pmatrix} \end{aligned} \quad (6.56)$$

Alternatively, the inverse matrix Eq. 6.43 can be expressed as

$$\hat{\underline{\mathbf{R}}}_{p_2}^{-1} = \begin{pmatrix} (\tilde{\mathbf{P}}_{p_2}^A)^{-1}, & (\tilde{\mathbf{P}}_{p_2}^A)^{-1} \tilde{\underline{\mathbf{a}}}_{p_2}^H \\ \tilde{\underline{\mathbf{a}}}_{p_2} (\tilde{\mathbf{P}}_{p_2}^A)^{-1}, & \hat{\underline{\mathbf{R}}}_{p_2-1}^{-1} + \mathbf{J} \tilde{\underline{\mathbf{s}}}_{p_2-1} (\tilde{\Phi}_{p_2-1}^*)^{-1} \tilde{\underline{\mathbf{s}}}_{p_2-1}^T \mathbf{J} + \tilde{\underline{\mathbf{a}}}_{p_2} (\tilde{\mathbf{P}}_{p_2}^A)^{-1} \tilde{\underline{\mathbf{a}}}_{p_2}^H \end{pmatrix} \quad (6.57)$$

Assume $\tilde{\mathbf{u}}_{p_2}[j, k]$ for $0 \leq j, k \leq p_2$ is a $(p_1 + 1) \times (p_1 + 1)$ block element of $\hat{\mathbf{R}}_{p_2}^{-1}$

$$\hat{\mathbf{R}}_{p_2}^{-1} = \begin{pmatrix} \tilde{\mathbf{u}}_{p_2}[0, 0] & \tilde{\mathbf{u}}_{p_2}[0, 1] & \cdots & \tilde{\mathbf{u}}_{p_2}[0, p_2] \\ \tilde{\mathbf{u}}_{p_2}[1, 0] & \tilde{\mathbf{u}}_{p_2}[1, 1] & \cdots & \tilde{\mathbf{u}}_{p_2}[1, p_2] \\ \vdots & \vdots & \ddots & \vdots \\ \tilde{\mathbf{u}}_{p_2}[p_2, 0] & \tilde{\mathbf{u}}_{p_2}[p_2, 1] & \cdots & \tilde{\mathbf{u}}_{p_2}[p_2, p_2] \end{pmatrix} \quad (6.58)$$

of $(p_1 + 1)(p_2 + 1) \times (p_1 + 1)(p_2 + 1)$ dimension. From above, the following relations may be found

$$\begin{aligned} \tilde{\mathbf{u}}_{p_2}[0, 0] &= (\tilde{\mathbf{P}}_{p_2}^A)^{-1}, & \tilde{\mathbf{u}}_{p_2}[p_2, p_2] &= \mathbf{J}(\tilde{\mathbf{P}}_{p_2}^{A*})^{-1}\mathbf{J}, \\ \tilde{\mathbf{u}}_{p_2}[j, 0] &= \tilde{\mathbf{A}}_{p_2}[j](\tilde{\mathbf{P}}_{p_2}^A)^{-1}, & \tilde{\mathbf{u}}_{p_2}[0, k] &= (\tilde{\mathbf{P}}_{p_2}^A)^{-1}\tilde{\mathbf{A}}_{p_2}^H[k], \\ \tilde{\mathbf{u}}_{p_2}[p_2, p_2 - k] &= \mathbf{J}(\tilde{\mathbf{P}}_{p_2}^{A*})^{-1}\tilde{\mathbf{A}}_{p_2}^T[k]\mathbf{J}, & \tilde{\mathbf{u}}_{p_2}[p_2 - j, p_2] &= \mathbf{J}\tilde{\mathbf{A}}_{p_2}^*[j](\tilde{\mathbf{P}}_{p_2}^{A*})^{-1}\mathbf{J} \end{aligned}$$

for $1 \leq j, k \leq p_2$, and

$$\begin{aligned} \tilde{\mathbf{u}}_{p_2}[j, k] &= \tilde{\mathbf{u}}_{p_2-1}[j, k] + \tilde{\mathbf{S}}_{p_2-1}[j]\tilde{\mathbf{\Phi}}_{p_2-1}^{-1}\tilde{\mathbf{S}}_{p_2-1}^H[k] \\ &\quad + \mathbf{J}\tilde{\mathbf{A}}_{p_2}^*[p_2 - j](\tilde{\mathbf{P}}_{p_2}^A)^{-1}\tilde{\mathbf{A}}_{p_2}^T[p_2 - k]\mathbf{J}, \end{aligned}$$

$$\begin{aligned} \tilde{\mathbf{u}}_{p_2}[j + 1, k + 1] &= \tilde{\mathbf{u}}_{p_2-1}[j, k] + \mathbf{J}\tilde{\mathbf{S}}_{p_2-1}^*[p_2 - j](\tilde{\mathbf{\Phi}}_{p_2-1}^*)^{-1}\tilde{\mathbf{S}}_{p_2-1}^T[p_2 - k]\mathbf{J} \\ &\quad + \tilde{\mathbf{A}}_{p_2}[j + 1](\tilde{\mathbf{P}}_{p_2}^A)^{-1}\tilde{\mathbf{A}}_{p_2}^H[k + 1], \end{aligned}$$

for $0 \leq j, k \leq p_2 - 1$. Combining the last two equations allows us to eliminate $\tilde{\mathbf{u}}_{p_2}[j, k]$, yielding

$$\begin{aligned} \tilde{\mathbf{u}}_{p_2}[j + 1, k + 1] &= \tilde{\mathbf{u}}_{p_2}[j, k] + \tilde{\mathbf{A}}_{p_2}[j + 1](\tilde{\mathbf{P}}_{p_2}^A)^{-1}\tilde{\mathbf{A}}_{p_2}^H[k + 1] \\ &\quad - \mathbf{J}\tilde{\mathbf{A}}_{p_2}^*[p_2 - j](\tilde{\mathbf{P}}_{p_2}^{A*})^{-1}\tilde{\mathbf{A}}_{p_2}^T[p_2 - k]\mathbf{J} - \tilde{\mathbf{S}}_{p_2-1}[j]\tilde{\mathbf{\Phi}}_{p_2-1}^{-1}\tilde{\mathbf{S}}_{p_2-1}^H[k] \\ &\quad + \mathbf{J}\tilde{\mathbf{S}}_{p_2-1}^*[p_2 - j](\tilde{\mathbf{\Phi}}_{p_2-1}^*)^{-1}\tilde{\mathbf{S}}_{p_2-1}^T[p_2 - k]\mathbf{J}. \end{aligned} \quad (6.59)$$

Eq. 6.59 is a recursive relationship that permits all inverse elements to be computed from knowledge of only the $\tilde{\mathbf{A}}$ vectors. The following inverse matrix relationship may be developed from Eq. 6.59

$$\begin{aligned} \hat{\underline{\mathbf{R}}}_{p_2}^{-1} = & \underline{\tilde{\mathbf{A}}}_{p_2} (\tilde{\mathbf{P}}_{p_2}^A)^{-1} \underline{\tilde{\mathbf{A}}}_{p_2}^H - \underline{\tilde{\mathbf{B}}}_{p_2} (\tilde{\mathbf{P}}_{p_2}^B)^{-1} \underline{\tilde{\mathbf{B}}}_{p_2}^H \\ & - \underline{\tilde{\mathbf{C}}}_{p_2-1} (\tilde{\mathbf{P}}_{p_2-1}^C)^{-1} \underline{\tilde{\mathbf{C}}}_{p_2-1}^H + \underline{\tilde{\mathbf{D}}}_{p_2-1} (\tilde{\mathbf{P}}_{p_2-1}^D)^{-1} \underline{\tilde{\mathbf{D}}}_{p_2-1}^H \end{aligned} \quad (6.60)$$

in which the $(p_1 + 1)(p_2 + 1) \times (p_1 + 1)(p_2 + 1)$ triangular Toeplitz matrices

$$\begin{aligned} \underline{\tilde{\mathbf{A}}}_{p_2} &= \begin{pmatrix} \mathbf{I} & \mathbf{0} & \cdots & \mathbf{0} \\ \tilde{\mathbf{A}}_{p_2}[1] & \ddots & \ddots & \vdots \\ \vdots & \ddots & \ddots & \mathbf{0} \\ \tilde{\mathbf{A}}_{p_2}[p_2] & \cdots & \tilde{\mathbf{A}}_{p_2}[1] & \mathbf{I} \end{pmatrix} \\ \underline{\tilde{\mathbf{B}}}_{p_2} &= \begin{pmatrix} \mathbf{0} & \mathbf{0} & \cdots & \mathbf{0} \\ \mathbf{J} \tilde{\mathbf{A}}_{p_2}^*[p_2] \mathbf{J} & \ddots & \ddots & \vdots \\ \vdots & \ddots & \ddots & \vdots \\ \mathbf{J} \tilde{\mathbf{A}}_{p_2}^*[1] \mathbf{J} & \cdots & \mathbf{J} \tilde{\mathbf{A}}_{p_2}^*[p_2] \mathbf{J} & \mathbf{0} \end{pmatrix} \\ (\underline{\tilde{\mathbf{P}}}_{p_2}^A)^{-1} &= \begin{pmatrix} (\tilde{\mathbf{P}}_{p_2}^A)^{-1} & \cdots & \mathbf{0} \\ \vdots & \ddots & \vdots \\ \mathbf{0} & \cdots & (\tilde{\mathbf{P}}_{p_2}^A)^{-1} \end{pmatrix} \\ (\underline{\tilde{\mathbf{P}}}_{p_2}^B)^{-1} &= \begin{pmatrix} \mathbf{J} (\tilde{\mathbf{P}}_{p_2}^{A*})^{-1} \mathbf{J} & \cdots & \mathbf{0} \\ \vdots & \ddots & \vdots \\ \mathbf{0} & \cdots & \mathbf{J} (\tilde{\mathbf{P}}_{p_2}^{A*})^{-1} \mathbf{J} \end{pmatrix} \end{aligned}$$

where each element is a $(p_1 + 1) \times (p_1 + 1)$ -dimensional matrix. The $(p_1 + 1)(p_2 + 1) \times 2(N_1 - p_1)(p_2 + 1)$ dimensional triangular Toeplitz matrices

$$\underline{\tilde{\mathbf{C}}}_{p_2-1} = \begin{pmatrix} \mathbf{0} & \mathbf{0} & \cdots & \mathbf{0} \\ \tilde{\mathbf{S}}_{p_2-1}[0] & \ddots & \ddots & \mathbf{0} \\ \vdots & \ddots & \ddots & \vdots \\ \tilde{\mathbf{S}}_{p_2-1}[p_2-1] & \cdots & \tilde{\mathbf{S}}_{p_2-1}[0] & \mathbf{0} \end{pmatrix}$$

$$\underline{\tilde{\mathbf{D}}}_{p_2-1} = \begin{pmatrix} \mathbf{0} & \mathbf{0} & \cdots & \mathbf{0} \\ \mathbf{J}\tilde{\mathbf{S}}_{p_2-1}^*[p_2-1]\mathbf{J} & \ddots & \ddots & \mathbf{0} \\ \vdots & \ddots & \ddots & \vdots \\ \mathbf{J}\tilde{\mathbf{S}}_{p_2-1}^*[0]\mathbf{J} & \cdots & \mathbf{J}\tilde{\mathbf{S}}_{p_2-1}^*[p_2-1]\mathbf{J} & \mathbf{0} \end{pmatrix}$$

have block elements that are $(p_1 + 1) \times 2(N_1 - p_1)$ -dimensional matrices. The diagonal matrices

$$(\underline{\tilde{\mathbf{P}}}_{p_2-1}^C)^{-1} = \begin{pmatrix} \tilde{\Phi}_{p_2-1}^{-1} & \cdots & \mathbf{0} \\ \vdots & \ddots & \vdots \\ \mathbf{0} & \cdots & \tilde{\Phi}_{p_2-1}^{-1} \end{pmatrix}$$

$$(\underline{\tilde{\mathbf{P}}}_{p_2-1}^D)^{-1} = \begin{pmatrix} \mathbf{J}(\tilde{\Phi}_{p_2-1}^*)^{-1}\mathbf{J} & \cdots & \mathbf{0} \\ \vdots & \ddots & \vdots \\ \mathbf{0} & \cdots & \mathbf{J}(\tilde{\Phi}_{p_2-1}^*)^{-1}\mathbf{J} \end{pmatrix}$$

are of dimension $2(N_1 - p_1)(p_2 + 1) \times 2(N_1 - p_1)(p_2 + 1)$ with elements of dimension $2(N_1 - p_1) \times 2(N_1 - p_1)$. Based on the substitution of Eq. 6.61 into Eq. 5.30, an alternative 2-D modified covariance LS-MVSE relationship becomes

$$\hat{\hat{P}}_{2\text{DMV-mod}}(f_1, f_2) = \frac{T_1 T_2}{\mathbf{e}_{p_2}^H(f_1) \left(\sum_{k=-p_2}^{p_2} \hat{\hat{\Psi}}[k] e^{-j2\pi f_2 k T_2} \right) \mathbf{e}_{p_2}(f_1)} \quad (6.61)$$

in which the $(p_1 + 1) \times (p_1 + 1)$ -dimension matrix $\hat{\hat{\Psi}}$ of correlated $\tilde{\mathbf{A}}$ elements is defined as

$$\hat{\Psi}[k] = \begin{cases} \sum_{i=0}^{p_2-k} \left[(p_2 + 1 - k - i) \cdot \tilde{\mathbf{A}}_{p_2}[i] (\tilde{\mathbf{P}}_{p_2}^A)^{-1} \tilde{\mathbf{A}}_{p_2}^H[k+i] \right. \\ \quad - i \cdot \mathbf{J} (\tilde{\mathbf{A}}_{p_2}[k+i] (\tilde{\mathbf{P}}_{p_2}^A)^{-1} \tilde{\mathbf{A}}_{p_2}^H[i])^* \mathbf{J} \\ \quad + (p_2 - k - i) \cdot \tilde{\mathbf{S}}_{p_2}[i] \tilde{\Phi}_{p_2-1}^{-1} \tilde{\mathbf{S}}_{p_2}^H[k+i] \\ \quad \left. - (i+1) \cdot \mathbf{J} (\tilde{\mathbf{S}}_{p_2}[k+i] \tilde{\Phi}_{p_2-1}^{-1} \tilde{\mathbf{S}}_{p_2}^H[k])^* \mathbf{J} \right] \text{ for } 0 \leq k \leq p_2 \\ \hat{\Psi}^H[-k] \text{ for } -p_2 \leq k \leq 0 \end{cases}$$

where $\tilde{\mathbf{A}}_{p_2}[0] = \mathbf{I}$, by definition. If we now define the elements of the $\hat{\Psi}$ matrix as

$$\hat{\Psi}[k] = \begin{pmatrix} \hat{\Psi}_k[0,0] & \cdots & \hat{\Psi}_k[0,p_1] \\ \vdots & \ddots & \vdots \\ \hat{\Psi}_k[p_1,0] & \cdots & \hat{\Psi}_k[p_1,p_1] \end{pmatrix} \quad (6.62)$$

and the 2-D $\hat{\alpha}$ scalars as sums along diagonals of the $\hat{\Psi}$ matrix for $0 \leq k \leq p_2$

$$\hat{\alpha}[m, k] = \begin{cases} \sum_{n=0}^{p_1-m} \hat{\Psi}_k[n, n+m], & \text{for } 0 \leq m \leq p_1 \\ \sum_{n=0}^{p_1+m} \hat{\Psi}_k[n-m, n], & \text{for } -p_1 \leq m < 0, \end{cases} \quad (6.63)$$

then Eq. 6.61 can be reformulated as

$$\tilde{P}_{2\text{DMV-mod}}(f_1, f_2) = \frac{T_1 T_2}{\sum_{m=-p_1}^{p_1} \sum_{k=-p_2}^{p_2} \hat{\alpha}[m, k] e^{-j2\pi[f_1 m T_1 + f_2 k T_2]}}. \quad (6.64)$$

Note that the symmetry property $\hat{\alpha}[m, -k] = \hat{\alpha}[-m, k]$ has been used in Eq. 6.37. The weighted correlation-like result $\hat{\alpha}$ is obtained from the 2-D forward and backward FIR filter parameters $\tilde{\mathbf{A}}$. It can be observed that the structure of the denominator of Eq. 6.64 can be computed using the 2-D FFT over the interval $(-1/2T_1 \leq f_1 \leq 1/2T_1, -1/2T_2 \leq f_2 \leq 1/2T_2)$ in Hz or meters/cycle. For the same reason as the 2-D covariance LS-based MVSE, the 2-D modified covariance LS-based MVSE estimator in Eq. 6.64 in Q_1 is numerically identical to the results

in quadrants Q_2 , Q_3 and Q_4 , which saves computations as there is no need to compute the other three quadrants.

6.3.2. Computation and Storage Counts

The computation and storage count is summarized in the Table 6.3. The new algorithm requires a number of multiply operations and a number of add operations proportional to p^5 in order to calculate the set of $\hat{\Psi}[k]$, $0 \leq k \leq p_2$, coefficients. An 2-D FFT in Eq. 6.64 is then used to evaluate the denominator of the LS-based MVSE over a range of frequencies ($-1/2T_1 \leq f_1 \leq 1/2T_1$, $-1/2T_2 \leq f_2 \leq 1/2T_2$) in Hz or meters/cycle. It only requires memory storage proportional to p^3 to save all of the parameters. This significantly reduces computational complexity and memory storage requirements, compared with the direct evaluation method Eq. 5.30 whose computational complexity and memory location are proportional to p^6 and p^5 , respectively.

2-D LS-based MVSE (Modified Covariance Case)		
$(p_1 = p_2 = p, N_1 = N_2 = N, N_{f1} = N_{f2} = N_f)$		
	Fast Solution	Direct Method
Computational Complexity	$-\frac{5}{2}p^5 - (10N - \frac{53}{2})p^4$ $+(\frac{5}{2}N^2 + \frac{3}{2} + \frac{135}{2})p^3$ $-(14N^3 + N^2 - \frac{45}{2}N - \frac{235}{2})p^2$ $+(3N^4 - 2N^3 - N^2 + \frac{29}{2}N + 89)p$ $+(3N^4 + N^3 + 5N^2)$ $+2N_f \log_2(N_f)$	$\frac{8}{3}p^6 - (4N - 12)p^5$ $+(2N^2 - 16N + 2N_f^2 + \frac{71}{3})p^4$ $+(8N^2 - 24N + 8N_f^2 + 28)p^3$ $+(12N^2 - 16N + 12N_f^2 + \frac{65}{3})p^2$ $+(8N^2 - 4N + 8N_f^2 + 10)p$ $+(2N^2 + 2N_f^2)$
	$-2p^5 - (10N - 40)p^4$ $+(12N^2 - 15N + \frac{59}{2})p^3$ $+(10N^2 - \frac{37}{3}N - 47)p^2$ $-(N^3 - 15N^2 + 10N - 44)p$ $+(5N^4 - N^3 + 11N^2 - N)$ $+2N_f \log_2(N_f)$	$\frac{8}{3}p^6 - (4N^2 - 8N - 8)p^5$ $-(14N^2 - 28N - 2N_f^2 - 8)p^4$ $-(16N^2 - 32N - 4N_f^2 - \frac{16}{3})p^3$ $-(4N^2 - 8N - 2N_f^2 - \frac{22}{3})p^2$ $+(4N^2 - 8N - \frac{8}{3})p + (2N^2 - 4N)$
Storage	$4p^3 + (7N + 30)p^2$ $+(4N^2 - 3N + 54)p$ $+(14N^2 + 9N + N_f^2)$	$3p^4 - (2N - 10)p^3$ $+(N^2 - 4N + 14)p^2$ $+(2N^2 - 2N + 10)p + (N^2 + N_f^2)$

TABLE 6.3. Comparison of the Computation and Storage Counts for 2-D Modified Covariance LS-Based MVSE. Note: p_1, p_2 are the orders of the estimator in 2-D directions, N_1, N_2 are the size of 2-D data sequence, N_{f1}, N_{f2} are the numbers of 2-D FFT frequency bins, \times is the number of complex multiplications, and $+$ is the number of complex additions. Note that the maximum 2-D order p_{max} must satisfy $p_{max} < (2N - 1)/3$ for $\hat{\underline{\mathbf{R}}}_p^{-1}$ exist.

7. IMPROVED-FEATURE DETAIL USING FAST ALGORITHMS FOR TWO-DIMENSIONAL MINIMUM VARIANCE SPECTRAL ESTIMATION

Experimental results from three different 2-D data sets are used to evaluate the performance of the two new fast computational solutions for 2-D LS-based MVSE in the covariance and the modified covariance cases in this chapter. A narrow-band 2-D complex sinusoid data set is used to test the capability to capture improved-feature detail out of the spectral estimation techniques. A wide-band 2-D AR process data set is used to evaluate the characteristic of the frequency variance and the PSD variance of the two new fast 2-D solutions. Finally, a third data set tests their performance with a 2-D ISAR radar data set to create a radar image of an actual truck.

7.1. Application One: Narrow-Band 2-D Sinusoid Data

In this application, the simulation results of 2-D complex sinusoids will be presented. The simulation examples serve to demonstrate the high resolution capability of the two new fast solutions for the 2-D LS-MVSE. The 2-D 32×32 complex-point signal has been generated as the sum of five 2-D complex sinusoids (cisoids) corrupted by 2-D additive complex Gaussian white noise samples $w[m, n]$ with variance $\rho_w = 0.1$. The spatial sampling intervals along the axis x and y are $D_x = 1$ cm and $D_y = 1$ cm. The fixed row order $p_1 = 7$ and the variable column order $p_2 = 7$ are chosen. In order to compare the resolutions of the selected spectral estimators, two pairs of very closely spaced sinusoids in white Gaussian noise are selected. The 2-D sampled signal is described by

$$\begin{aligned}
x[m, n] = & \exp[j2\pi(f_{x1} \cdot D_x \cdot m + f_{y1} \cdot D_y \cdot n)] + \exp[j2\pi(f_{x2} \cdot D_x \cdot m + f_{y2} \cdot D_y \cdot n)] \\
& + \exp[j2\pi(f_{x3} \cdot D_x \cdot m + f_{y3} \cdot D_y \cdot n)] + \exp[j2\pi(f_{x4} \cdot D_x \cdot m + f_{y4} \cdot D_y \cdot n)] \\
& + \exp[j2\pi(f_{x5} \cdot D_x \cdot m + f_{y5} \cdot D_y \cdot n)] + w[m, n]
\end{aligned}$$

where the cisoids all have unit amplitude and are located at 2-D spatial fraction of sampling frequencies $f_{x1} = 0.3$, $f_{y1} = 0.3$, $f_{x2} = 0.35$, $f_{y2} = 0.35$, $f_{x3} = -0.2$, $f_{y3} = -0.2$, $f_{x4} = -0.25$, $f_{y4} = -0.15$, $f_{x5} = -0.05$, $f_{y5} = -0.4$. $w[m, n]$ is a 2-D white Gaussian noise. The $SNR = 20$ dB. The numbers of PSD frequencies in 2-D is $N_{f1} = N_{f2} = 4k$. The two new fast solutions of 2-D LS-based MVSE inherit the high-resolution performance of the original non-fast-algorithm methods of the 2-D LS-based MVSE. Therefore, we only show estimates calculated by the two new fast solutions. Fig. 7.1 (a) shows the anticipated 2-D true spectra. The simulation results in Fig. 7.1 (b) to (f) illustrate the enhanced resolution improvement of the two new fast solutions of the 2-D LS-based MVSE, compared to the 2-D classical periodogram, the 2-D covariance AR estimator and the 2-D lattice MV spectral estimator. In Fig. 7.1 (b), the 2-D Nuttall window was applied to suppress the sidelobes of 2-D FFT, but still the 2-D classic periodogram could not distinguish the two very closely -spaced sinusoid pairs. The peaks are fairly wide, and artifact peaks appear due to the sidelobe behavior of the 2-D FFT. Fig. 7.1(c) shows the 2-D covariance AR estimates which combine the first and the fourth quadrant estimates. When the SNR is reduced, the 2-D covariance AR spectral resolution degenerates. The 2-D lattice MV estimates shown in Fig. 7.1(d) could locate some frequencies correctly, however its amplitude estimates are much worse. The five peaks in Fig. 7.1(e) and (f) are very sharp and are accurately located on the true 2-D frequencies. The improved feature details can be easily seen in the 1-D slices of the different 2-D spectra at 2-D spatial frequency 0.3 in the column

dimension shown in Fig. 7.2. The two fast solutions of the 2-D LS-MVSE in covariance case and in modified covariance case are not only more computationally efficient than their direct methods, but they also inherit the advantage of sharper peaks from 2-D MVSE.

7.2. Application Two: Wide-Band 2-D bandpass signal

The wide-band 2-D bandpass signal, another common test case for 2-D application, is used to evaluate the data modeling capability of the two new fast solutions of the 2-D LS-based MVSE. The generated 50×50 random signal has a doughnut-shape bandpass 2-D spectrum shown in Fig. 7.3(a). Fig 7.3(b) to (f) show the experimental results created by different 2-D spectral estimators. The orders $p_1 = p_2 = 10$ and the numbers of PSD in 2-direction $N_{f1} = N_{f2} = 2k$ are chosen in this experiment. Both 2-D periodogram Fig 7.3(b) and 2-D covariance AR Fig 7.3(c) algorithms can not fit the data well. It is hard to recognize the flat top in Fig 7.3(b), while it is hard to tell the double circle in Fig 7.3(c). The 2-D lattice MV estimates shows better results. However, when compared with the results shown in Fig 7.3(e) and (f), the two new fast algorithms of the 2-D MV estimator provide the best fit to the doughnut-shape bandpass 2-D spectrum.

7.3. Application Three: Actual 2-D Synthetic Aperture Radar Data

The truck ISAR radar data introduced in Chapter 4.4 is used to validate the two new fast solutions of the 2-D LS-based MVSE. This application focuses on evaluation of the capability of the two new fast computational solutions of 2-D LS-based MVSE for extracting scattering centers of the truck ISAR imagery made by 2-D spectral analysis of the 2-D radar data. Their improved results presented

in this thesis are compared with those of the 2-D classical periodogram estimator and the 2-D covariance AR estimator.

In path 1 on Fig. 4.14 in Chapter 4, a 2-D radar image in the 2-D spatial domain is obtained by forming the magnitude of the 2-D IFFT (a sample 2-D periodogram). The x-axis represents the cross-range distance in units of cm, while the y-axis represents down-range distance in units of cm. The truck ISAR images in Fig. 7.5 to Fig. 7.11 are generated by four different estimation methods at four selected center azimuth angles $[0^\circ, 47^\circ, 75^\circ \text{ and } 180^\circ]$ to obtain more knowledge about the truck radar image at different viewing aspect angles. A front view of the truck is the 0° azimuth reference. Other parameters are chosen to be the same as those used in the 1-D evaluation in Chapter 4.4. As shown in figures Fig. 7.5 to Fig. 7.11, the two new fast solutions of the 2-D LS-based MVSE can more sharply detect scattering centers in the ISAR imagery than seen in the 2-D classical periodogram estimator and the 2-D covariance AR estimator. These estimated scattering centers are much sharper compared with those estimated by the other methods.

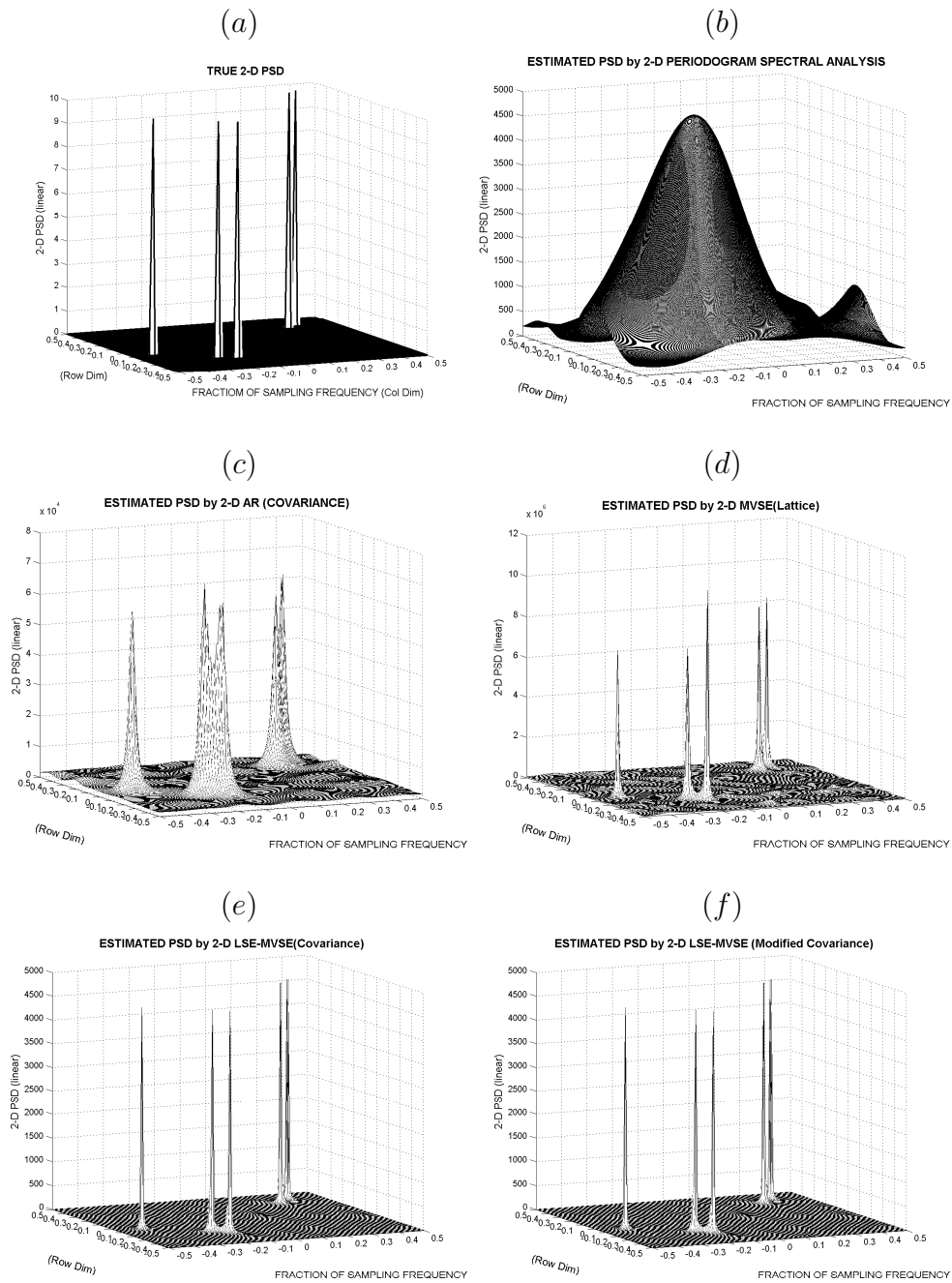


FIGURE 7.1. Comparison of the resolution and accuracy for the different 2-D spectral estimators. (a) True spectra of 2-D complex sinusoids. (b) 2-D classical periodogram estimator. (c) 2-D covariance AR estimator. (d) 2-D lattice MV estimator. (e) the new fast 2-D covariance LS-based MV estimator. (f) the new fast 2-D modified covariance LS-based MV estimator.

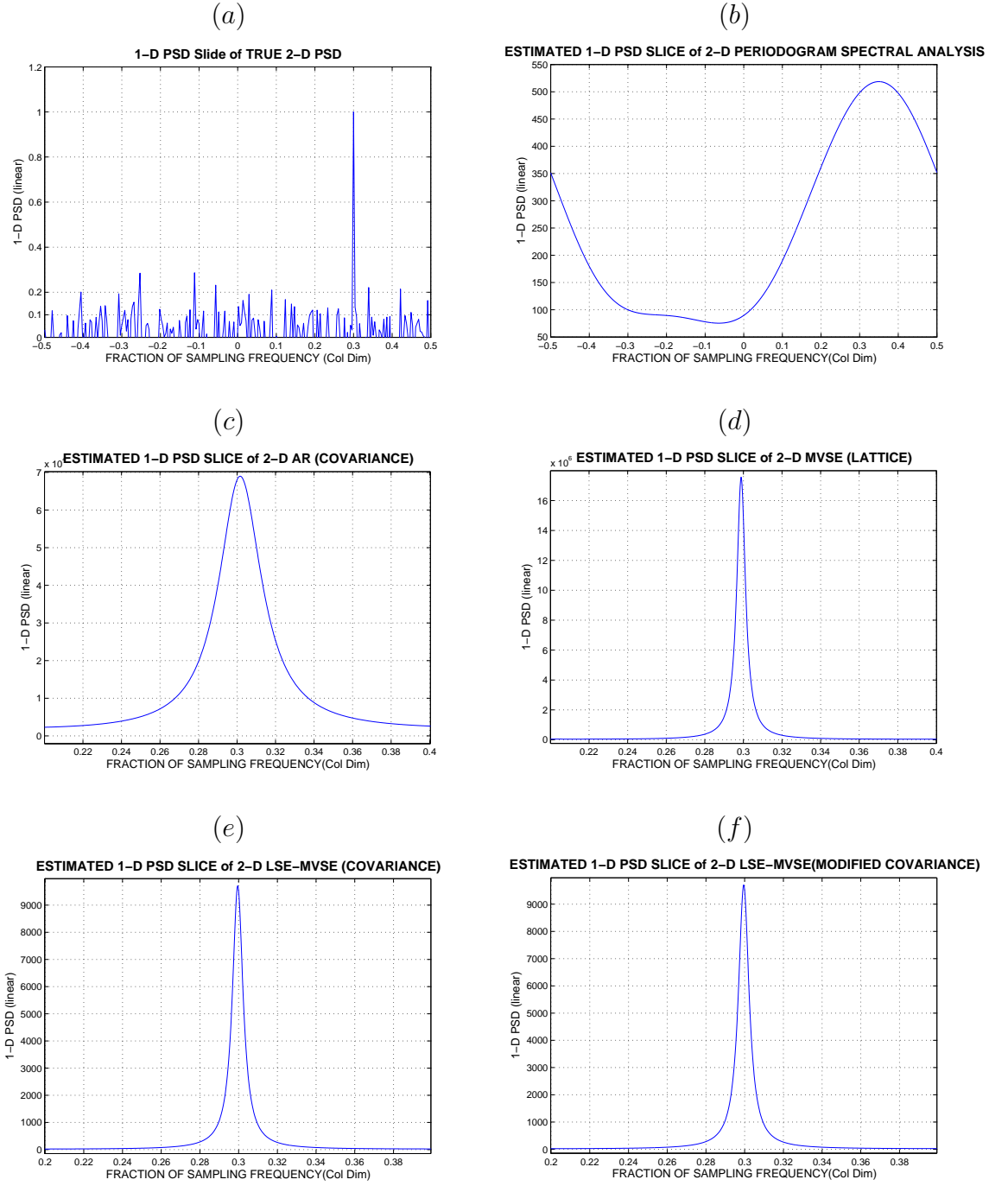


FIGURE 7.2. One-dimensional slices for the different 2-D spectral estimators at 0.3 spatial fraction of sampling frequency in the column dimension. (a) True spectra of 2-D complex sinusoids. (b) 2-D classical periodogram estimator. (c) 2-D covariance AR estimator. (d) 2-D lattice MV estimator. (e) the new fast 2-D covariance LS-based MV estimator. (f) the new fast 2-D modified covariance LS-based MV estimator.

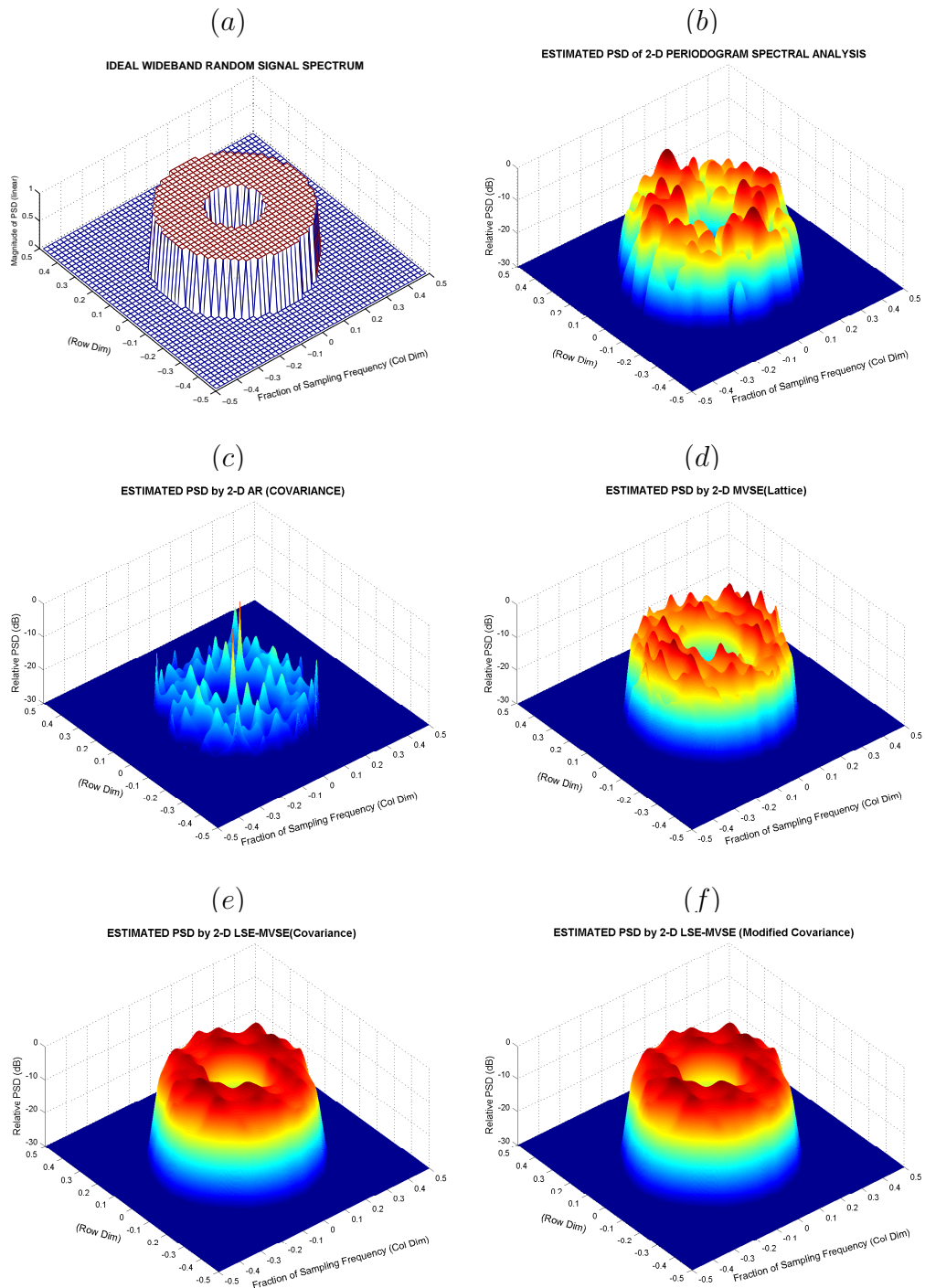


FIGURE 7.3. Comparison data modeling capability for different 2-D spectral estimators. (a) doughnut-shape true 2-D spectrum of wide-band bandpass signal. (b) 2-D classical periodogram estimator. (c) 2-D covariance AR estimator. (d) 2-D lattice MV estimator. (e) the new fast 2-D covariance LS-based MV estimator. (f) the new fast 2-D modified covariance LS-based MV estimator.

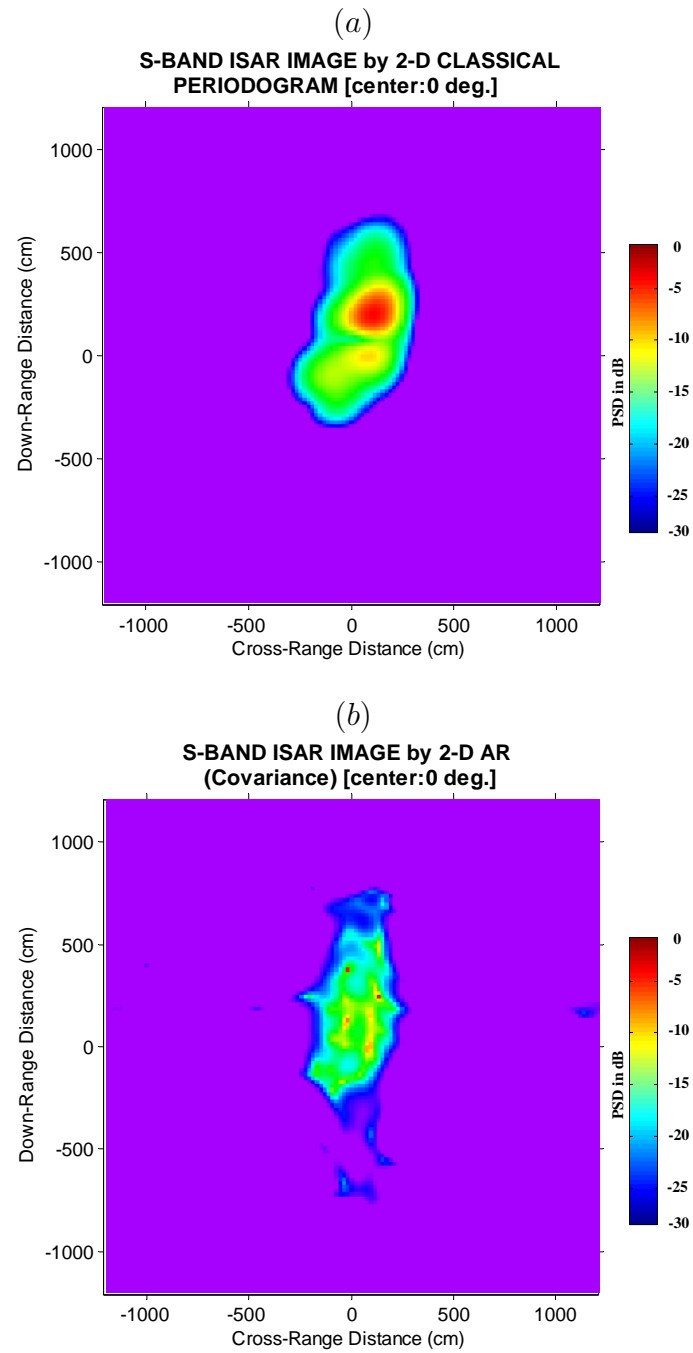


FIGURE 7.4. S-band ISAR image of truck obtained by different spectral estimators (center azimuth 0 degrees - front of truck). (a) 2-D classical periodogram estimator. (b) 2-D covariance AR estimator.

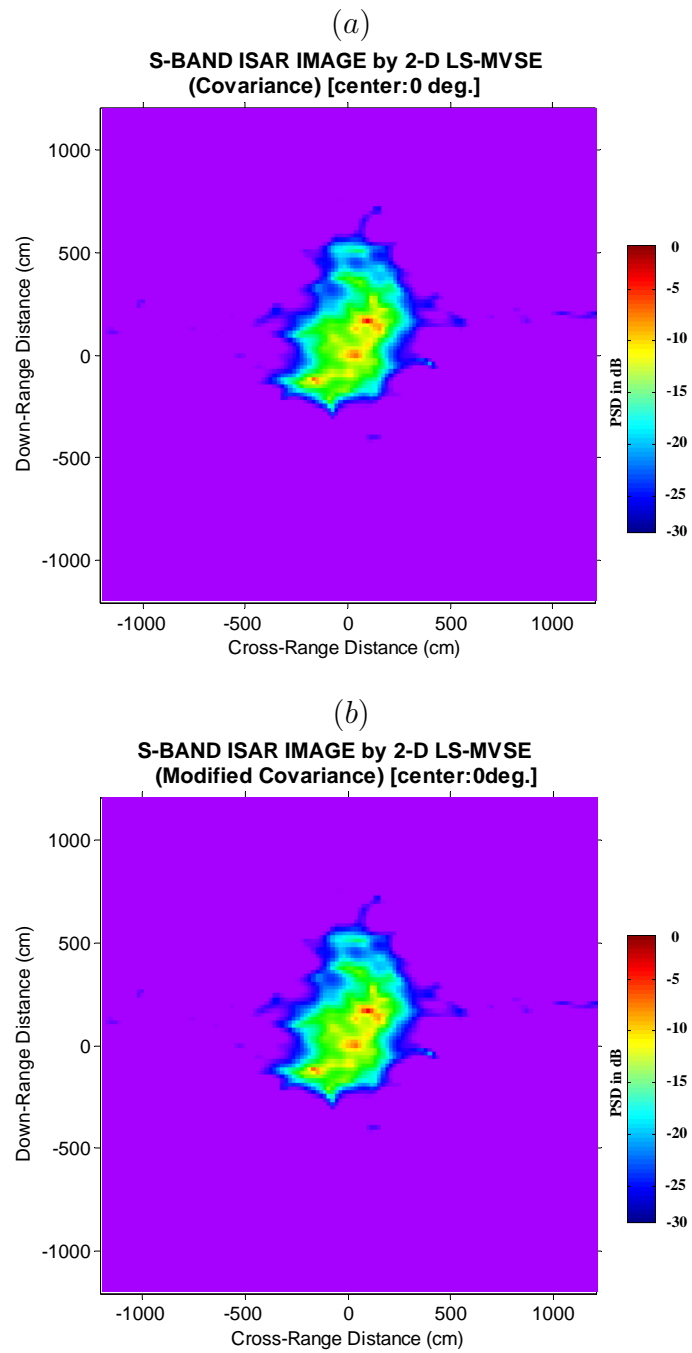


FIGURE 7.5. S-band ISAR image of truck obtained by different spectral estimators (center azimuth 0 degrees - front of truck). (a) the new fast 2-D covariance LS-based MV estimator. (b) the new fast 2-D modified covariance LS-based MV estimator.

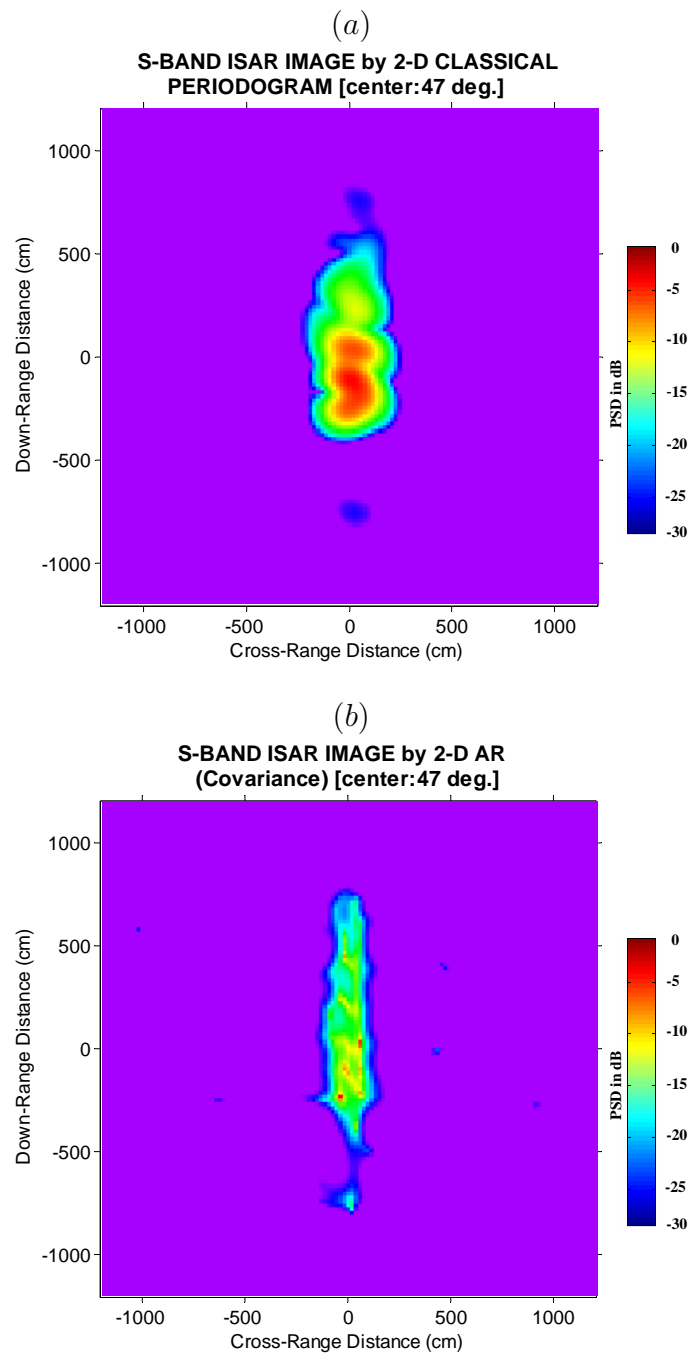


FIGURE 7.6. S-band ISAR image of truck obtained by different spectral estimators (center azimuth 47 degrees). (a) 2-D classical periodogram estimator. (b) 2-D covariance AR estimator.

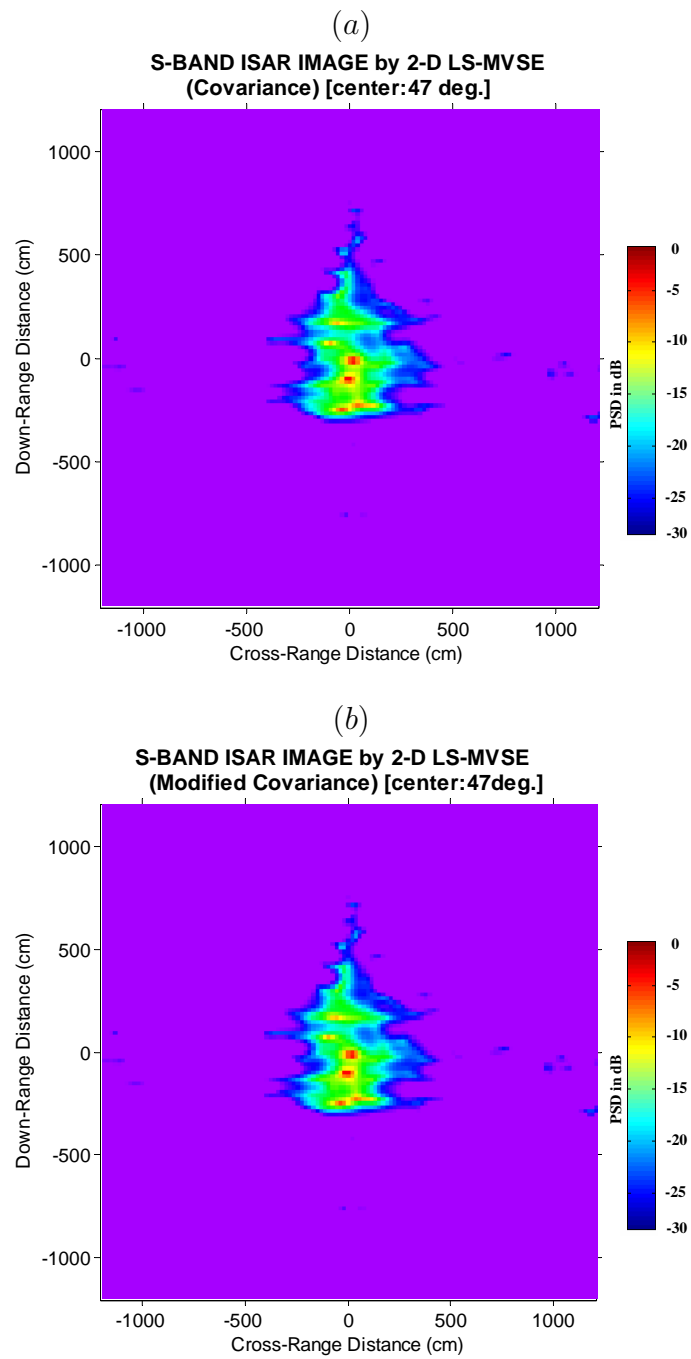


FIGURE 7.7. S-band ISAR image of truck obtained by different spectral estimators (center azimuth 47 degrees). (a) the new fast 2-D covariance LS-based MV estimator. (b) the new fast 2-D modified covariance LS-based MV estimator.

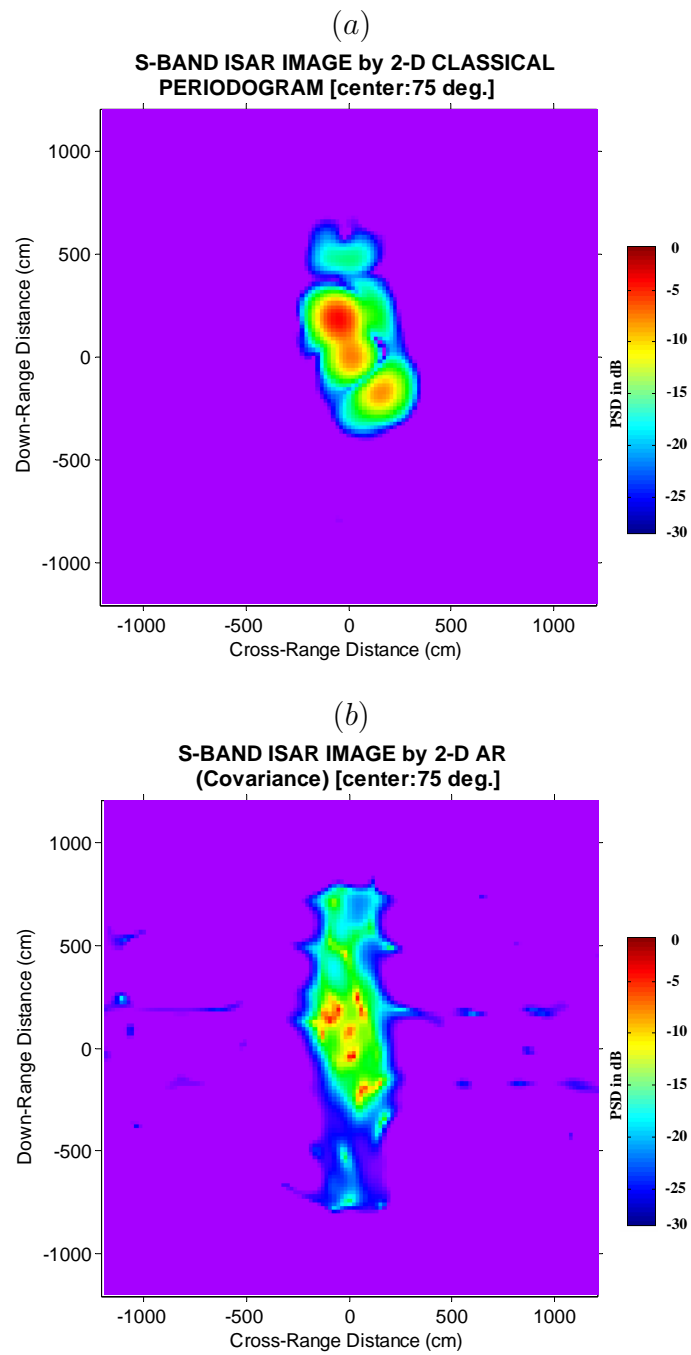


FIGURE 7.8. S-band ISAR image of truck obtained by different spectral estimators (center azimuth 75 degrees). (a) 2-D classical periodogram estimator. (b) 2-D covariance AR estimator.

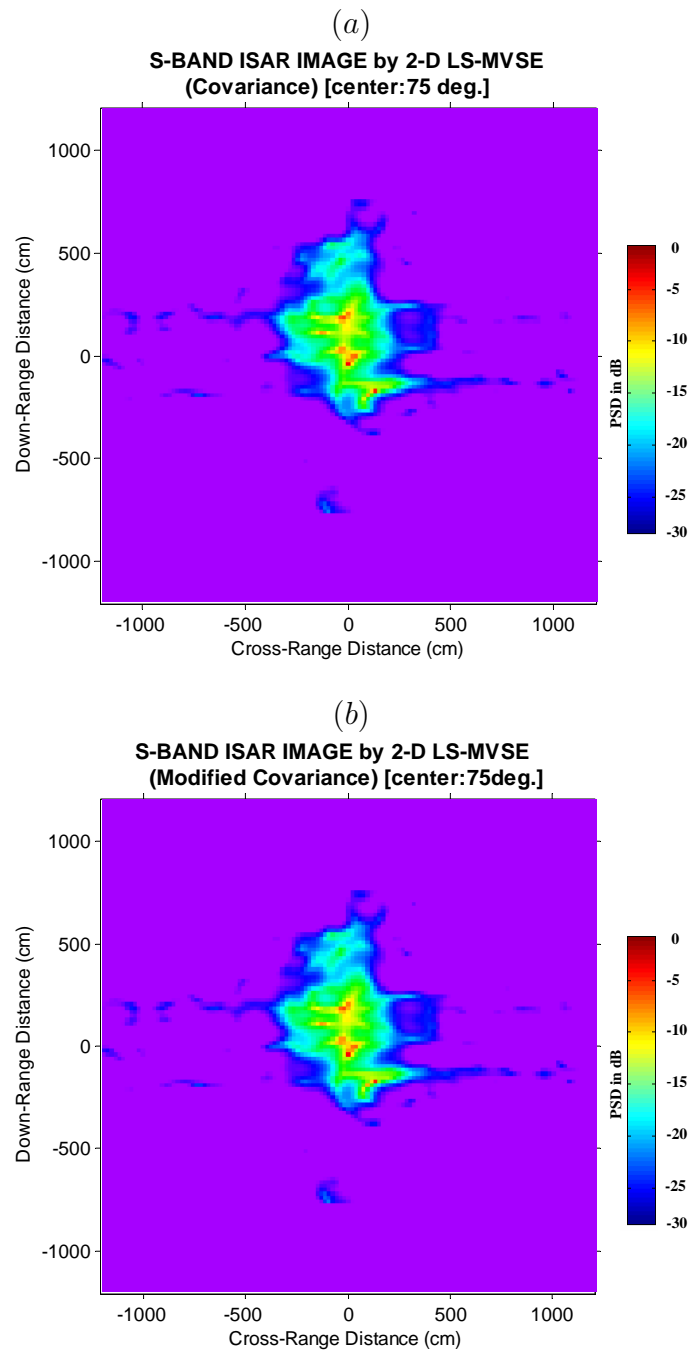


FIGURE 7.9. S-band ISAR image of truck obtained by different spectral estimators (center azimuth 75 degrees). (a) the new fast 2-D covariance LS-based MV estimator. (b) the new fast 2-D modified covariance LS-based MV estimator.

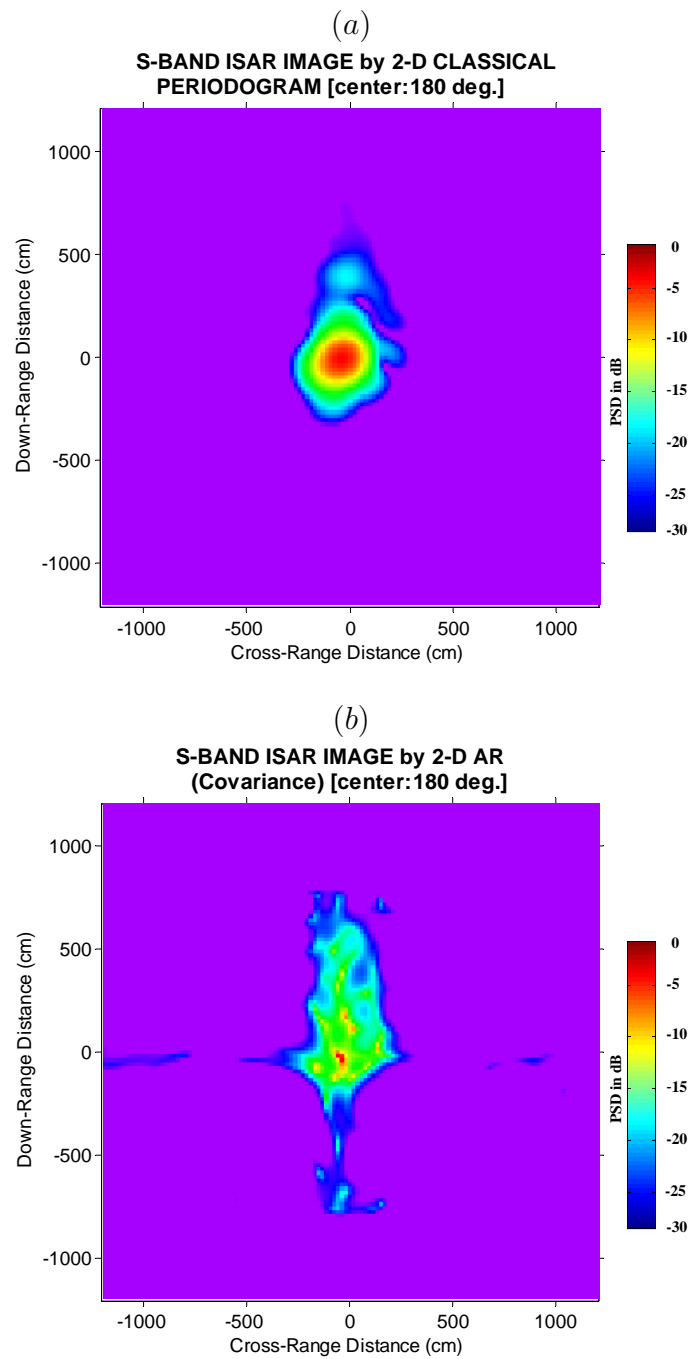


FIGURE 7.10. S-band ISAR image of truck obtained by different spectral estimators (center azimuth 180 degrees - rear of truck). (a) 2-D classical periodogram estimator. (b) 2-D covariance AR estimator.

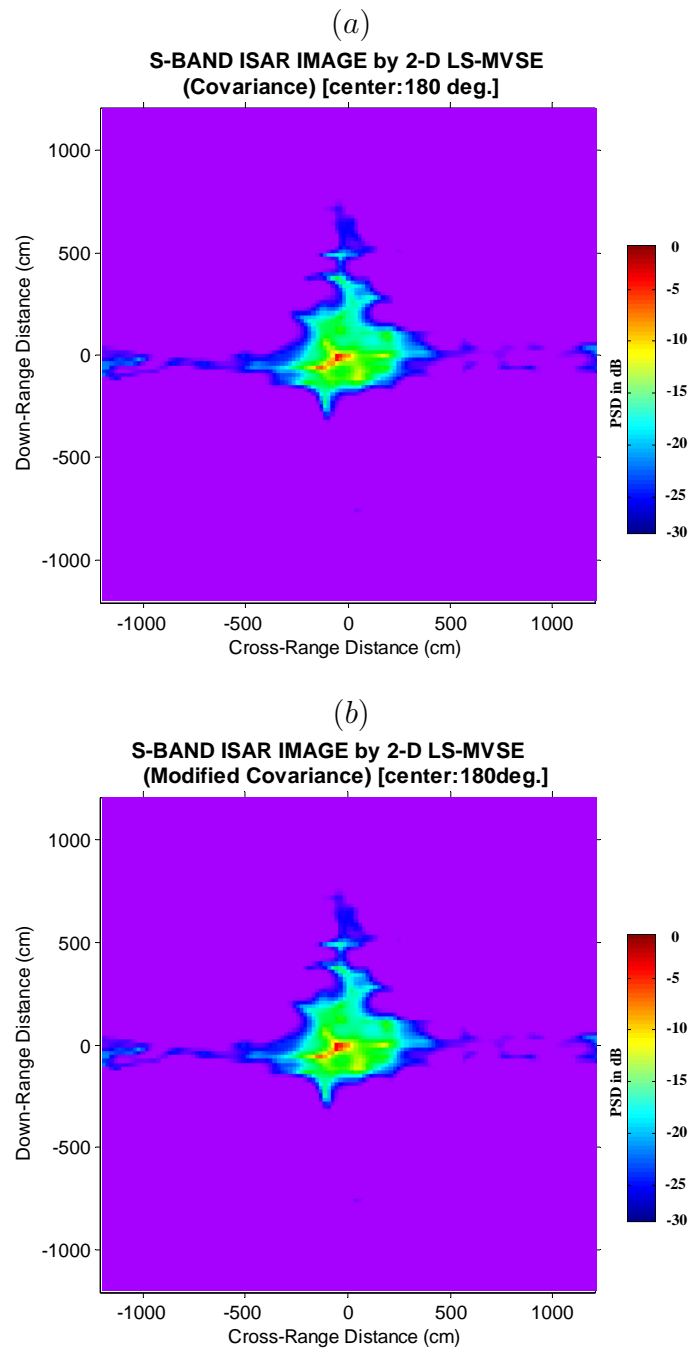


FIGURE 7.11. S-band ISAR image of truck obtained by different spectral estimators (center azimuth 180 degrees - rear of truck). (a) the new fast 2-D covariance LS-based MV estimator. (b) the new fast 2-D modified covariance LS-based MV estimator.

8. SUMMARY OF RESEARCH CONTRIBUTIONS

In this last chapter, the research contributions presented in this thesis are summarized and future research work is proposed. The contributions of this thesis fall into four sections: (1) fast computational solution for the 1-D covariance LS-based MVSE, (2) fast computational solution for the 1-D modified covariance LS-based MVSE, (3) fast computational solution for the 2-D covariance LS-based MVSE, and (4) fast computational solution for the 2-D modified covariance LS-based MVSE. The two 2-D fast computational solutions are rather complex extensions of the two 1-D solutions. However, the two 2-D fast computational solutions produce numerically identical results to the corresponding 1-D fast solutions when the estimation order in one of two dimension is set to zero.

Table 8.1 expands Table 1.1 and compares the properties of the new fast computational solution algorithms with other estimation techniques. The research contributions of this thesis are noted. The four new fast computational solutions have the following advantages in common:

(1) They significantly decrease computational complexity and memory storage requirements, as summarized in Tables 3.2, 3.3, 6.2 and 6.3. The closed-form expressions of the inverses of the 1-D *near-to-Toeplitz* matrices and 2-D *doubly-near-to-Toeplitz* matrices provide special structures that enable fast computational solutions to be developed. The computational complexity of the two 1-D fast computational solutions in the covariance and modified covariance cases are proportional to p^2 with memory storage proportional to p , versus p^3 computation and p^2 storage requirements for both direct solution methods. The computational complexity of the two 2-D fast computational solutions in the covariance and modified covariance cases are proportional to p^5 with memory storage proportional to

p^3 , versus p^6 computation and p^4 storage requirements if solved by using either 2-D direct solution approaches. The four new fast computational solutions significantly reduce computational complexity and memory storage, especially for short data records. Short means that the data size N should not be too large compared with the order p , as illustrated with examples in Fig. 1.6 through Fig. 1.9.

(2) All inherit the capability of improved-feature detail from their direct solution methods. The new fast solutions of the LS-based MV spectral estimators can find extra spectral details which may be missed by Fourier-based and AR spectral estimation algorithms. The resolution for sinusoid signals was shown in this thesis to be about 1.67 times better by our new fast algorithms than by the classical periodogram. However, compared with the lattice-Burg method, the four new fast solutions of MV spectral estimation do not show bias and line-splitting problems. The fast modified covariance MVSE generates the sharpest peaks in some applications. The four new fast solutions exhibited the least PSD variance and the least frequency variance among all spectral estimators tested.

(3) The basis for the fast solutions is the exploitation of the structures of the various inverse relationships, which expresses the inverse of covariance matrices (or covariance-like quadratic-data-matrix product matrices in the case of the least-squares algorithms) in terms of the LP parameters.

(4) Furthermore, all fast computational solutions recursively calculate and save all intermediate order LP parameters so that one can select a lower-order estimator without recalculating the LP parameters. It also helps to find the optimal order for data modeling. The LS-based fast solutions are often not required to use as high an order as non-least-squares solutions in order to achieve similar feature detail resolution in the MVSE spectra.

(5) The LS-based fast solutions are appropriate for applications in which the 1-D or 2-D autocorrelations are unknown and only 1-D or 2-D finite data samples are available. The four new fast solutions can detect more scattering centers in the ISAR imagery of an actual truck than other estimators in both 1-D and 2-D cases. Meanwhile the scattering centers in the ISAR imagery created by the four new fast solutions are sharper than those generated by other methods.

In addition to these important characteristics, there are more distinctive advantages:

(1) In practice, both 1-D and 2-D fast solutions of LS-based MVSE in the modified covariance case appear to achieve higher resolution than the corresponding covariance solutions, since the modified covariance LP approach employs a combination of both forward and backward LP, versus the separate forward and backward LP estimates made in the covariance approach. The modified covariance approach collects more information while calculating the LP parameters.

(2) Both 2-D fast computational solutions of LS-based MVSE are quarter-plane independent and does not have the skew problem of the other 2-D estimators, such as 2-D AR estimator. This further reduces computation load.

Future research includes the following possibilities: (1) Apply the improved results of the new 2-D fast computational solutions of the spectral estimation proposed in this thesis to the new 2-D bandwidth extrapolation techniques proposed by Liew [32] in order to achieve enhanced image of 2-D sensor data. (2) Develop fast computational solutions for 3-D LS-based MVSE which may benefit from the 3-D LP fast algorithm [32]. (3) Develop fast computational solutions for multi-channel MVSE. (4) In the case of long data records, especially for the 2-D case, the advantage of the computational efficiency of the new fast computational solutions presented in this thesis may be canceled out. Alternative multi-dimensional

fast computational solutions of the LS-based MVSE for long data records would also be an interesting topic.

Notations on Table 8.1:

- (a) $N \rightarrow \infty$; unreliable.
- (b) large variance; only short data record.
- (c) guarantee stability; line splitting; biased.
- (d) separate the forward and backward LP; no line splitting; unbiased; less variance.
- (e) combine the forward and backward LP; no line splitting; unbiased; less variance.
- (f) less variance; no line splitting; unbiased.
- (g) large variance; short data record.
- (h) guarantee stability; Less variance; line splitting; biased estimator.
- (i) separate the forward and backward LP; less variance; no line splitting; unbiased.
- (j) combine the forward and backward LP; less variance; no line splitting; unbiased.

Spectral Estimator Type	Defining Equations	Method	Resolution Capability	Lower-order Solutions Recursively Generated	Fast Solution Available	Relative Computational Complexity	Relative Storage	Notation
Classical Fourier Methods	Eq. 4.2	Periodogram	Low	×	×	$O(N \log_2 N)$	$O(N)$	(a)
		Yule-Walker	Medium	✓	✓	$O(p^2 + N_f \log_2 N_f)$	$O(p)$	(b)
		Burg Lattice	Medium	✓	✓			(c)
		Covariance	High	✓	✓			(d)
Autoregressive	Eq. 4.3	Modified Covariance	High	✓	✓			(e)
		Original Approach	Medium	×	✓	$O(p^3)$	$O(p^3)$	(f)
		Yule-Walker + Correlation + FFT	Medium	✓	✓	$O(p^2 + N_f \log_2 N_f)$	$O(p)$	(g)
		Burg-Lattice + Correlation + FFT	High	✓	✓			(h)
Minimum Variance Spectral Estimation	Eq. 3.3	Covariance + Correlation + FFT	High	✓	✓			(i)
		Modified Covariance + Correlation + FFT	High	✓	✓			(j)
		Eq. 3.31	High	✓	✓			(i)

TABLE 8.1. Comparison of Spectral Estimation Techniques. × indicates not available, ✓ indicates available, N is the number of data samples, p is the order of model, N_f is the number of FFT frequency bins. Notations are given in this chapter.

BIBLIOGRAPHY

- [1] J. Capon, "High Resolution Frequency-Wavenumber Spectral Analysis", *Proc. IEEE*, vol. 57, pp. 1408-1418, August, 1969.
- [2] R. T. Lacoss, "Data Adaptive Spectral Analysis Methods", *Geophysics*, vol. 36, pp. 661-675, August, 1971.
- [3] D. Steinberg, "Computational Matrix Algebra", *McGraw-Hill Book Company, Inc.*, N.Y., 1974.
- [4] J. P. Burg, "Maximum Entropy Spectral Analysis", *Ph.D. dissertation, Department of Geophysics, Stanford University*, Palo Alto, C.A., 1975.
- [5] A. H. Nuttall, "Spectral Analysis of a Univariate Proces with Bad Data Points, via Maximum Entropy and Linear Predictive Techniques", *Naval Underwater Systems Center Technical Report TR-5303*, New London, C.T., March, 1976.
- [6] B. Friedlander, M. Morf, T. Kailath and L. Ljung, "New Inversion Formulas for Matrices Classified in Terms of Their Distance From Toeplitz Matrices", *Linear Algebra and Its Applications*, vol. 27, pp. 31-60, 1979.
- [7] J. Cadzow and K. Ogino, "Two-dimensional Spectral Esstimation", *IEEE trans. on Acoustics, Speech, and Signal Processing*, vol. 29, No. 3, pp. 396-401, June, 1981.
- [8] J. McClellan, "Multidimensional Spectral Estimation", *Proc. IEEE*, vol. 70, pp. 1029-1037, September, 1982.
- [9] D. Dudgeon and R. Mersereau, "Multidimensional Digital Signal Processing", *Prentice-Hall, Inc.*, Englewood Cliffs, N.J., 1984.
- [10] C. L. Nikias, P. D. Scott and J. H. Siegel, "Computer Based Two-Dimensional Spectral Estimation for the Detection of Prearrhythmic States after Hypothermic Myocardial Preservatrion", *Comput. Biol. Med.*, vol. 14, pp. 159-178, 1984.
- [11] F. U. Dowla, "Relationship between Maximum Likelihood Method and Autoregressive Modeling in Multidimensional Power Spectral Estimation", *IEEE trans. on Acoustics, Speech, and Signal Processing*, vol. ASSP-32, No. 5, October, 1984.
- [12] S. Shon and K. Mehrotra, "Performance Comparison of Autoregressive Estimation Methods", *IEEE Proceedings of the Internatioanl Conference on Acoustics, Speech, and Signal Processing*, pp. 14.3.1-14.3.4, 1984.

- [13] B. Musicus, "Fast MLM Power Spectrum Estimation from Uniformly Spaced Correlations", *IEEE Transactions on Acoustics, Speech, and Signal Processing*, vol. ASSP-33, pp. 1333-1335, October, 1985.
- [14] S. L. Marple, Jr., "An Introduction to and a Fast Algorithm for Multichannel Variance Spectral Estimation", *Third ASSP Workshop on Spectrum Estimation and Modeling*, Boston, M.A., November, 1986.
- [15] S. L. Marple, Jr., "Digital Spectral Analysis with Applications", *Prentice-Hall, Inc.*, Englewood Cliffs, N.J., 1987.
- [16] Kay, S. M., "Modern Spectral Estimation: theory and application", *Prentice-Hall, Inc.*, Englewood Cliffs, N.J., 1988.
- [17] J. Krolik and M. Eizenman, "Minimum Variance Spectral Estimation for Broadband Source Location Using Steered Covariance Matrices", *International Conference on Acoustics, Speech, and Signal Processing*, vol. 5, pp. 2841-844, New York, N.Y., April, 1988.
- [18] S. L. Marple, Jr., "A Fast Computational Algorithm for The Modified Covariance Method of Linear Prediction", *Digital Signal Processing Journal*, vol. 1, pp. 124-133, July, 1991.
- [19] A. E. Frazho and P. J. Sherman, "On the Convergence of the Minimum Variance Spectral Estimator in Nonstationary noise", *IEEE Transactions on Information Theory*, vol.37, No. 5, pp. 1457-1459, September, 1991.
- [20] S. L. Marple, Jr., "A Fast Algorithm for the Two-Dimensional Covariance Method of Linear Prediction", *IEEE International Conference on Acoustics, Speech, and Signal Processing*, pp. 1693-1696, Detroit, M.I., May, 1995.
- [21] P. Owens and M. English, "Multichannel Spectral Estimation of ECGs", *Computers in Cardiology*, pp. 437-440, September, 1996.
- [22] H. Shi, "Cloud Movement Detection for Satellite Image", *International Conference on Signal Proceedings*, vol. 2, pp. 982-985, Beijing, China, October, 1998.
- [23] M. Soumekh, "Synthetic Aperture Radar Signal Processing", *Wiley*, N.Y., 1999.
- [24] S. L. Marple, Jr., "Two-Dimensional Lattice Linear Prediction Parameter Estimation Method and Fast Algorithm", *IEEE Signal Processing Letters*, vol. 7, No. 6, June, 2000.

- [25] J. Andreas, S. L. Marple and P. Stoica, "Computationally Efficient Two-Dimensional Capon Spectrum Analysis", *IEEE Transactions on Signal Processing*, vol. 48, No. 9, pp. 2651-2661, September, 2000.
- [26] J. A. C. Lee and D. C. Munson Jr., "Spatially variant apodization for image reconstruction from partial Fourier data ", *IEEE Transactions on Image Processing*, vol. 9, No. 11, pp 1914-1925, November, 2000.
- [27] S. L. Marple, Jr., "Minimum Variance Spectral Estimator Fast Algorithm Based on Covariance and Modified Covariance Methods of Linear Prediction", *Signals, Systems and Computers, Conference Record of the Thirty-Fifth Asilomar Conference*, vol. 1, pp. 711-714, Pacific Grove, C.A., November, 2001.
- [28] A. Mathur, N. H. Younan and L. M. Bruce, "Automated Texture Recognition System Based On 2-D Minimum Variance Spectral Estimation", *IEEE International Geoscience and Remote Sensing Symposium, 2004. IGARSS '04. Proceedings*, vol. 2, pp. 1061-1064, 2004.
- [29] T. S. Rappaport, "Wireless Communications Principles and Practice, Second Edition", *Prentice-Hall, Inc.*, Englewood Cliffs, N.J., 2004.
- [30] L. Wei and S. L. Marple, Jr., "A New Least-squares-based Minimum Variance Spectral Estimator Fast Algorithm", *2005 IEEE International Conference on Acoustics, Speech, and Signal Processing*, vol. 4, pp. 405-408, Philadelphia, P.A., March, 2005.
- [31] Y. Wang, J. Li and P. Stoica, "Two-dimensional Nonparametric Spectral Analysis in the Missing Data Case", *2005 IEEE International Conference on Acoustics, Speech, and Signal Processing*, vol. 4, pp. 397-400, Philadelphia, P.A., March, 2005.
- [32] J. Liew, "Multi-dimensional Parametric Estimation: Two-dimensional Sharpening by Predictive Bandwidth Extrapolation and Fast Algorithms For Three-dimensional Autoregressive Estimation", *Ph.D. dissertation, Department of Electrical and Computer Engineering, Oregon State University*, Corvallis, O.R., June, 2006.
- [33] L. Wei and S. L. Marple, Jr., "Fast Algorithm for Least-Squares-Based Minimum Variance Spectral Estimation", *submitted to EURASIP Journal on Signal Processing*, 2006.
- [34] L. Wei and S. L. Marple, Jr., "Fast Algorithm for Covariance Least-Squares-Based 2-D Minimum Variance Spectral Estimation", *submitted to IEEE Transactions on Signal Processing*, 2006.
- [35] <http://www.srtm.usgs.gov>.

- [36] “Migration of Birds, Flight Speed and Rate of Migration”,
<http://www.npwrc.usgs.gov/resource/birds/migratio/speed.htm>.
- [37] Wikipedia, “Wind Speed”, *<http://www.en.wikipedia.org/wiki/Wind-speed>*.
- [38] *<http://www.fhwa.dot.gov>*.

APPENDICES

APPENDIX A. LIST OF ACRONYMS

<u>Notation</u>	<u>Description</u>	<u>Page</u>
1-D	One-dimensional	1
2-D	Two-dimensional	1
ACS	Autocorrelation sequence	4
ACS-based	Autocorrelation sequence-based	4
AR	Autoregressive	1
DTFT	Discrete time Fourier transform	28
FIR	Finite impulse response	20
FFT	Fast Fourier transform	2
IFFT	Inverse Fast Fourier transform	53
ISAR	Inverse synthetic aperture radar	15
LP	Linear prediction	1
LS-based	Least-squares-based	1
MV	Minimum variance	12
MVSE	Minimum variance spectral estimation	1
PSD	Power spectral density	2
RF	Radio Frequency	51
SNR	Signal-to-noise ratio	14

APPENDIX B. LIST OF SYMBOLS

<u>Symbols</u>	<u>Description</u>	<u>Page</u>
$y[n]$	Output of FIR filter	20
$h_p[n]$	FIR impulse response	20
\mathbf{h}_p	FIR impulse response vector	20
$x[n]$	An input sample	20
\mathbf{J}	Reflection matrix	20
$\mathbf{x}_p[n]$	Input data vector	20
p	Order of FIR filter	20
T	Matrix transpose	20
H	Matrix hermitian transpose	20
\mathbf{R}_p	Toeplitz autocorrelation matrix	20
$r[m]$	Autocorrelation sequence element	20
T	Sampling interval	20
$\mathbf{e}_p(f)$	Complex sinusoid vector	20
f	Frequency	21
ρ_{MV-ar}	ACS-based minimum filter output variance	21

<u>Symbols</u>	<u>Description</u>	<u>Page</u>
P_{MV-ar}	ACS-based MVSE	21
\mathbf{R}_p^{-1}	Inverse matrix of Toeplitz autocorrelation matrix	21
$y^b[n]$	Forward filter output of FIR filter	21
$y^f[n]$	Backward filter output of FIR filter	21
$\bar{\mathbf{a}}_p$	Filter forward parameter vector in 1-D covariance case	21
$\bar{\mathbf{b}}_p$	Filter backward parameter vector in 1-D covariance case	21
$\hat{\rho}_p$	LS-based filter output variance in 1-D covariance case	22
\mathbf{X}_p	Toeplitz data matrix	22
$\hat{\mathbf{R}}_p$	Near-to-Toeplitz data product matrix in 1-D covariance case	22
$\hat{\mathbf{R}}_p^{-1}$	Inverse of the data product matrix in 1-D covariance case	23
$\hat{\rho}_{MV-cov}$	LS-based minimum filter output variance in 1-D covariance case ..	24
\hat{P}_{MV-cov}	LS-based MVSE in 1-D covariance case	24
$\tilde{\mathbf{a}}_p$	Filter forward parameter vector in 1-D modified covariance case ...	24
$\hat{\rho}_p$	LS-based filter output variance in 1-D modified covariance case ...	25
\hat{P}_{MV-mod}	LS-based MVSE in 1-D modified covariance case	25
$\hat{\mathbf{R}}_p$	Near-to-Toeplitz data product matrix in 1-D modified covariance case	25
$\hat{\mathbf{R}}_p^{-1}$	Inverse of the data product matrix in 1-D modified covariance case	25
\mathbf{A}_p	Triangular Toeplitz matrix of forward AR parameters	26

<u>Symbols</u>	<u>Description</u>	<u>Page</u>
\mathbf{B}_p	Triangular Toeplitz matrix of backward AR parameters	27
ψ_{MV}	Weighted correlations of AR parameters	27
$\hat{\mathbf{R}}_{p-1}^{\cdot}$	Upper partition matrix in 1-D covariance case	29
$\hat{\mathbf{R}}_{p-1}^{\cdot\cdot}$	Down partition matrix in 1-D covariance case	29
$\bar{\mathbf{c}}_p$	Auxiliary vector in 1-D covariance case	29
$\bar{\mathbf{d}}_p$	Auxiliary vector in 1-D covariance case	29
$\bar{\rho}_p^a$	Forward LP error variance estimate in 1-D covariance case	30
$\bar{\rho}_p^b$	Backward LP error variance estimate in 1-D covariance case	30
$\bar{\rho}_p^c$	Gain adjustment factor in 1-D covariance case	32
$\bar{\rho}_p^d$	Gain adjustment factor in 1-D covariance case	32
$\bar{\Phi}_p$	Gain adjustment matrix 1-D covariance case	32
$\bar{\mathbf{A}}_p$	Triangular Toeplitz matrix of forward LP parameters in 1-D covariance case	33
$\bar{\mathbf{B}}_p$	Triangular Toeplitz matrix of backward LP parameters in 1-D covariance case	33
$\bar{\mathbf{C}}_{p-1}$	Triangular Toeplitz matrix of auxiliary parameters in 1-D covariance case	33
$\mathbf{0}$	All zero matrix	33
$\bar{\mathbf{P}}_{p-1}$	Diagonal matrix of gain adjustment in 1-D covariance case	33
$\hat{\psi}_{MV}$	Weighted correlations of LP parameters in 1-D covariance case ...	34
$\hat{\mathbf{R}}_{p-1}^{\cdot}$	Upper and down partition matrix in 1-D modified covariance case	36

<u>Symbols</u>	<u>Description</u>	<u>Page</u>
$\tilde{\rho}_p^a$	Forward and backward LP error variance estimate in 1-D modified covariance case	37
$\tilde{\mathbf{c}}_p$	A auxiliary vector in 1-D modified covariance case	38
$\tilde{\Phi}_p$	Gain adjustment matrix in 1-D modified covariance case	38
\mathbf{I}	Identity matrix	38
$\tilde{\mathbf{A}}_p$	Triangular Toeplitz matrix of forward LP parameters in 1-D modified covariance case	40
$\tilde{\mathbf{B}}_p$	Triangular Toeplitz matrix of backward LP parameters in 1-D modified covariance case	40
$\tilde{\mathbf{C}}_{p-1}$	Triangular Toeplitz matrix of auxiliary parameters in 1-D modified covariance case	40
$\tilde{\mathbf{D}}_{p-1}$	Triangular Toeplitz matrix of auxiliary parameters in 1-D modified covariance case	40
$\tilde{\mathbf{P}}_{p-1}$	Gain adjustment matrix in 1-D modified covariance case	41
$\tilde{\psi}_{MV}$	Weighted correlations of LP parameters in 1-D modified covariance case	41
$y[n_1, n_2]$	Output of 2-D FIR filter	64
$h_p[n_1, n_2]$	2-D FIR impulse response	64
\mathbf{h}_{p_2}	2-D FIR impulse response vector	64
$x[n_1, n_2]$	2-D input sample	64
p_1	Row order of 2-D FIR filter	64
p_2	Column order of 2-D FIR filter	64
\mathbf{R}_{p_2}	2-D block Toeplitz autocorrelation matrix	65
$\mathbf{e}_{p_2}(f_1, f_2)$	2-D block complex sinusoid vector	66

<u>Symbols</u>	<u>Description</u>	<u>Page</u>
T_1	2-D sampling interval in row direction	66
T_2	2-D sampling interval in column direction	66
f_1	2-D spatial frequency in row direction	66
f_2	2-D spatial frequency in column direction	66
$\rho_{2DMV-ar}$	2-D ACS-based minimum filter output variance	66
$P_{2DMV-ar}$	2-D ACS-based MVSE	67
$y^f[n_1, n_2]$	Forward filter output of 2-D FIR filter	67
$y^b[n_1, n_2]$	Backward filter output of 2-D FIR filter	67
$\hat{\rho}_{p_2}$	LS-based filter output variance in 2-D covariance case	68
$\underline{\mathbf{X}}_{p_2}$	2-D block Toeplitz data matrix	69
$\hat{\underline{\mathbf{R}}}_{p_2}$	Near-to-doubly-Toeplitz data product matrix in 2-D covariance case	69
$\hat{\underline{\mathbf{R}}}_{p_2}^{-1}$	Inverse of the near-to-doubly-Toeplitz data product matrix in 2-D covariance case	69
$\hat{P}_{2DMV-cov}$	LS-based MVSE in 2-D covariance case	69
$\hat{\underline{\mathbf{R}}}_{p_2}$	Near-to-doubly-Toeplitz data product matrix in 2-D modified covariance case	73
$\hat{\underline{\mathbf{R}}}_{p_2}^{-1}$	Inverse of the near-to- doubly-Toeplitz data product matrix in 2-D modified covariance case	73
$\hat{P}_{2DMV-mod}$	LS-based MVSE in 2-D modified covariance case	73
\mathbf{P}_{p_2}	ACS-based 2-D minimum filter output variance	76
$\underline{\mathbf{A}}_{p_2}$	2-D block triangular Toeplitz matrix of forward AR parameters ...	77

<u>Symbols</u>	<u>Description</u>	<u>Page</u>
$\underline{\mathbf{B}}_{p_2}$	2-D block triangular matrix of backward AR parameters	78
$\underline{\mathbf{P}}_{p_2}^A$	2-D block matrix of forward filter variance	78
$\underline{\mathbf{P}}_{p_2}^B$	2-D block matrix of backward filter variance	78
$\alpha[m, k]$	Weighted correlation-like result in 2-D ACS case	78
$\hat{\underline{\mathbf{R}}}_{p_2-1}'$	2-D block upper partition matrix in 2-D covariance case	82
$\hat{\underline{\mathbf{R}}}_{p_2-1}''$	2-D block down partition matrix in 2-D covariance case	82
$\underline{\mathbf{X}}_{p_2}$	2-D block Toeplitz data matrix	82
$\underline{\mathbf{c}}_{p_2}$	2-D block auxiliary matrix in 2-D covariance case	83
$\underline{\mathbf{d}}_{p_2}$	2-D block auxiliary matrix in 2-D covariance case	83
$\underline{\mathbf{A}}_{p_2}$	2-D block triangular Toeplitz matrix of forward LP parameters in 2-D covariance case	86
$\underline{\mathbf{B}}_{p_2}$	2-D block triangular Toeplitz matrix of backward LP parameters in 2-D covariance case	86
$\underline{\mathbf{C}}_{p_2-1}$	2-D block triangular Toeplitz matrix of auxiliary parameters in 2-D covariance case	87
$\underline{\mathbf{D}}_{p_2-1}$	2-D block triangular Toeplitz matrix of auxiliary parameters in 2-D covariance case	87
$\underline{\mathbf{P}}_{p_2}^A$	2-D block forward LP error variance estimate in 2-D covariance case	87
$\underline{\mathbf{P}}_{p_2}^B$	2-D block backward LP error variance estimate in 2-D covariance case	87
$\underline{\mathbf{P}}_{p_2}^C$	2-D block gain adjustment matrix in 2-D covariance case	87
$\underline{\mathbf{P}}_{p_2}^D$	2-D block gain adjustment matrix in 2-D covariance case	87

<u>Symbols</u>	<u>Description</u>	<u>Page</u>
$\hat{\underline{\Psi}}$	2-D weighted correlations of LP parameters in 2-D covariance case	88
$\hat{\underline{\alpha}}[m, k]$	Weighted correlation-like result in 2-D covariance case	88
$\hat{\underline{\mathbf{R}}}_{p_2-1}$	2-D block upper and down partition matrix in 2-D modified covariance case	92
$\tilde{\underline{\mathbf{c}}}_{p_2}$	2-D block auxiliary matrix in 2-D modified covariance case	93
$\tilde{\underline{\mathbf{d}}}_{p_2}$	2-D block auxiliary matrix in 2-D modified covariance case	93
$\tilde{\underline{\mathbf{A}}}_{p_2}$	2-D block triangular Toeplitz matrix of forward LP parameters in 2-D modified covariance case	96
$\tilde{\underline{\mathbf{B}}}_{p_2}$	2-D block triangular Toeplitz matrix of backward LP parameters in 2-D modified covariance case	96
$\tilde{\underline{\mathbf{C}}}_{p_2-1}$	2-D block triangular Toeplitz matrix of auxiliary parameters in 2-D modified covariance case	97
$\tilde{\underline{\mathbf{D}}}_{p_2-1}$	2-D block triangular Toeplitz matrix of auxiliary parameters in 2-D modified covariance case	97
$\tilde{\underline{\mathbf{P}}}^A_{p_2}$	2-D block forward LP error variance estimate in 2-D modified covariance case	97
$\tilde{\underline{\mathbf{P}}}^B_{p_2}$	2-D block backward LP error variance estimate in 2-D modified covariance case	97
$\tilde{\underline{\mathbf{P}}}^C_{p_2}$	2-D block gain adjustment matrix in 2-D modified covariance case ..	97
$\tilde{\underline{\mathbf{P}}}^D_{p_2}$	2-D block gain adjustment matrix in 2-D modified covariance case ..	97
$\hat{\underline{\Psi}}$	2-D weighted correlations of LP parameters in 2-D modified covariance case	98
$\hat{\underline{\alpha}}[m, k]$	Weighted correlation-like result in 2-D modified covariance case	98